

Università di Pisa

Facoltà di Scienze Matematiche Fisiche e Naturali

Dipartimento di Fisica “E. Fermi”



Tesi di Laurea Magistrale in Fisica della Materia

Spin physics in dipolar quantum gases of erbium atoms

Candidato:

Gabriele Natale
Matr. 527902

Relatore esterno:

Prof.ssa Francesca Ferlaino
(University of Innsbruck)

Relatore interno:

Prof.ssa Donatella Ciampini

Anno Accademico 2016/2017

Alla mia famiglia...

Contents

Introduction	1
1 Erbium properties	4
1.1 Electronic configuration and energy spectrum	5
1.1.1 Energy spectrum	6
1.1.2 Hyperfine structure	7
1.2 Interaction with magnetic fields	8
1.2.1 Magnetic moment	8
1.2.2 Landé g-factor	8
1.2.3 Zeeman splitting	10
1.3 Interactions properties	12
1.3.1 The contact interactions	12
1.3.2 The magnetic dipole-dipole interactions	14
2 Production of spinor Er quantum gases	16
2.1 Experimental setup	16
2.1.1 Reaching quantum degeneracy	19
2.2 Overview on spin preparation	20
2.2.1 Direct radio-frequency excitation of the Zeeman sublevels	20
2.2.2 Landau-Zener sweep	27
3 Experiment on spin-1/2 system	33
3.1 The optical lattice: basic concepts	34
3.2 Fermi-Hubbard model	36
3.3 Measurement of the interaction properties	38
3.3.1 Experimental sequences	39
3.3.2 The onsite interaction	41

4	Advanced Spin-preparation with light	45
4.1	AC-Stark shift	45
4.1.1	Stark shift: theory	45
4.1.2	Ac-Stark shift: calculation at 631 nm	49
4.2	Realization of a laser source at 631 nm	52
4.2.1	Design of the laser system	54
4.2.2	Diode laser characterization	56
4.2.3	Experimental setup	61
4.3	Overview on spin preparation/manipulation with light	64
4.3.1	Optical pumping scheme	64
4.3.2	Raman scheme	65
4.3.3	Stimulated raman adiabatic passage	66
4.3.4	Single spin state manipulation	68
	Conclusion	70
	A Lock of the laser system	79
	Acknowledgements	83

Introduction

One of the fundamental principle of quantum mechanics relies on the revolutionary concept of wave-particle duality [De 25]. In every-day life, ordinary objects at room temperatures have an extension of the corresponding wavepacket so small that their wave nature is not apparent. On the other hand, at extremely low temperatures, atomic gases reveal their wave-like nature. Albert Einstein, following Satyandra Bose's work on photons, predicted that, in these extreme conditions, atoms occupy a single macroscopic quantum wave function. This new state of matter is known as Bose-Einstein condensate (BEC) [Bos24; Ein25].

Einstein predictions remained for decades a mere theoretical concept. The main limiting factor to realize such an exotic state of matter was the requirement of extremely low temperatures. For a million atoms, it would be indeed necessary to reach temperatures on the order of tens of nano Kelvin. Only after the development of new laser cooling and atomic trapping techniques in the 1980's and ultimately the implementation of evaporative cooling, the first Bose-Einstein condensate was achieved with Rb [And95] and Na [Dav95] .

In this temperature regime, where thermal wavelength and inter-particle distance become of the same order, quantum statistics start to play a role.

Whereas bosons undergo Bose-Einstein condensation, fermions begin to occupy one-by-one all the energy levels up to the Fermi energy, forming the so called degenerate Fermi gas (dFg). The first dFg was reached only later in the 1999 [DeM99]. The delay in reaching a dFg is due to the Pauli principle, which makes the collision properties different with respect to bosons and the implementation of evaporative cooling not straightforward.

Over the last two decades, quantum gases have proven to be ideal systems to study novel few- and many-body quantum phenomena, e.g [Kno08] [Cho16]. These atomic gases provide a clean (impurities are essentially absent) and dynamically tunable system. The versatility of ultracold atomic gases relies on the possibility of tuning the strength of the interactions between atoms, e.g. via a magnetic Feshbach resonance [Chi10], or by designing the external potential landscape seen by the atoms thanks to light and magnetic fields engineering.

The level of control was even improved when ultracold bosonic and fermionic atoms were stored in artificial periodic potentials, created by standing waves of light, namely optical lattices. The use of optical lattices opens the doors for studying the strongly-interacting regime (via the introduction of a large effective mass to the atoms, mitigating their kinetic energy) and probing fundamental questions of interdisciplinary fields of research by its similarities to electrons in solid crystals. A first pioneering experiment with optical lattice was the observation of the transition from the superfluid to the Mott insulator phase, with bosonic atoms [Gre02]. This experiment demonstrated also the possibility to describe cold atoms in optical lattice with a relative simple Hamiltonian, the Bose-Hubbard model, and thus reconnect to the idea of quantum simulation to solve solid-state problems. From that experiment, several works have reported a non standard Hubbard model [Dut14] or the experimental realization of an antiferromagnet in the Hubbard model, with a quantum gas microscope [Maz16], offering the potential to answer the regime of the doped Hubbard model.

Recently, a new class of atomic species has been brought to quantum degeneracy, namely the magnetic lanthanides, which triggered a huge interest in particular in the prospect of quantum simulation because of the distinct properties of these atoms. In particular, the lanthanides have the largest magnetic moment in the periodic table and thus bring an additional ingredient to the system, implementing long-range and anisotropic dipole-dipole interactions (DDI) between the particles. Lanthanide experiments open fascinating possibility to study the impact of the DDI on few and many body quantum physics. The ERBIUM experiment in Innsbruck (AT) produced the first BEC and dFg of erbium (Er) atoms. The combination of dipolar quantum gases and optical lattices provides a powerful platforms to study strongly correlated quantum system beyond standard Bose-Hubbard model. Recently, the group realized an extended Bose Hubbard model featuring both onsite and offsite interactions [Bai12] in dealing with the long-range nature of interaction in dipolar bosonic atoms.

In this thesis we investigate the preparation of a spinor quantum gas of Er atoms. Preparing a deterministic spin mixture can be particularly challenging for a high-spin system as Er. The ground state of Er has a total angular momentum $J=6$ ($F=19/2$) giving rise to 13 (20) different spin states for bosons (fermions). At our typical magnetic field strength, the Zeeman splitting for the bosonic isotopes between adjacent spin states is equal; hence a deterministic preparation of one particular spin state is not possible with standard methods such as radio-frequency (RF) coupling. In this work, we show how the quadratic Zeeman shift enables us, in the fermionic case, to obtain a deterministic spin preparation with RF pulse or RF sweep. We in particular demonstrate and experimentally implement a versatile

preparation of a mixture of two spin states. Several unexplored phases are predicted to occur with a spin mixture of highly magnetic atoms in a deep lattice, e.g. stripe phase [Maz17]. Before searching for such new phases in our experiment, to characterize the system we load the fermionic isotope into a deep lattice, and we extract the onsite interaction by lattice modulation spectroscopy measurements between the lowest spin states. Additionally, as a step towards the predicted phases, we present a method to obtain a deterministic spin preparation and a single-spin-state control, which exploits the tensorial ac-Stark shift and can be implemented for both fermionic and bosonic isotopes. For this aim, I developed an External Cavity Diode Laser (ECDL) source, emitting close to a narrow transition at 631 nm, together with an optical setup that allows different schemes for spin manipulation. This study provides new elements to increase the knowledge of our system and opens the door to investigate the stability of ordered magnetic phases.

The structure of this thesis is the following:

Chapter 1 introduces the main properties of Er, based on its high magnetic moment and the long-range and anisotropic nature of the interactions.

Chapter 2 describes the ERBIUM experimental apparatus and then focuses on the methods adopted to realize a spinor gas of Er.

Chapter 3 investigates a system of fermionic Er atoms into a deep optical lattice and presents the consecutive measurements of the onsite interaction, and the extracted scattering length, between the two lowest spin states.

Chapter 4 introduces the theory and calculations of the AC-Stark shift, then it describes the realization of a laser source at 631 nm and the related optical setup developed during my thesis work. Finally, it presents an overview of different methods to achieve a deterministic spin preparation with light and the manipulation at the single-spin-state level in Er.

Chapter 1

Erbium properties

Erbium (Er) is an element of the periodic table, and it is one of the so called rare earth elements (REE). The adjective "rare" is much more indicative of the history related to the erbium's discovery (1788) rather than its real properties, since for many years these elements could only be found in a miner in Ytterby (Sweden). Erbium is present on the entire earth crust with a concentration of 3.4 ppm [Lid10]. Nevertheless, the price of pure erbium is high for several reasons. First, it is difficult to find REE at high concentration in a single location; second they are not found as pure elements but mixed together and finally, due to the monopoly of market run by China¹.

Erbium has 5 stable bosonic isotopes and 1 stable fermionic isotope. The masses of such isotopes range from 162 amu to 170 amu. Table 1.1 shows the abundances and statistics of stable Er isotopes.

Table 1.1: Relative abundances and type of quantum mechanical statistics for all stable erbium isotopes.

isotope	¹⁶² Er	¹⁶⁴ Er	¹⁶⁶ Er	¹⁶⁷ Er	¹⁶⁸ Er	¹⁷⁰ Er
abundance	0.14%	1.61%	33.6%	23.0%	26.8%	15.0%
statistics	boson	boson	boson	fermion	boson	boson

The high abundance of the fermionic isotope paves the way for studying dipolar fermionic quantum gases. This chapter is devoted to the basic properties of erbium. The first section introduces the electronic configuration and the energy spectrum with the description of the principal atomic transitions used in the experiment. The second section is dedicated to the Zeeman splitting induced by an external magnetic field, which is fundamental for the

¹China has the largest rare earth reserves in the world; the industrial reserves occupy first place (76%) and it is the major producer of REE for the world market.

understanding of the spin preparation and manipulation. Finally, the last section introduces the interaction properties of Er atoms.

1.1 Electronic configuration and energy spectrum

In the ground state, the electronic configuration of Er is written as below:

$$(1s^2 2s^2 2p^6 3s^2 3p^6 3d^{10} 4s^2 4p^6 4d^{10} 5s^2 5p^6) 4f^{12} 6s^2, \quad (1.1)$$

where the terms in the round brackets represent the electronic configuration of xenon. In fact it is often abbreviated as

$$[Xe] 4f^{12} 6s^2 \quad (1.2)$$

According to the Madelung's rule, this electronic configuration presents an open 4f shell shielded by a completely filled 6s. For this reason, it is usually referred as a *submerged-shell* [Jen91] and it is expected to give rise to exciting unexplored physical scenarios. The motivation behind this has to be searched in the anisotropy of the electronic density distribution of the 4f shell, which leads to a large magnetic moment. Only the incompletely filled shell contributes to the quantum number of the ground state, which can be obtained using Hund's rule and LS (Russel-Saunders) coupling scheme. The 4f shell has 7 m_ℓ states filled by only 12 electrons, which arrange each other to maximize the total spin $S = 2 \times 1/2 = 1$ and the orbital angular momentum $L = 2 + 3 = 5^2$.

m_ℓ	-3	-2	-1	0	+1	+2	+3
m_s	$\uparrow\downarrow$	$\uparrow\downarrow$	$\uparrow\downarrow$	$\uparrow\downarrow$	$\uparrow\downarrow$	\uparrow	\uparrow

Using the spin-orbit coupling³ the total angular momentum quantum number can be calculated as $J = S + L$ and the ground state, denoted by $^{2S+1}L_J$ in the Russell-Saunders notation, reads:

$$\text{ground state : } ^3H_6 .$$

²In the LS coupling the spins of the single electrons have to be added to get the total spin S and the individual orbital angular momenta as well, to obtain the orbital angular momentum L. Only then L and S couple to give the total angular momentum J. It is assumed that spin-spin interaction > orbit-orbit interaction > spin-orbit interaction.

³The LS coupling scheme is applicable only for the ground state. Due to the heavy mass, the spin-orbit interactions get important with respect to the Coulomb interactions and the JJ-coupling scheme has to be used for the other levels.

This ground state has high angular momentum, which will affect the interactions properties.

1.1.1 Energy spectrum

Figure 1.1 shows the energy spectrum of erbium up to 25000cm^{-1} . The complexity arises

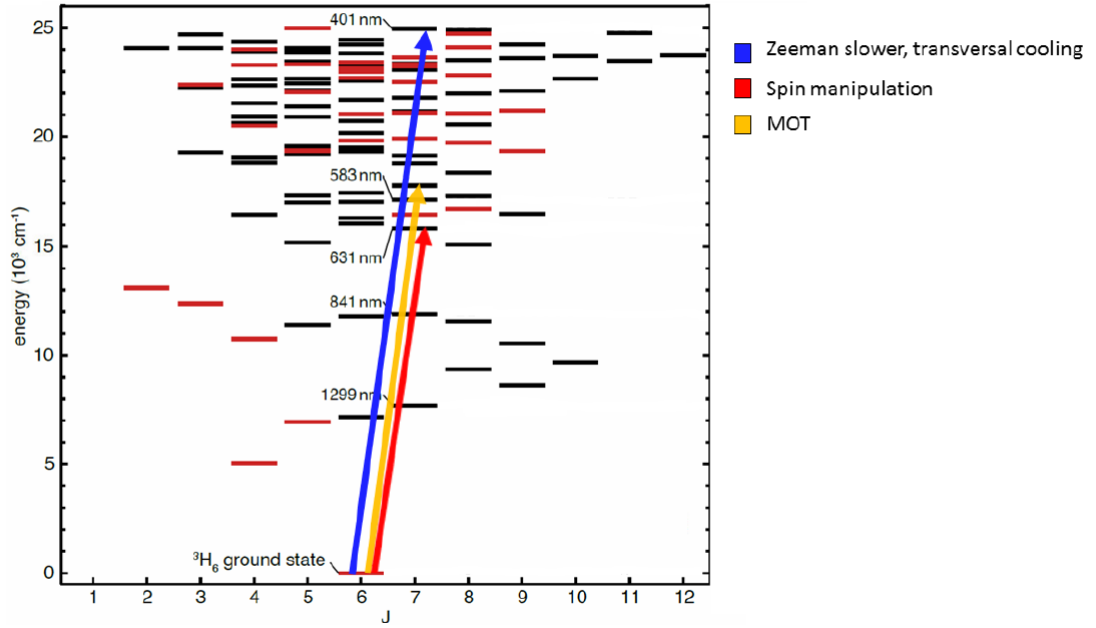


Figure 1.1: Energy level scheme of erbium up to an energy of $E = 25000\text{cm}^{-1}$. The full level scheme is presented in [Fri14]. States with even (odd) parity are shown in red (black). The three most important transitions for the ERBIUM experiment are at a wavelength of 401 nm (blue), 583 nm (yellow) and 631 nm (red). The blue transition is used for the Zeeman slower (ZS), transversal cooling (TC) and imaging. The yellow transition is used for creating the magneto-optical trap (MOT), whereas the red transition will be used for spin manipulation.

from the electronic configuration, which due to the submerged shell nature, allows the electrons to be excited to higher energy levels in many different ways. Indeed, not only the valence electrons of the 6s shell can be excited, but also the valence electrons of the 4f shell. Focusing on the electric dipole transitions, it is possible to find different lines available for laser cooling and ultracold atom applications, whose linewidths range from Hz to MHz. The most important transitions for our experiment are shown in Fig. 1.1.

The blue line in Fig. 1.1 at 401 nm involves the transition of one electron from the 6s orbital to the 6p orbital in a singlet state. This is a strong transition with a broad linewidth (30 MHz) convenient⁴ for the first stage of cooling, based on transversal cooling and Zeeman slower. Moreover, this light is used for the imaging of the atomic cloud.

The yellow transition at 583 nm is an intercombination line, where one of the electrons of the 6s orbital gets promoted in the 6p state, but this time in a triplet state. This line is weaker with respect to the blue line because, since involves a change of the spin, is semi-forbidden. The narrow linewidth of about 190 kHz is ideal for realizing the magneto-optical trap (MOT) light. As described in [Fri12], the MOT capture velocity with this linewidth is sufficiently high to trap atoms coming from the Zeeman slower and reach temperature as low as 10 μ K.

The red transition at 631 nm involves the excitation of an electron coming from the 4f shell. Due to the completely filled 6s shell, the electrons of the 4f shell are shielded. Very narrow transitions can be found with electrons coming from the 4f shell and arriving at the 5d shell (also shielded by the 6s). The transition at 631 nm has a linewidth \simeq 20 kHz but linewidths as narrow as 2 Hz are present in the spectrum. Part of the work of this thesis is focused on the realization of a laser source, emitting at this wavelength, which can be used for a deterministic control of the atomic spins, see Chapter 4.

1.1.2 Hyperfine structure

Among the erbium isotopes, bosons have a zero nuclear spin, $I = 0$, whereas the fermions have $I = 7/2$, which couples with the total angular momentum J leading to the hyperfine structure[Bra83]. For the ^{167}Er isotope, the already complex energy level scheme becomes even more complicated due to the removal of the degeneracy caused by the hyperfine splitting expressed as

$$\Delta E_{hfs} = AC + B \frac{3/2C(2C+1) - I(I+1)J(J+1)}{2I(2I-1)J(2J-1)}, \quad (1.3)$$

where A and B are the hyperfine structure constants and $C = \frac{1}{2}(F(F+1) - J(J+1) - I(I+1))$, with F the total angular momentum quantum number. For erbium, $F = 19/2$ gives eight hyperfine states from $F = J+I = 19/2$ to $F = J-I = 5/2$.

⁴A broad transition is usually suited for application in which a large number of scattering events are needed as transversal cooling, Zeeman slower and imaging.

1.2 Interaction with magnetic fields

The Zeeman effect consists in the separation of the spectral lines due to an external magnetic field (B). In particular the lines are splitted due to the interaction of the B field with the magnetic moment of the atoms. The goal of this section is to explain the behavior of atomic lines in presence of an external magnetic field and how this changes in the bosonic and fermionic case.

1.2.1 Magnetic moment

For bosons the atomic magnetic moment μ is given by:

$$\mu_{\text{Boson}} = g_J \mu_B \sqrt{J(J+1)}, \quad (1.4)$$

where g_J is the Landé g-factor and μ_B is the Bohr magneton. The component along the direction of the magnetic field is

$$\mu_{\text{Boson}}(z) = -m_J g_J \mu_B, \quad (1.5)$$

where m_J is the magnetic quantum number and it can assume the following $2J+1$ values:

$$[-J, -(J-1) \dots 0 \dots (J-1), J]. \quad (1.6)$$

For the fermionic isotope, which has an hyperfine structure, the total angular momentum J couples with the nuclear momentum I and the total angular momentum F has to be considered to calculate the magnetic moment:

$$\mu_{\text{Fermion}}(z) = -m_F g_F \mu_B. \quad (1.7)$$

It is clear that the Landé g-factor is needed in order to obtain the magnetic moment.

1.2.2 Landé g-factor

In the LS-coupling, the Landé g-factor for the ground state reads

$$g_J = 1 + (g_S - 1) \left[\frac{J(J+1) - L(L+1) + S(S+1)}{2J(J+1)} \right], \quad (1.8)$$

where $g_s \approx 2.00232$ is the gyromagnetic ratio. Using $J = 6$, $L = 5$ and $S = 1$, we find for the ground state

$$g_J(J = 6, L = 5) = 1.167053. \quad (1.9)$$

On the other hand, the most precise experimental value is [Fri14].

$$g_J = 1.163801(1). \quad (1.10)$$

The discrepancy between the two values can be explained by different reasons [Jud61]. First, deviation from totally L-S coupling. Second, the relativistic corrections necessary due to the kinetic energy of the electron in higher shells, and finally diamagnetic effects. The magnetic moment can now be estimated for the ground state of bosonic erbium isotopes ($J=6$) considering a spin polarized sample in $m_J = -6$

$$\mu_{\text{Atom}}(z) = -6.982806(6) \mu_B. \quad (1.11)$$

This incredibly high value is not common in the periodic table and after terbium, dysprosium and holmium is the highest value one can find.

For the excited states, the jj -coupling has to be considered. In the case of jj -coupling, first the orbital angular momentum l and the spin s of each electron couple to form a total angular momentum j , then all the single-electron j sum up to the total angular momentum of the atoms J . Two particular cases of this coupling are $J_1 J_2$ and $J_1 j$ that are often used for the excited states of lanthanide atoms. In this scheme, all the inner electrons up to the 4f-shell couple together in the standard LS-coupling giving out J_1 , and then couple to the outer lying electrons via $J_1 J_2$, if these couple among themselves via LS (as for $[Xe]4f^{12}(3H_6)6s6p(1P_1)$)⁵, or via $J_1 j$ if the 6s electronic shell remains filled (as for $[Xe]4f^{11}(4I_{13/2})5d6s^2$)⁶. In the case of jj -coupling, an estimate of the Landé g-factor can be obtained using the following relation

$$g_J = g_{J_1} \frac{J(J+1) + J_1(J_1+1) - J_2(J_2+1)}{2J(J+1)} + \quad (1.12)$$

$$+ g_{J_2} \frac{J(J+1) + J_2(J_2+1) - J_1(J_1+1)}{2J(J+1)},$$

where $J_2 = j$ in case of $J_1 j$ -coupling. Table 1.2 gives the Landé g-factors found for the ground state and the three excited states shown in Fig. 1.1. The most precise values are taken from [Mar78], where the three corrections are taken into account.

⁵This is the electronic configuration of the 401 nm light shown in Fig. 1.1

⁶This is the electronic configuration of the 631 nm light shown in Fig. 1.1

Table 1.2: Landé g_J of the ground state and the excited states of bosonic erbium including the values with corrections.

electronic configuration	Wavelength (nm)	g_J value from Eq. 1.12	g_J value from Ref.[Mar78]
[Xe]4f ¹² 6s ²		1.167	1.164
[Xe]4f ¹² (³ H ₆)6s6p(¹ P ₁)	401	1.143	1.160
[Xe]4f ¹² (³ H ₆)6s6p(³ P ₁)	583	1.215	1.195
[Xe]4f ¹¹ (⁴ I _{13/2})5d6s ²	631	1.090	1.070

In the case of fermionic ¹⁶⁷Er, since the nuclear spin I is not zero, the magnetic moment of the nucleus couples to the magnetic field produced by the electrons of the atom. As a result, the gyromagnetic ratio has to be calculated according to the following relation:

$$g_F = g_J \frac{F(F+1) - I(I+1) + J(J+1)}{2F(F+1)}, \quad (1.13)$$

where g_J is given by Eq.(1.12). Using the most precise experimental value for g_J , it is possible to estimate the g_F factor and the magnetic moment for the ground state of the fermionic isotope:

$$g_F = 1.163801 \frac{\frac{19}{2}(\frac{19}{2} + 1) - \frac{7}{2}(\frac{7}{2} + 1) + 6(6 + 1)}{19(\frac{19}{2} + 1)} = 0.735032(1), \quad (1.14)$$

$$\mu_{\text{Fermion}}(z) = -6.982804(4) \mu_B, \quad (1.15)$$

where Eq. (1.7) was used considering the fermionic spin polarized ground state ($F = 19/2$; $m_F = -19/2$).

1.2.3 Zeeman splitting

By applying an external magnetic field, the degeneracy of the energy levels is removed creating several magnetic-sublevels. Let's consider two separately cases: bosonic and fermionic atoms of erbium.

For bosonic erbium isotopes, the lack of nuclear spin allows a straightforward argumentation. The energy level with total angular momentum J splits into $2J + 1$ levels with magnetic quantum number m_J . The effect of the external magnetic field is given by the following term in the Hamiltonian:

$$\hat{H}_{Bosonic} = \mu_B(g_S \hat{\mathbf{S}} + g_L \hat{\mathbf{L}}) \cdot \mathbf{B}. \quad (1.16)$$

From which, for standard magnetic fields used in ultracold atom experiments⁷, the Zeeman energy shift is linear and it reads:

$$\Delta E_{m_J} = g_J m_J \mu_B B. \quad (1.17)$$

Considering two different consecutive spin states, e. g. $m_J = -6$ and $m_J = -5$, the degeneracy present at $B = 0$ G is now removed and the splitting is of 1.628879 MHz for each Gauss of magnetic field applied⁸. The same splitting is also present for all adjacent spin states

$$\Delta E_{m_{J'}} - \Delta E_{m_{J'+1}} = \Delta E_{m_{J'+1}} - \Delta E_{m_{J'+2}}. \quad (1.18)$$

In the fermionic case (¹⁶⁷Er), the hyperfine structure modifies the Zeeman interaction due to the nuclear spin:

$$\hat{H}_{B_{Fermionic}} = \mu_B (g_S \hat{\mathbf{S}} + g_L \hat{\mathbf{L}} + g_I \hat{\mathbf{I}}) \cdot \mathbf{B}. \quad (1.19)$$

In the case of weak magnetic fields, where the Zeeman energy shift is much smaller than the hyperfine scale, the Zeeman interactions can be treated as a perturbation in the $|F, m_f\rangle$ basis. In this case the Zeeman energy shift can be approximated to be linear:

$$\Delta E_Z(B) = m_F g_F \mu_B B. \quad (1.20)$$

Considering two different adjacent spin states, e.g. $m_F = -19/2$ and $m_F = -17/2$, the degeneracy present at $B = 0$ G is now removed and the magnetic sublevels are separated by 1.025409 MHz for each Gauss of magnetic field applied.

For higher B fields⁹, I and J fully decouple, leading to the Paschen-Back effect. In this framework an exact diagonalization of the Hamiltonian is needed. Figure 1.2 shows the effect of the B field on the hyperfine ground state $F = 19/2$. In this plot it is hard to notice the quadratic dependence of the Zeeman splitting at high B fields. On the other hand, if we consider the three adjacent spin states: e.g. $m_F = 19/2$, $17/2$ and $15/2$, then the splitting between the first two $\Delta E_{19/2-17/2}$ with respect to the following two $\Delta E_{17/2-15/2}$

⁷The range in which the Zeeman energy shift is linear in the case of $I = 0$ depends on the energy shift given by the fine structure, which are large for lanthanides. In fact the result of Eq. (1.17) can be used for $B \ll \Delta_{fs} \frac{\hbar}{\mu_B} g_J \approx 500$ T since $\Delta_{fs} \approx h \times 1$ PHz. The energy scales to be compared are the Zeeman splitting and the fine structure splitting.

⁸To obtain this result, the g_J value was taken from expression (1.10).

⁹The range in which the Zeeman energy shift is linear, in the case of $I \neq 0$, depends on the hyperfine energy shift which are much smaller than the fine ones. Indeed, the result of Eq. (1.20) can be used for $B \ll \Delta_{hfs} \frac{\hbar}{\mu_B} g_F \approx 5$ G since $\Delta_{hfs} \approx h \times 1$ GHz.

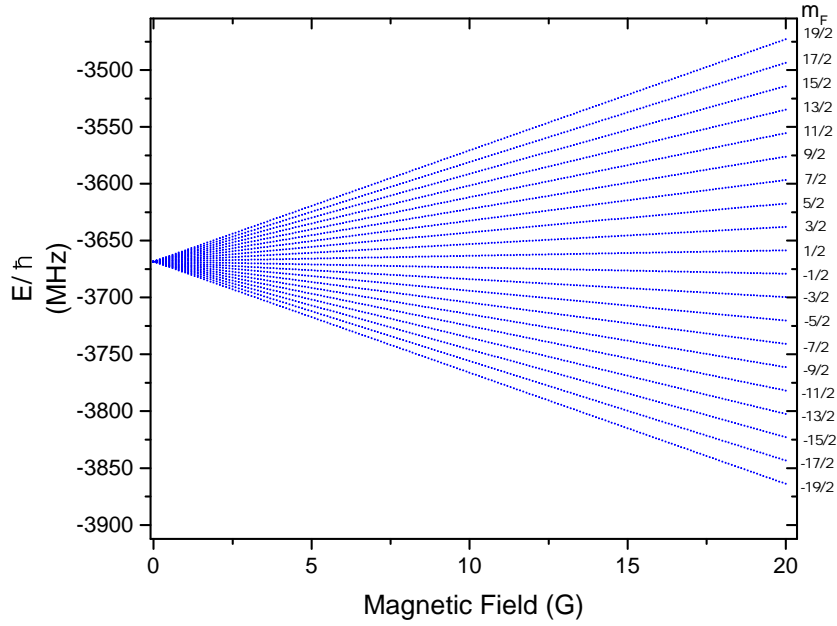


Figure 1.2: Effect of the Zeeman splitting on the $F=19/2$ manifold. The resulting states are evaluated from exact diagonalization of the Hamiltonian.

becomes unequal due to the quadratic dependence. This can be visualized in Fig. 1.3 from the difference of the two splitting: $\Delta E_{19/2-17/2} - \Delta E_{17/2-15/2}$.

1.3 Interactions properties

Despite cold gases are dilute systems, the inter-particle interactions are crucial in determining the scattering properties. The two-body interactions in erbium can not be described using only the contact interaction [Lah09], but, due to the high magnetic moment, also the dipole-dipole interaction (DDI) plays a fundamental role. In the following, short-range contact interaction and the long-range dipole-dipole interaction are briefly introduced.

1.3.1 The contact interactions

Two atoms at a separation distance r feel an interaction potential $U(r)$ which, in a first order approximation, is the so-called van der Waals potential

$$U_{vdW} = -\frac{C_6}{r^6}, \quad (1.21)$$

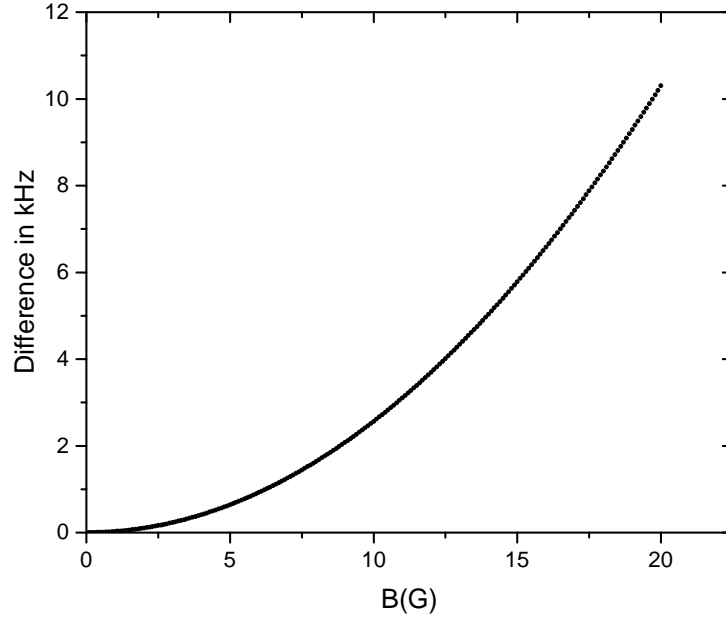


Figure 1.3: Effect of quadratic Zeeman splitting on the difference of the separation between adjacent spin states $\Delta E_{m_F+2-m_F+1} - \Delta E_{m_F+1-m_F}$.

where C_6 is the van der Waals coefficient. This potential results in a short-range and isotropic character. For a classical picture of the scattering between two particles, consider Fig. 1.4, in which two atoms are colliding with incident momentum p and impact parameter b . The angular momentum reads

$$L = |\mathbf{r} \times \mathbf{p}| = bp = \hbar l, \quad (1.22)$$

where l represents the partial wave number. As a condition for the scattering to be relevant, the impact parameter has to be much smaller than the interactions range r_0 , leading to the following condition

$$b \ll r_0 \rightarrow l \ll \frac{2\pi r_0}{\lambda_{\text{dB}}}, \quad (1.23)$$

where $\lambda_{\text{dB}} = \frac{h}{p}$ is the de Broglie wavelength. In the limit of low collisional energy, i. e. low momentum p , the only solution is a s -wave collision ($l = 0$). In this situation, the van der Waals potential can be approximated by the pseudo-potential

$$U_{\text{contact}}(\mathbf{r}) = 4\pi \frac{\hbar^2 a}{m} \delta(\mathbf{r}), \quad (1.24)$$

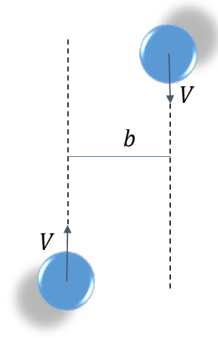


Figure 1.4: A scattering process of two neutral atoms. The two colliding atoms have a relative velocity of $2v$ and they are approaching each other with an impact parameter b which determines their relative angular momentum.

where $\delta(\mathbf{r})$ is the Dirac delta function and the only important parameter is a , the *s-wave* scattering length.

1.3.2 The magnetic dipole-dipole interactions

In dipolar gases, beside the contact interaction, one has to consider DDI. For two atoms with a magnetic moment μ_1 and μ_2 pointing in the direction \mathbf{e}_1 and \mathbf{e}_2 , respectively, the DDI reads as

$$U_{\text{DDI}}(\mathbf{r}, \mathbf{e}_1, \mathbf{e}_2) = \frac{\mu_0 \mu_1 \mu_2}{4\pi} \frac{(\mathbf{e}_1 \cdot \mathbf{e}_2)r^2 - 3(\mathbf{e}_1 \cdot \mathbf{r})(\mathbf{e}_2 \cdot \mathbf{r})}{r^5}, \quad (1.25)$$

where $|\mathbf{r}|$ is the distance between the atoms and μ_0 the magnetic permeability of free space. By applying a magnetic field, the dipoles align themselves along the quantization axis given by the direction of the external field. The interaction between two polarized atoms can be simplified and described by only two parameters: the distance r and the angle θ between \mathbf{r} and the quantization axis,

$$U_{\text{DDI}}(\mathbf{r}, \theta) = \frac{\mu_0 \mu_1 \mu_2}{4\pi} \frac{1 - 3\cos^2 \theta}{r^3}. \quad (1.26)$$

The result is a tunable interaction whose tunability is given by the angle θ . In fact, the term $(1 - 3\cos^2 \theta)$ can assume values ranging between -2 and 1 , going from an interaction maximally attractive when $\theta = 0^\circ$ (*head-to-tail configuration*) to maximally repulsive when $\theta = 90^\circ$ (*side-by-side configuration*). It is worth noticing that the DDI can also be tuned to zero for the magic angle $\theta = 54.7^\circ$. Due to the θ dependence and the scaling as r^{-3} , DDI are anisotropic and long-range in a 3-dimensional system. In the presence of DDI, the elastic scattering processes between atoms can radically change. In the following we will only

briefly discuss why this can affect the physics of spinor gases. In a contact-type collision (s-wave), which is spin-independent, atoms exit the scattering with no net relative angular momentum. After the interaction their total spin is conserved, but not necessarily the spin of the single atom (*flip-flop*).

On the other hand, in a dipole-dipole-type of collision, due to the long-range nature, atoms do not preserve the relative angular momentum, but rather only the total angular momentum. Thus, the total spin is not conserved.

Chapter 2

Production of spinor Er quantum gases

A system composed of BECs or dFgs, occupying different Zeeman sublevels is usually referred as “spinor” quantum gas [Sta13].

The aim of this chapter is to describe the techniques adopted to realize an ultracold spinor erbium gas. In the first and second section we give an overview of the vacuum apparatus and main procedure for the production of a degenerate quantum gas. Finally, the last section describes the techniques usually adopted to generate a spinor gas.

2.1 Experimental setup

An overview of the machine is shown in Fig. 2.1. In the figure two different pressure regions are highlighted. The High Vacuum (HV) section maintains a pressure of about 4×10^{-9} mbar while the Ultra High Vacuum (UHV) section maintains a pressure of 1×10^{-11} mbar. The two parts are connected to each other by a differential pumping tube, which provides a pressure gradient of up to three orders of magnitude. We now briefly review the main production steps.

Erbium travel in the high vacuum section A commercial diffusive oven, where solid pieces of Er evaporate at a temperature of 1100°C , realizes an erbium atomic vapor. Then, from the vapor, a set of apertures, forming the so-called hot lip and usually heated at 1200°C , produces the collimated atomic beam. Atoms exiting the oven are additionally optically collimated by a 2D transversal cooling stage made by two retro-reflected laser beams, operating at 401 nm (broad transition of erbium). Figure 2.1 displays in blue the two beams, crossing each other at an angle of 90° . This stage enhances the atomic flux in the longitudinal direction. The atomic beam travels then towards the Zeeman slower.

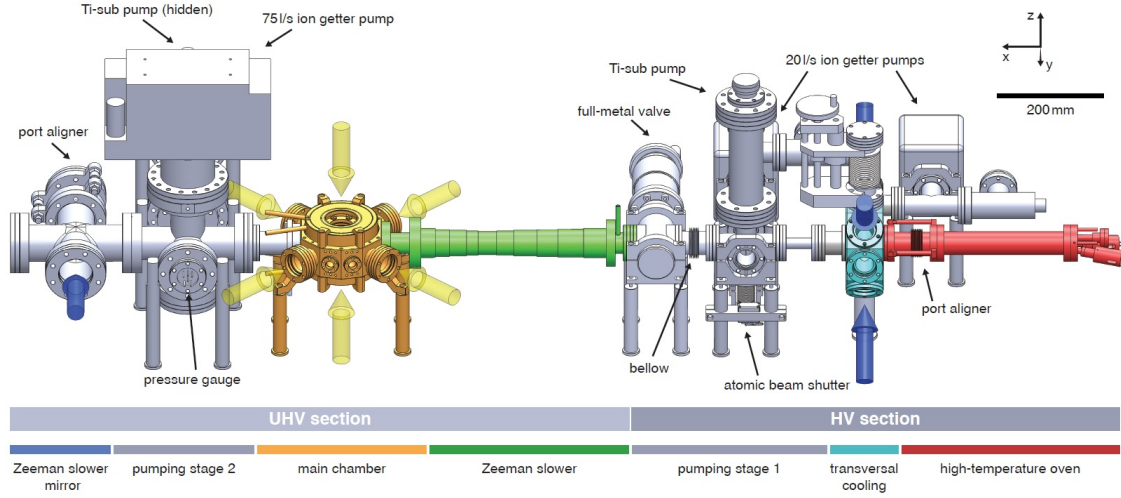


Figure 2.1: The erbium apparatus (picture taken from[Fri14]). The figure points out the presence of two sections. The HV section on the right is used to realize a collimated atomic beam while the UHV section to slow down the atoms and finally reach the degeneracy conditions in the main chamber.

Slowing down, cooling and trapping in the Ultra High Vacuum section Along the differential pumping tube, connecting the HV to UHV section, atoms are cooled down using the Zeeman slower. The basic idea is to use combination of Zeeman effect and large radiative pressure from laser light to reduce the velocity of the atoms down to the MOT capture velocity. This is implemented by shining a 401 – nm beam collinear and counterpropagating to the atomic beam. Due to the broad linewidth of the 401nm transition, a large number of scattering events happen during the travelling time of the atoms in the Zeeman Slower. During one of this event, the atom by absorbing a photon, receives a momentum kick in the direction of light propagation while its internal state is promoted to the excited state of the 401nm-transition. The atom decays back to its internal ground state by spontaneously emitting a photon isotropically in space. Thus, due to the high number of events, the average change of the momentum given by the emission vanishes, resulting in a overall slowing process. The reduction of the velocity makes the light off resonant due to the Doppler shift. Several coils are positioned to create an inhomogeneous magnetic field which leads to a space-dependent Zeeman shift. This compensates the Doppler shift and keeps the atoms always resonant with the light.

When atoms approach the main chamber, shown in yellow in Fig. 2.1, they are already slow enough to be trapped into the MOT. The MOT combines laser cooling with a position dependent force to trap the atoms. The idea consists in the use of two counter-propagating laser beams, for the three directions, of momentum k_L and $-k_L$ with frequency ω_L detuned

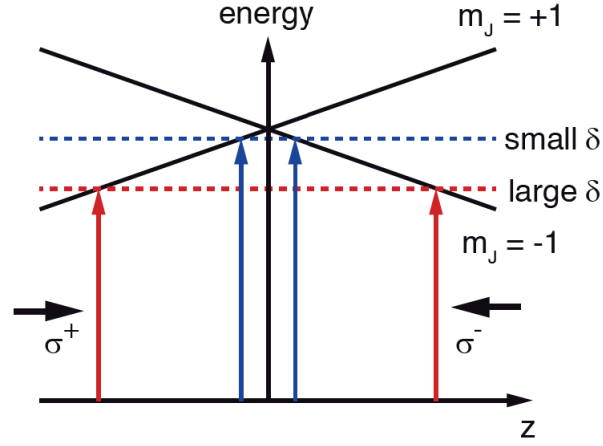


Figure 2.2: (a) Simplified 1D version of a MOT (picture taken from[Fri14]) for a two-level atom with $J=1$ excited state and $J=0$ ground state that coincide with the z axis. The B field gradient splits the excited state in the magnetic sublevels. For $J=1$ only three sublevels are present and the atom can be excited in these levels with the right polarization. Exploting σ^+ and σ^- polarized photon only the two level $m_J = \pm 1$ are involved in the transition. In the picture the spatial effect of reducing the detuning is also illustrated.

from the atomic resonance (ω_a). Similar to the Zeeman slower case, the resonant condition for the beam of momentum \mathbf{k}_L is met for atoms whose velocity \mathbf{v} is such that $\mathbf{k}_L \cdot \mathbf{v} = \omega_L - \omega_a$ and the absorption of photon from this beam is most likely for atom with this velocity. Then, by detuning $\omega_L < \omega_a$ (red detuning), the atoms are always most likely to scatter light from the beams against which they propagate $\mathbf{k}_L \cdot \mathbf{v} < 0$ and the net force is always opposite to the velocity and null if the atoms are at rest (friction force). This simple configuration is not a trap. The atoms, indeed, feel a force that is velocity dependent but not space dependent. Thus, the configuration with six beams can be seen more as a optical molasses rather than a trap for the atoms. To correct for this and obtain a trap, the three retro-reflected laser-beams are combined to a quadrupole magnetic field and a special choice of light polarization is made [Raa87] (MOT). Figure 2.2 shows a simplified 1D sketch of the mechanism of a MOT, approximating the atom to a two-level system with $J=0$ and $J'=1$ ground and excited states. The quadrupole field induces a position-dependent Zeeman shift for the different magnetic sublevels (quantum number m'), cancelling at $z = 0$. The two counterpropagating beams are chosen of polarization σ_{\pm} so that they selectively excite the atom to $m' = \pm 1$, respectively. Thus, atoms displaced to the right with respect to the central position of the trap absorb more probably photons coming from the beam σ^- polarized propagating towards the left, and vice-versa for a displacement to the other side of the trap. Hence, they always receive a kick (due to the linear momentum carried by photons) opposite with respect to their displacement.

The result is a tunable trap, since it is also possible, after trapping the atoms, to reduce the detuning of the MOT beams with respect to the transition and compress the atomic cloud (see blue arrows in Fig. 2.2). In the case of Er, several optical transitions can in principle be used to generate a MOT. Our experiment uses the 190 kHz linewidth transition at 583 nm. This narrow linewidth leads to a Doppler temperature $T_D = \frac{\hbar\Gamma}{2k_B}$ of 4.6 μ K which enables a direct loading of the optical dipole trap (ODT) from the MOT. For heavy atoms as erbium, the gravitational sag associated with the use of large detuning of the MOT light makes that the sample get automatically spin polarized in the lowest spin states $m_F = -19/2$ or $m_J = -6$ for the fermionic and bosonic case, respectively. The choice of narrower transitions can help to reach very low temperatures but a trade off has to be chosen because also the capture velocity will dramatically be reduced.

2.1.1 Reaching quantum degeneracy

From the MOT, we load the atoms into a single-beam optical dipole trap (ODT). Matching the aspect ratio of the dipole trap to the atomic cloud in the MOT via a scanning system, see Refs. [Bai12; Ahm05], enables to achieve a maximum loading efficiency of 35%. The scanning system allows a change of the horizontal beam waist by rapidly scanning the frequency of an AOM, whose first order is used for the ODT. After loading, atoms are transferred into a crossed ODT and cooled down to the degeneracy using evaporative cooling [Ket96]. The idea of cooling by evaporation consists of removing the high-energetic atoms from the sample and to allow the remaining atoms to rethermalize to a lower temperature via elastic collisions. This process requires the atoms to collide and that the elastic collision rate (enabling rethermalisation) is much larger than the inelastic one (limiting the lifetime of the sample). This is achieved in cold atom experiments by truncating the confining potential to a certain depth U , which we slowly decrease. Reaching a degenerate quantum gas is not only a matter of temperature, rather, the important parameter is the phase space density (PSD), defined as:

$$\text{PSD} = n\lambda_{\text{dB}}^3, \quad (2.1)$$

where n is the peak density of the gas and λ_{dB} is the De Broglie wavelength. For a thermal cloud, atoms follow the Maxwell-Boltzmann energy distribution and the peak density n can be calculated from the total atom number N , once the trap frequencies and the temperature T are known, by using this expression:

$$n = N\bar{\omega}^3 \left(\frac{m}{2\pi k_B T} \right)^{\frac{3}{2}}, \quad (2.2)$$

where $\bar{\omega} = (\omega_x \omega_y \omega_z)^{1/3}$ is the geometrical mean trap frequency, k_B is the Boltzmann constant and m is the mass of the chosen isotope. The condition to reach the phase transition from a thermal sample to a degenerate quantum gas is $\text{PSD} > 1$ [Pit16]. It is important to carefully choose the parameters of the evaporation ramp (of the ODT depth) and the trap frequencies $\omega_{x,y,z}$, in order to remove only the hottest atoms. Indeed, it is important that the ramp is slow enough, and the density high enough (and thus its elastic collision rate) so that the system has time to rethermalise. It is also necessary to have a good ratio between elastic and inelastic collisions, since the latter will lead to atom losses. Furthermore, increasing the PSD requires to compete the decreases of temperature with respect to the atom number.

In our lab the first Bose-Einstein condensate and degenerate Fermi gas of erbium was obtained in 2012 and 2013, respectively, exploiting the evaporative cooling technique [Aik12]. Indeed, in the case of dipolar gases, a significant elastic cross section persists at low temperatures also for a Fermi gas due to the universal character of dipolar scattering [Bon09].

2.2 Overview on spin preparation

The peculiarity of spinor Er gases derives essentially from two characteristics. First, high spin systems as Er can lead to the possibility of investigating disparate magnetically ordered states, such as [San06; Lia12] for bosons and stripe-phase [Maz17], d-wave superfluidity [Bar04] for fermions. Second, DDI plays an important role in driving process where the spin is not conserved. Several difficulties need to be overcome to reach these unexplored quantum states, e.g. deterministic control of the population of the Zeeman sublevels. Thus, it is helpful to reduce the complexity of the system from 13 (20) spin states for bosonic (fermionic) isotopes, to an effective spin 1/2 or spin 1 system. This can be realized by exploiting the Zeeman effect or AC-stark shift, which depends nonlinearly on the different magnetic sublevels. In addition, a good control of the B-fields is often necessary, making the study of these systems even more challenging. For this purpose the AC-noise has to be reduced and the DC value stabilized with high care. In the following subsections, we give an overview of the techniques usually utilized to realize a spin mixture in the experiment. The techniques introduced are two: RF pulse and the Landau-Zener Sweep.

2.2.1 Direct radio-frequency excitation of the Zeeman sublevels

Consider a sample of Er atoms in the lowest spin state interacting with a static field \vec{B}_0 , parallel to the z-axis, and a radio-frequency field $\vec{B}_1 \cos(\omega t)$, along the x-axis. The radio-frequency (RF) field can be decomposed along z in a superposition of a counterclockwise

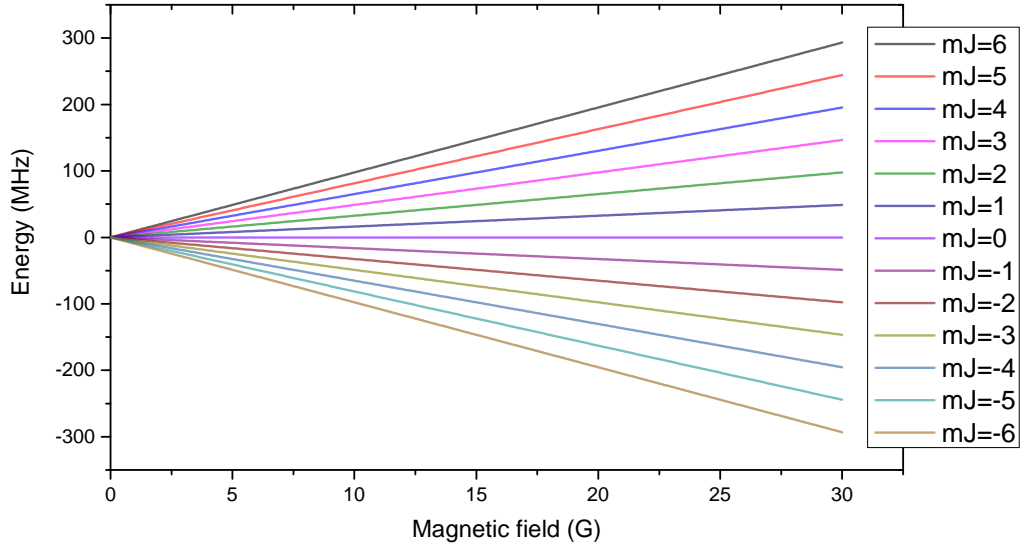


Figure 2.3: Zeeman splitting up to 30 G for the ground state $J=6$ of the bosonic isotopes. The splitting gives rise to 13 magnetic sublevels. According to the formula (1.17) the splitting is linear in the magnetic field range usually used in ultracold-atoms experiments.

and clockwise rotating field and it drives the spin flip¹. The discussion will be divided in two cases, bosons and fermions, and rely on the use of basis change, considering the rotating frame of frequency ω . The first step is to understand the bare states obtained by removing from the Hamiltonian the off-diagonal coupling terms between field and atom. In the next step, the effect of the coupling is switched on reinserting the off-diagonal elements. Diagonalizing the resulting Hamiltonian it is possible to obtain the new eigenvalues and eigenstates, which represent the state of the atom in presence of the RF coupling.

For bosons, the B_0 field splits the ground state $J = 6$ in 13 different m_j -states, according to the Eq. (1.17). Figure 2.3 shows the resulting effect. The splitting induced by the magnetic field is linear² and hence, a RF pulse that couples two adjacent spin states unavoidably couples all the spin states. To fully understand the Hamiltonian for 13 spin states, it is useful to start from the standard textbook spin- $\frac{1}{2}$ system [Coh11]. In the laboratory frame the

¹Different configurations, as for example positioning the antenna on the z-axis, can effectively drive the transition. This is the configuration usually used in our experiment, where one exploits the presence of all the polarizations in the near field regime. In fact, only generating radio-frequencies above 300 MHz, one can reach the far field in a realistic distance antenna-atoms of 1 meter.

²As described in Chapter 1, due to the lack of nuclear spin, there is no quadratic regime accessible for magnetic field usually used in ultra-cold experiment.

Hamiltonian of the atom reads:

$$\hat{H} = \omega_0 \hat{S}_z + 2\Omega_1 \cos(\omega t) \hat{S}_x, \quad (2.3)$$

where $S_i = \frac{\hbar}{2} \sigma_i$ with $i = x, y, z$ and σ_i are the Pauli matrices defined by:

$$\sigma_x = \begin{pmatrix} 0 & 1 \\ 1 & 0 \end{pmatrix}, \quad \sigma_y = \begin{pmatrix} 0 & -i \\ i & 0 \end{pmatrix}, \quad \sigma_z = \begin{pmatrix} 1 & 0 \\ 0 & -1 \end{pmatrix}. \quad (2.4)$$

The first diagonal term in Eq. 2.3 represents the Larmor precession at frequency ω_0 induced by the B_0 field, whereas the second one is the term given by the interaction with the RF field, in which $\Omega_1 = -\gamma B_1$ is the Larmor precession frequency. According to the rotating-wave approximation³, the terms that oscillate in the opposite direction with respect to the Larmor precession of the spin are neglected. Thus, the Hamiltonian in frame rotating at ω reduces to

$$\hat{H} = \delta \hat{S}_z + \Omega_1 \hat{S}_x \quad (2.5)$$

or in the matrix form:

$$\hat{H} = \frac{\hbar}{2} \begin{pmatrix} \delta & \Omega_1 \\ \Omega_1 & -\delta \end{pmatrix}, \quad (2.6)$$

where $\delta = \omega - \omega_0$ is the detuning between the RF frequency and the Larmor frequency.

For bosonic erbium, the Hamiltonian in the laboratory frame results in:

$$\hat{H} = \mu_B g_J(\omega_0) \hat{J}_z + 2\Omega_1 \cos(\omega t) \hat{J}_x, \quad (2.7)$$

which gives, in the rotating frame of frequency ω and expressed in the basis of the eigenvectors, $|m_J\rangle$, of J_z

$$H = \frac{\hbar}{2} \begin{pmatrix} \delta_{-6} & \Omega_1 & 0 & \dots & 0 \\ \Omega_1 & \delta_{-5} & \Omega_1 & \dots & 0 \\ 0 & \Omega_1 & \delta_{-4} & \dots & 0 \\ \vdots & \vdots & \vdots & \ddots & \vdots \\ 0 & 0 & 0 & \dots & \delta_6 \end{pmatrix}, \quad (2.8)$$

where the coupling between not adjacent states is equal to zero, because of the selection rules for magnetic dipole transitions, and $\delta_{m_J} = \omega - m_J \omega_0$. Before obtaining the eigenvalues and eigenvectors of the complete Hamiltonian, it is interesting to have a look at the bare

³In this approximation, the terms in the Hamiltonian which oscillate rapidly are neglected. This is a valid approximation when the applied field is near resonance with an atomic transition. In this case the fast oscillating term is the counterpropagating one with respect to the precession of the spin.

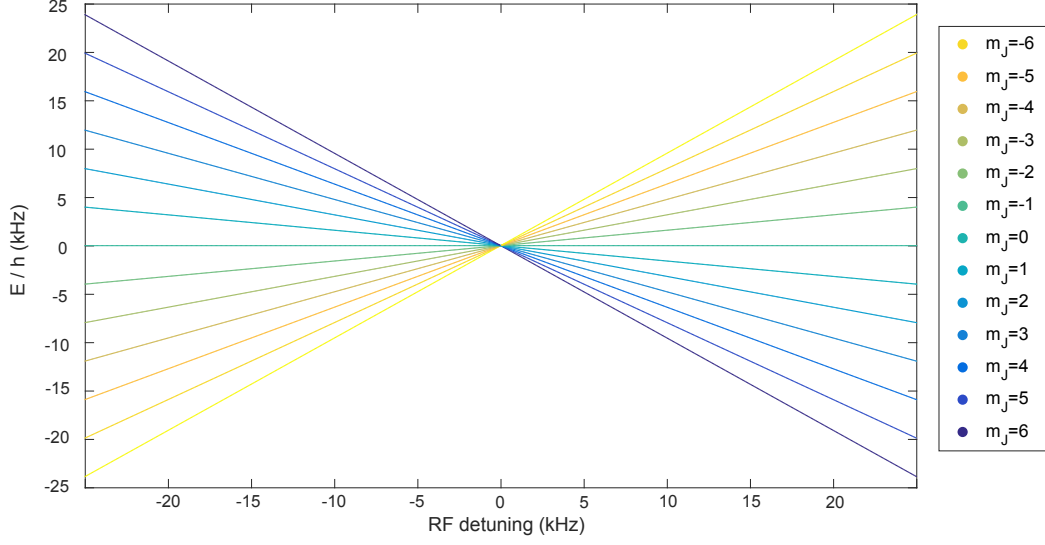
states in the rotating frame shown in Fig. 2.4a, obtained using $\Omega_1 = 0$. Switching on the atom-field coupling, as shown in Fig. 2.4b, lifts the degeneracy between the eigenstates and the crossings become avoided crossings. The new states are a mixture of all the sublevels magnetic states.

In the experiment, we apply a RF coupling at a given detuning and coupling, for a given time and detect the population of the different m_J states. After optimizing the RF pulse duration, detuning and strength we find that it is possible to achieve a population of few spin states but a deterministic and reproducible population of the latest two is not achievable. Furthermore, it is not possible to clearly see Rabi oscillations, because the high number of states makes the situation particularly complex and susceptible to noise. The applied RF starts to populate the level $m_j = -5$ and by iteration, it fills the others, up to the highest m_J . This can be seen in Fig. 2.5 where, for a thermal sample, a RF is applied for different pulse durations. For a very long pulse this leads to an occupation of all the spin states.

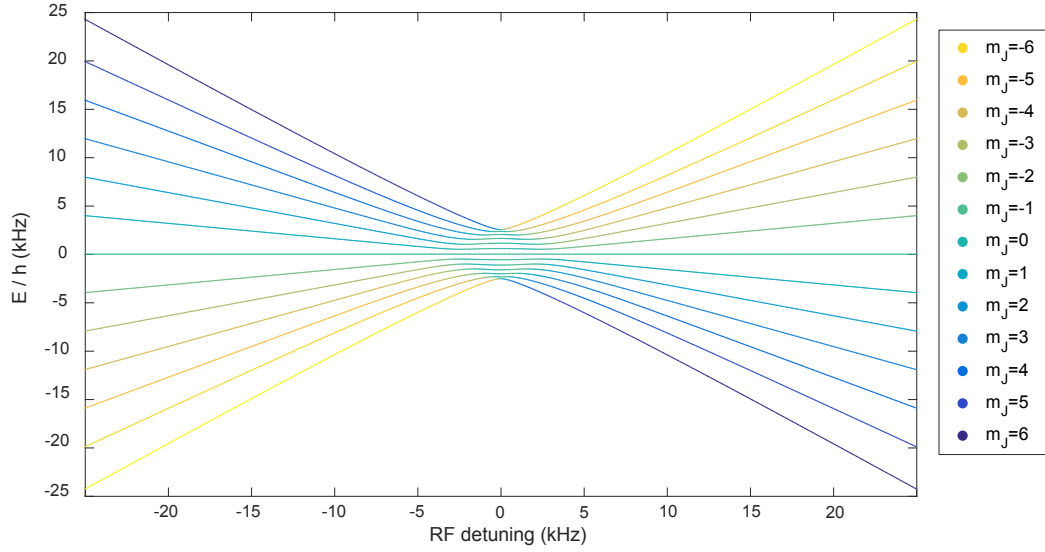
On the contrary, in the fermionic case, the preparation of a given spin state can be better controlled. It is in particular possible to achieve a deterministic population of the first two spin states in a reproducible way. This takes advantage of the fact that the nuclear spin leads to a non-negligible quadratic Zeeman shift (see section 1.2), even for magnetic fields of a few Gauss. In this case the degeneracy of all spin states for $\delta = 0$, observed in the bosonic case (Fig. 2.4a), is removed and it is possible to achieve a deterministic population of the first two spin states in a reproducible way, above few Gauss. The bare states and the coupled states, shown in Fig. 2.6, can be found after including the quadratic effect, induced by a magnetic field of 40 G, as an additional quadratic detuning on the diagonal term of the Hamiltonian. The states in presence of coupling exhibit avoided crossings at various detuning $\delta \neq 0$. In this way, when following the lowest energy state and increasing the detuning from $\delta < 0$ to $\delta > 0$, one encounters 19 avoided crossings.

Although the RF is a selective resonant phenomenon, a careful analysis is needed to understand the quadratic effect necessary to avoid to populate other states, in particular the one necessary to drive the transition to the state $m_F = -17/2$, without coupling the state $m_F = -15/2$ ⁴. Figure 2.7 a) shows an illustration of the effect of the quadratic Zeeman shift. At a given magnetic field, the Zeeman effect results in an energy splitting between the different m_F states. The linear effect leads to a dominant term, independent of the $m_F \rightarrow m_F + 1$ transitions, while the quadratic effect effectively detunes each of these different transitions by Δ_m , increasing (quadratically) with B_0 . The relevant ω for the spin state preparation would be the one resonant with the $-19/2 \rightarrow -17/2$ transition but detuned, thanks to a large enough B_0 , from the $-17/2 \rightarrow -15/2$. The necessary detuning Δ_m between the different

⁴The following consideration can be applied also for the bosonic case.



(a)



(b)

Figure 2.4: In (a) the 13 bare states (i.e. for vanishing RF coupling Ω_1) of the atom in the rotating frame, for the bosonic ground state, become degenerate when the RF is resonant with the Zeeman splitting between adjacent spin states. In (b) switching on the coupling (off diagonal terms of the Hamiltonian (2.8)), the bare states are mixed and the crossing an avoided one.

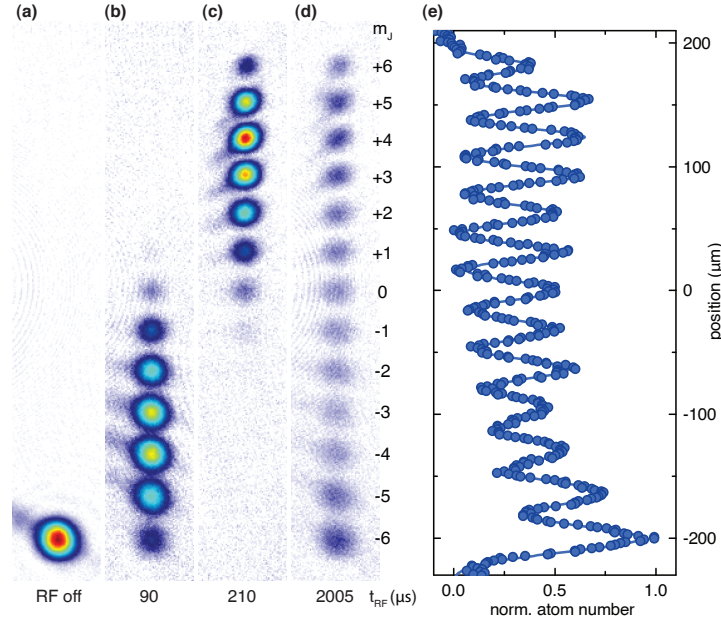


Figure 2.5: In the figure the result of applying a RF pulse for different time durations is shown in (a) (b) (c) (d) (picture taken from[Fri14]). In (e) the normalized atom number for the 2005 μs pulse is plotted versus the position. The spin position dependence is the result of the Stern Gerlach procedure.

Zeeman transition, necessary to have a robust spin preparation, usually results mostly from the magnetic noise present in the system. In particular, for our experiment, a typical noise for the B field is on the mG level. As it can be seen from the schematic illustration in Fig. 2.7 b), a magnetic field noise is directly converted in a different energy splitting of the levels mainly via the linear Zeeman effect. To quantify this effect, for 1 mG the distance between adjacent spin states varies up to 1 kHz. This not only reduces the RF coupling but also could cause a population of the higher spin states. To avoid population of the $m_F = -15/2$ the detuning δ has to be much higher than 2 kHz ($\delta \gg 2\text{ kHz}$). This condition can be verified in our experiment working at 20 G.

In addition, it is important to take care of the frequency spectrum of the RF signal. Indeed, when a very short pulse is used, the spectrum can be Fourier-limited. Particular shapes for the intensity of the RF pulse can be used to improve the Fourier spectrum, as for example the so

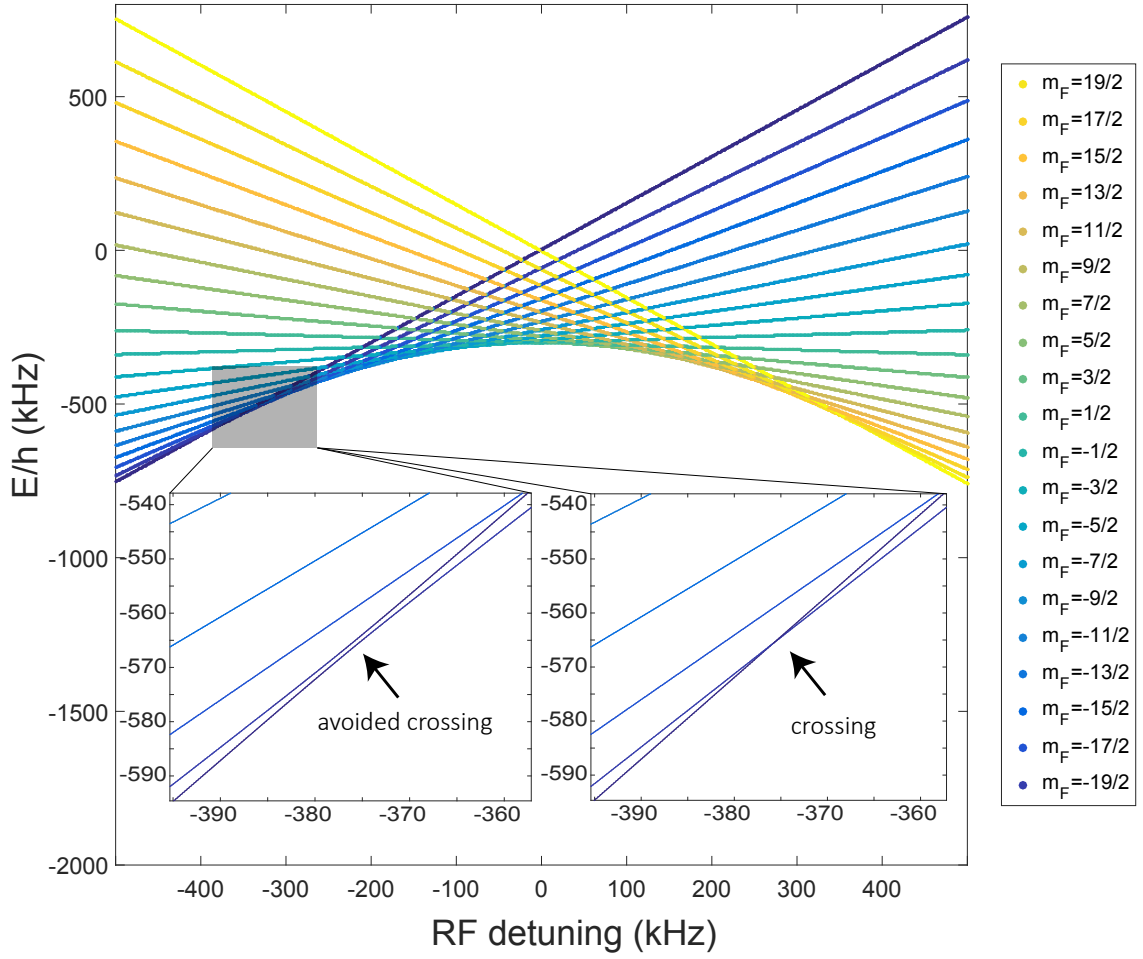


Figure 2.6: The 20 bare states of the system atom plus radiation, for the fermionic isotope in the $F=19/2$ manifold, are plotted as a function of the RF detuning. The zero indicates the $m_F=-19/2$ $m_F=-17/2$ resonance. The presence of a quadratic effect makes the adjacent states resonantly coupled at different positions of the RF frequency. The two insets show a zoom of the dashed area. In the right inset, the bare states of the two lowest magnetic sublevels cross each other in absence of RF coupling. In the left inset the bare states become dressed state and the crossing an avoided one.

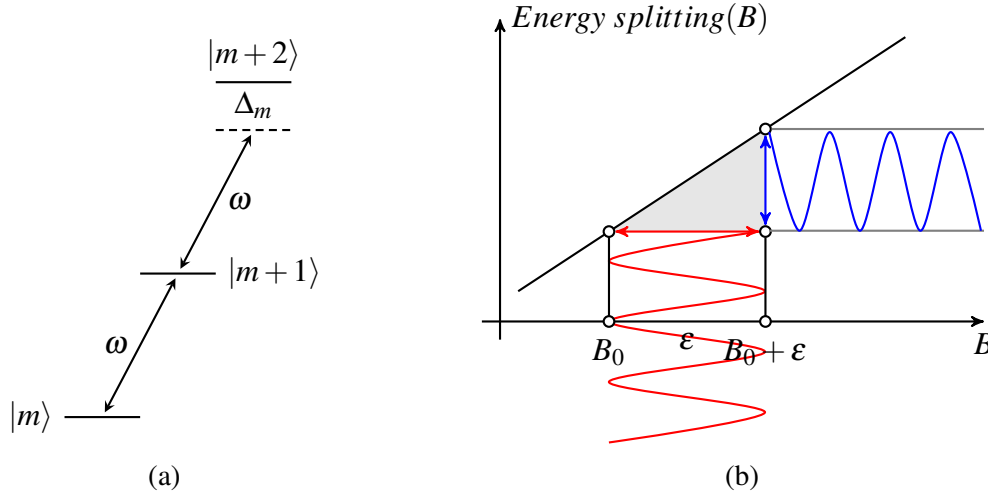


Figure 2.7: (a) When the frequency ω matches the energy difference between $|m\rangle$ and $|m+1\rangle$, the next state $|m+2\rangle$ is not coupled due to the quadratic effect, which results in an effective detuning Δ_m . (b) The magnetic field noise, depicted as a sinusoidal wave on the x-axis, leads to a variable energy splitting for adjacent spin states according to their different slope.

called Blackman pulse [Mon10; Cha13]. Figure 2.8 compares a windowing⁵ of a Blackman waveform⁶ to the standard rectangular one, in the time and in the frequency domain.

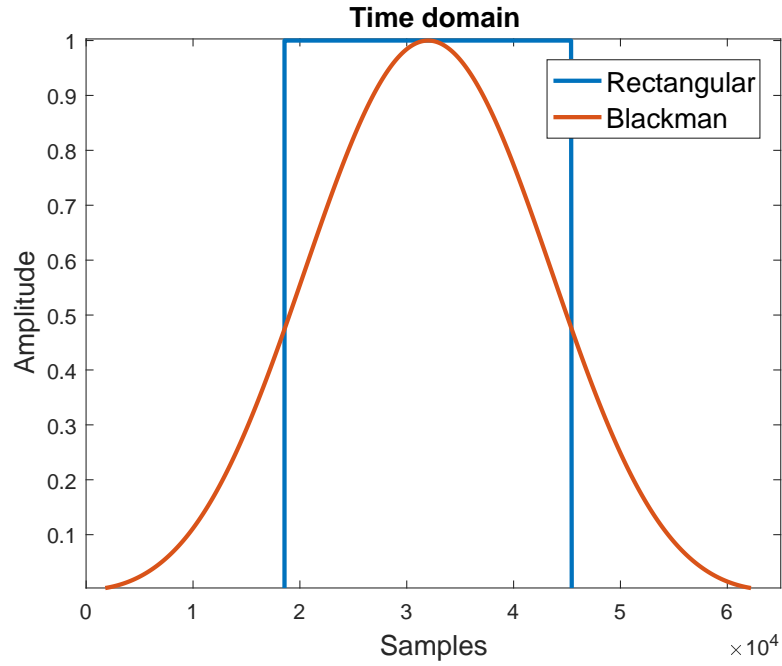
Although the main lobes' width is slightly larger in the case of Blackman pulse, the relative sidebands attenuation is much bigger and equal to -58 dB in comparison to the only -13 dB of the rectangular one. In particular, regarding the RF coupling of higher states in presence of a certain detuning δ , it could be possible to reduce the RF power, leaked at that particular detuning, using an ad-hoc choice of the function parameters.

2.2.2 Landau-Zener sweep

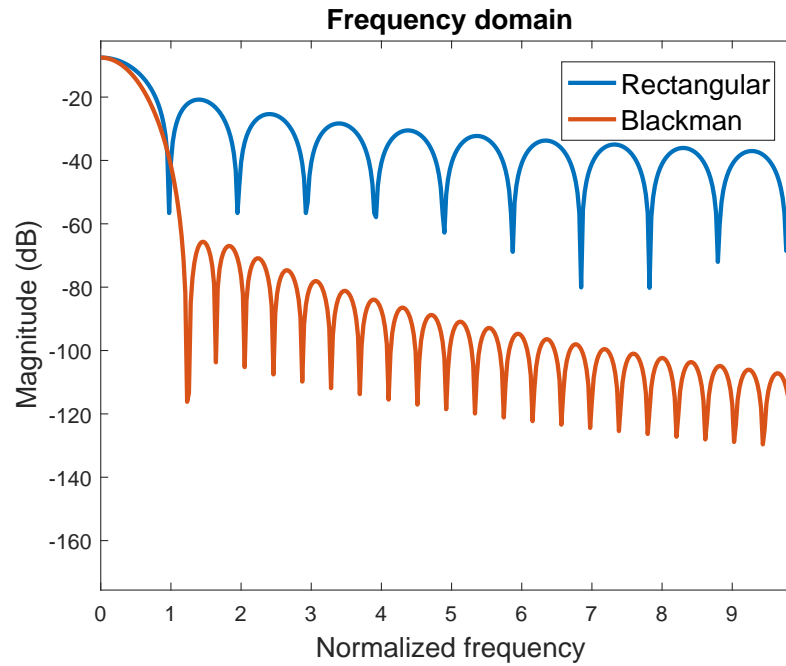
To make the spin preparation more robust with RF, the Landau-Zener passage can be executed [Mew97]. This consists in realizing a frequency sweep from the positive to negative RF detuning. The idea is to reduce the influence of the B field noise on the final state and in particular to decrease the coupling to higher spin states. Let's consider the previous case with a $S = 1/2$ system described by the Hamiltonian of Eq. (2.6). The eigenstates, obtained

⁵A window function is a function whose value is 0 outside an interval. Windowing of a simple waveform is useful since often it is interesting to look at the spectral content if a function is applied only during a limited time period. Indeed, windowing of simple waveform like $\sin \omega t$ causes its Fourier transform to develop spectral leakages at frequencies different from ω .

⁶The expression used to realize the analysis of the Blackman is $w(t) = a_0 - a_1 \cos\left(\frac{2\pi t}{N-1}\right) + a_2 \cos\left(\frac{4\pi t}{N-1}\right)$ with $a_0 = 0.42$, $a_1 = 0.5$, $a_2 = 0.08$



(a)



(b)

Figure 2.8: (a) A pulse with a rectangular amplitude in time and frequency domain is compared to the Blackman shape in (b). It is possible to notice the power leaked out at different frequency with respect to the central one can be reduced with a particular time dependence of the amplitude of the pulse.

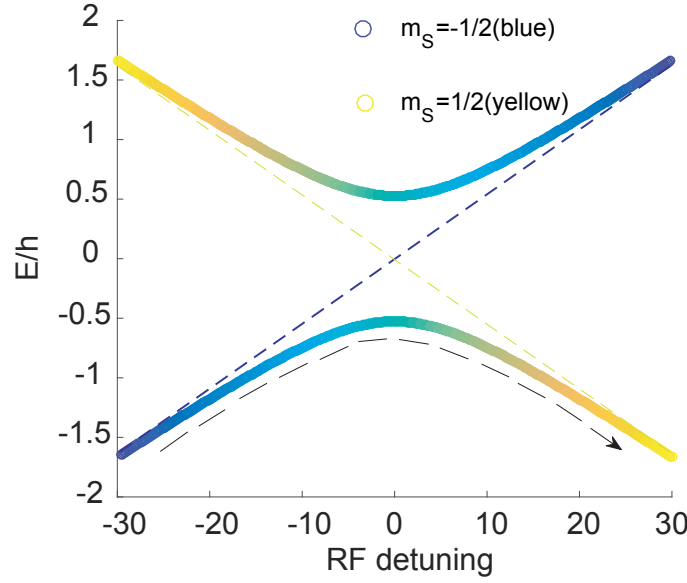


Figure 2.9: The result of the diagonalization of the Hamiltonian for a two-level system. The dressed state presents a gap. The colours gives an indication of the possibility of measure $m_S = 1/2$ in yellow or $m_S = -1/2$ in blue. Only far off resonance the dressed states match the bare states whereas they are mixed states across the resonance. As detailed in the main text, due to the presence of a gap, an adiabatic sweep of the RF frequency following the black arrow allows a passage from the $m_S = -1/2$ in to $m_S = 1/2$ state.

by diagonalizing the Hamiltonian, contain superposition of $m_S = -1/2$ and $m_S = 1/2$. Figure 2.9 shows the two m_S states, where the solid lines indicate the new states dressed by the RF, whereas the dotted lines are referred to the bare states. Far off resonance, the coupled states matches the bare states $m_S = \pm 1/2$. The method to reliably change the state of the atom, starting from $m_S = -1/2$ to $m_S = 1/2$, consists in an adiabatic rapid passage(ARP). According to the adiabatic theorem, as stated by Max Born and Vladimir Fock: "*A physical system remains in its instantaneous eigenstate if a given perturbation is acting on it slowly enough and if there is a gap between the eigenvalue and the rest of the Hamiltonian's spectrum.*"[Bor28]. Following this idea and starting with a spin polarized system in the $m_S = -1/2$, one can apply an off resonance RF and slowly ramp the detuning across the resonance. In Fig. 2.9 this corresponds to follow the dotted arrow. In this way all the atoms are transferred from the $m_S = -1/2$ to the $m_S = 1/2$ state, if the passage is adiabatic⁷.

Figure 2.6 shows the energy states in presence of RF coupling for the fermionic Er isotope. Two different types of crossing are present. One type refers to a crossing between energy

⁷To verify the adiabaticity condition we need to compare the two energy scales that are playing a role. In particular the time duration of the ramp (t) has to satisfy the relation $\frac{1}{t} \ll \frac{E_{\text{gap}}}{\hbar}$, where E_{gap} is the minimum energy splitting between the coupled states.

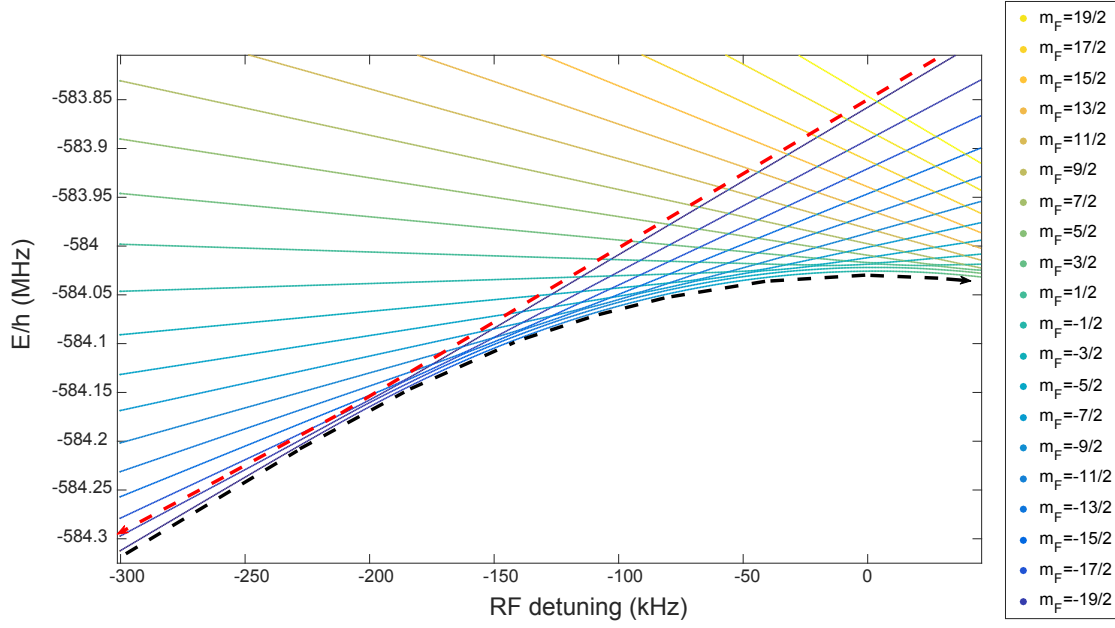


Figure 2.10: Applying the RF sweep in an adiabatic way the atoms will remain in their eigenstates. Following the black arrow, in this dressed state picture, results in obtaining a population up to the highest spin states. Instead following the red arrow leads to a population of the lowest spin states.

levels with zero-coupling, which were imposed in the Hamiltonian for all the not-adjacent spin states. The other type is instead the avoided crossing between adjacent spin states, which now results in a gap. Only adjacent spin states can be coupled by the RF, according to the magnetic dipole transition selection rules. The presence of a gap can be exploited to effectuate the adiabatic rapid passage. Starting with a spin polarized sample in $m_F = -19/2$, it is possible to effectuate the RF sweep in both directions with completely different results. Figure 2.10 displays a particular region of Fig. 2.6. The two sweep paths are highlighted with dotted arrows of different colors and allow disparate spin preparations.

Starting from an off resonance RF from negative detuning, the RF is not driving any transition up to the first zero crossing. At that point, the population of the $-19/2$ is transferred to the $-17/2$ state. Afterwards, the next crossing is the one that represents the coupling of $-17/2$ with $-15/2$. Since there is population in the $-17/2$ this will populate the higher spin state, leading to the coupling of all the spin states. Then it is possible to end up with a population in the higher $m_F = 19/2$ spin state. A complete transfer in the higher spin states is challenging since it requires to maintain the adiabaticity condition over the 19 avoided crossings present in the path. In a non-adiabatic crossing the system will not follow the ground state of the Hamiltonian and it will mix the different energy states. This path can be chosen

to achieve a population in the highest spin states, although the purity of the sample and the reproducibility will be affected.

Starting with negative detuning and following the red path, leads to a deterministic and reproducible population of the lowest spin states $m_F = -19/2$ and $m_F = -17/2$. During the sweep of the RF, the same number of crossings as before are present, but this does not influence the population of the magnetic sublevels because these are empty states. The only changes in the population is due the last avoided crossing. When this is crossed, it is possible to end up with a mixture of the only two lowest spin states.

To get the population of the different sublevels during the RF sweep, the time evolution of the wave function has to be evaluated according to the following relation:

$$|\psi(t)\rangle = e^{-i \int \frac{H_t}{\hbar} dt} |\psi(0)\rangle \quad (2.9)$$

where $\psi(0)$ is the wave function at $t = 0$, which is initialized in the lowest spin state. Figure 2.11 and 2.12 show the time evolution of the m_F state population during the two sweeps. The parameters of the sweep were chosen to optimize the spin population of the highest spin states, sweeping from positive to negative detuning, and to obtain a 50-50 mixture of the lowest two spin states, sweeping in the other direction.

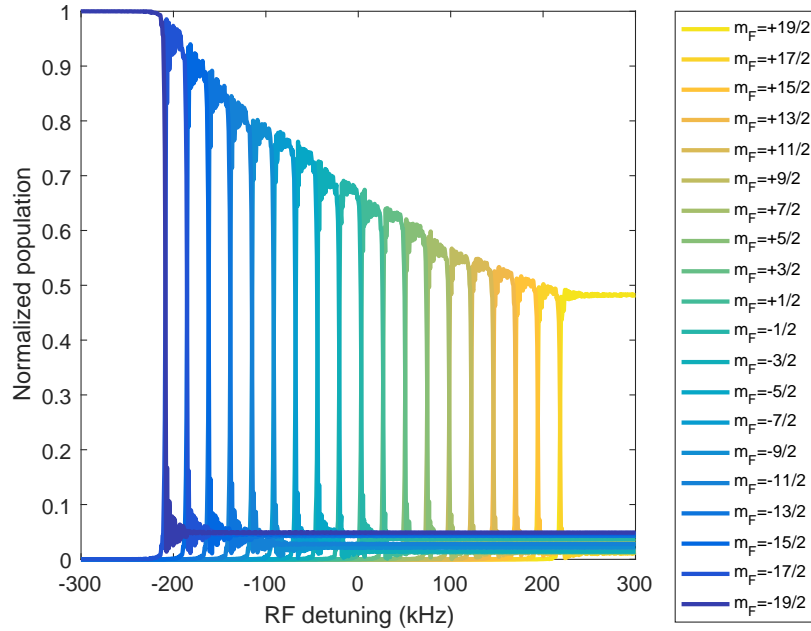


Figure 2.11: Normalized population of the spin states during the sweep as a function of the RF detuning. The not complete transfer of the population in the highest spin state is the result of a not completely adiabatic crossing of the states. This is obtained from the result of a simulation where the black arrow of Figure 2.10 is followed.

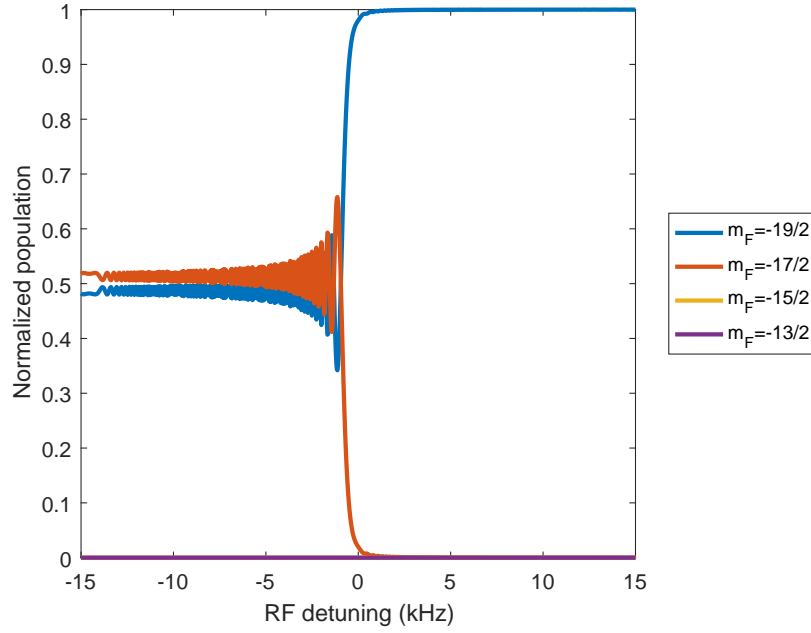


Figure 2.12: Normalized population of the spin states during the sweep as a function of the RF detuning. The not complete transfer of the population in the $m_F = 17/2$ spin state is the result of a not completely adiabatic crossing of the states. This is obtained from the result of simulation where the red arrow of Figure 2.10 is followed.

This technique is usually used in our lab to produce 50-50 mixture of fermions with better reproducibility with respect to the simple RF pulse.

It is also possible to use this technique to prepare spinor bosonic gases, but due to the lack of quadratic Zeeman effect, a pure sample is not achievable since all the levels cross at the same RF.

In Chapter 4 a promising spin preparation and a protocol for a single spin state manipulation is proposed, which can be implemented and used for fermionic and bosonic isotopes as well.

Chapter 3

Experiment on spin-1/2 system: dipolar fermions in a lattice

The previous chapter discussed a method to reduce the complexity of a spinor quantum gas of the fermionic erbium isotope from 20 to 2 spin states. The main step was to decouple the spin states and realize an effective spin-1/2 system exploiting the quadratic Zeeman effects at high B fields ($B > 20\text{G}$). In this way, the complex situation in which all the spin states are coupled can be broken down into smaller solvable problems. A spin-1/2 system in the periodic potential of an optical lattice is described by the Hubbard model. In the case of erbium, its large magnetic moment requires to modify the Hubbard model by adding the effect of the DDI; the resulting model is known as an extended Hubbard model [Dut14]. Several unexplored phases are predicted to occur with long-range interactions in the extended Hubbard model of dipolar spinor gases, e.g [Bar12; Maz17]. In the prospect of future investigations of the rich physics of dipolar spinor gases, in this chapter, we start to characterize our system with a measurement of the onsite interaction between the two lowest spin states of ^{167}Er loaded into a three-dimensional optical lattice. From the onsite measurements we can understand the interaction between the two spin states. This chapter consists of three sections. The first section introduces the basic concept of optical lattices and the lattice adopted in our experiment. The second section describes the Fermi-Hubbard model and the effects induced by the presence of DDI in the extended version. Finally, in the last section the experimental procedure adopted to investigate the onsite interaction is explained and the result analyzed.

3.1 The optical lattice: basic concepts

A one-dimensional optical lattice (1D) can be realized by simply overlapping two counter-propagating laser beams with the same wavelength λ and with a constant relative phase. This results in a standing wave whose period is $\lambda/2$. Thus, the atoms feel a periodic potential as a consequence of the effects of interference and Stark-shift. In the same way, a three-dimensional (3D) lattice geometry is obtained with the use of three pairs of counter-propagating beams, each pair being of different frequencies. Ultracold atoms in optical lattices are widely used to simulate solid state problems in which the lattice is free of impurities and atoms can be easily manipulated [Blo05]. Furthermore, this artificial crystal made of light is highly tunable. It is indeed possible to change the lattice geometry and its characteristics by modifying the laser beam parameters. For example, by changing the wavelength of one pair of counter-propagating beams, one can modify the spacing between the lattice sites in the direction of propagation of the two lattice beams. Additionally, tuning the intensity of the laser beams leads to a variation of the lattice depth, which determines the strength of the different terms of the Hubbard Hamiltonian, both the kinetic (tunneling) and the interparticle interactions. This tunability gives the possibility to carefully investigate time dynamics and phase transitions [Blo12].

In the ERBIUM experiment, two lasers running at 532nm and 1064nm create a three-dimensional(3D) optical lattice. In particular, two beams coming from the 532-nm light source and one from the 1064-nm light source are retro-reflected to obtain the 3D array of lattice sites. The 2 pairs of 532nm beams are purposely detuned by 220 MHz (so that they do not interfere). Taking the laboratory reference system, in which z is the axis of gravity and $x - y$ is referred as horizontal plane, the three lattice standing waves are orthogonal to each other and propagate along x , y and z . The resulting potential acting on the atoms can be written as

$$V_{\text{lattice}}(x, y, z) = -V_x e^{-2\frac{y^2+z^2}{w_x^2}} \sin^2(k_x x) - V_y e^{-2\frac{x^2+z^2}{w_y^2}} \sin^2(k_y y) - V_z e^{-2\frac{x^2+y^2}{w_z^2}} \sin^2(k_z z), \quad (3.1)$$

where V_η are the three amplitudes induced by the combined effect of interference and Stark shift, k_η are the wavevectors and the Gaussian envelopes (with waist w_η) result from the Gaussian profile of the laser beams. Since the atomic cloud is usually small compared with the beam waist, only the central part of the optical lattice is occupied. Thus, the trapping potential can be approximated as an harmonic confinement superimposed to an homogeneous

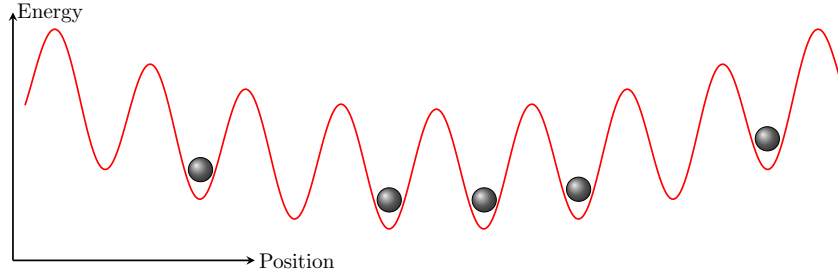


Figure 3.1: Sketch of the potential (3.2) along one direction $i=x,y$ or z resulting from the interference. The harmonic confinement is enhanced to show the effect of the Gaussian envelope confinement.

periodic lattice potential, as illustrated in Fig. 3.1:

$$V_{\text{lattice}}(x,y,z) = - \sum_{\eta=x,y,z} V_{\eta} \sin^2(k_{\eta} \eta) + \frac{m}{2} (\omega_{\eta}^2 \eta^2), \quad (3.2)$$

where the trapping frequency ω_i are given by:

$$\omega_x^2 = \frac{4}{m} \left(\frac{V_y}{w_y^2} + \frac{V_z}{w_z^2} \right) \quad (3.3)$$

and ω_y^2 , ω_z^2 can be obtained from Eq. (3.3) with cyclic permutations [Gre03]. The horizontal lattice beams produce a separation of 266 nm between the lattice sites on the x and y direction, while on the vertical direction the spacing is of 532 nm. The maximum lattice depth is given by four times the single beam trap depth and it is usually expressed in recoil energy (E_r). Due to the different wavelengths of the lattice beams in the horizontal plane with respect to the vertical direction, the recoil energies are different and equal to

$$\frac{E_r^{\text{hor}}}{\hbar} = \frac{\hbar k_{x,y}^2}{2m} = 2\pi \cdot 4221 \text{ Hz}, \quad \frac{E_r^{\text{ver}}}{\hbar} = \frac{\hbar k_z^2}{2m} = 2\pi \cdot 1055 \text{ Hz}, \quad (3.4)$$

where m is the atomic mass of the fermionic isotope. With the current setup the maximum lattice depths achievable are $(E_x, E_y, E_z) = (30, 30, 100) E_r$. We usually work at the conditions in which the two beams, propagating in the x and y direction, have the same intensity. This gives $V_x = V_y$.

3.2 Fermi-Hubbard model

The Hubbard model was first introduced to describe electrons in solids, i.e spin 1/2 fermions, and it was intensively studied to solve solid-state problems [Hub63; Ani91]. In the last years, this model was applied to ultracold atoms including new features, e.g the bosonic statistics (Bose-Hubbard model) or with the presence of a long-range interaction [Dut14], namely the DDI, which can behave as a model of the long-range Coulomb interactions which occur between electrons. To derive the Fermi-Hubbard Hamiltonian, as a starting point, one can consider the Hamiltonian resulting for a system of spin- $\frac{1}{2}$ fermions, whose interaction potential can be written as

$$V(r-r') = \left(\frac{4\pi\hbar^2 a_s}{m} \right) \delta(r-r') \equiv g\delta(r-r'). \quad (3.5)$$

This is the pseudo-potential approximation of the van der Waals potential, referred as contact interaction in Chapter 1, which features a short-range and isotropic character. Using the formalism of the second quantization, the Hamiltonian reads:

$$\hat{H} = \int dr \left[\sum_{\sigma} \hat{\Psi}_{\sigma}^{\dagger}(\mathbf{r}) \left(-\frac{\hbar^2}{2m} \nabla^2 + V_{\text{lattice}} \right) \hat{\Psi}_{\sigma}(\mathbf{r}) + g \left(\hat{\Psi}_{\downarrow}^{\dagger}(\mathbf{r}) \hat{\Psi}_{\uparrow}^{\dagger}(\mathbf{r}) \hat{\Psi}_{\uparrow}(\mathbf{r}) \hat{\Psi}_{\downarrow}(\mathbf{r}) \right) \right], \quad (3.6)$$

where σ refers to the two spins (\uparrow, \downarrow), Ψ_{σ} and Ψ_{σ}^{\dagger} are the fermionic annihilation and creation field operators, respectively, which have to satisfy the following fermionic anti-commutation relation:

$$\{\hat{\Psi}_{\sigma}(r), \hat{\Psi}_{\sigma'}^{\dagger}(r')\} = \delta_{\sigma\sigma'} \delta(r-r'). \quad (3.7)$$

In the Hamiltonian, the first term describes the kinetic and potential energy of the single particle in the lattice, whereas the second term takes into account interactions between two atoms. In this case, only the s-wave type interactions between two different spin states ($\uparrow \downarrow$) are taken into account, since the s-wave collisions vanish for identical fermions ($\uparrow \uparrow, \downarrow \downarrow$) according to the Pauli's principle and relation (3.7). The field operators can be expanded into a basis of Bloch functions ($\phi_{n,k}$). These are the eigenfunctions of the single-particle Hamiltonian where one considers only the first term of Eq. (3.6). This expansion reads:

$$\hat{\Psi}(r) = \sum_{n,k} \hat{c}_{n,k} \phi_{n,k}, \quad (3.8)$$

where $\hat{c}_{n,k}$ is the annihilation operator of the particle in the band number index n with quasi momentum k . If the degenerate Fermi gas is loaded adiabatically in a deep lattice, the

population of second and higher bands can be neglected, since the large bandgap prevents the higher bands to be populated [Pfa97]. In this case, since the Bloch functions are periodic in the momentum space, it is useful to expand them in Fourier series. Then the field operators are given by

$$\hat{\Psi}(r) = \sum_i \hat{b}_i w_i(r). \quad (3.9)$$

Here, \hat{b}_i is the annihilation operator of the particle localized at the i -th site and w_i are the associated Wannier functions defined by:

$$w_i(r) = \sum_k e^{-ik(r-r_i)} \phi_k(r). \quad (3.10)$$

Substituting Eq. (3.9) in Eq. (3.6), one finds the Fermi-Hubbard Hamiltonian:

$$H = - \underbrace{\sum_{\langle i,j \rangle, \sigma} t_{ij} b_{i,\sigma}^\dagger b_{j,\sigma}}_{\text{tunneling from site } j \text{ to } i} + U \underbrace{\sum_{i=1} b_{i\uparrow}^\dagger b_{i\downarrow}^\dagger b_{i\downarrow} b_{i\uparrow}}_{\text{on site interaction}}. \quad (3.11)$$

The first term represents the tunneling from one lattice site labeled j to one neighbor labeled i , where

$$t_{ij} = - \int d\mathbf{r} w_i^*(\mathbf{r}) \left[-\frac{\hbar^2 \nabla^2}{2m} + V(r) \right] w_j(\mathbf{r}). \quad (3.12)$$

Whereas, the second term gives the onsite interaction between two different spin states in the same lattice site, with

$$U = \frac{4\pi\hbar a_s}{m} \int d\mathbf{r} |w_i(\mathbf{r})|^4. \quad (3.13)$$

The aim of the next section is the measurement of the onsite interaction between the $m_F = -19/2$ and the $m_F = -17/2$ spin states.

As already underlined in Chapter 1 erbium has an high magnetic moment. Thus, the inter-atomic potential (3.5) has also a second contribution, which is long-range and anisotropic. The total interaction potential of Eq. (3.5) has to be modified as the sum of the contact interaction term and the dipole-dipole term

$$V(r-r') = g\delta(r-r') + \frac{\mu_0\mu_\sigma\mu_{\sigma'}}{4\pi} \frac{1-3\cos^2\theta}{|r-r'|^3}. \quad (3.14)$$

Following the same steps as before, for a system with long-range interactions expressed by the potential (3.14), one obtains the extended Fermi-Hubbard Hamiltonian. Limiting the offsite interaction terms to nearest neighbors and neglecting the terms which contain a

negligible overlap of the Wannier functions from different lattice sites, one obtains:

$$H = - \underbrace{\sum_{\langle i,j \rangle, \sigma} t_{ij} b_{i,\sigma}^\dagger b_{j,\sigma}}_{\text{tunneling from site } j \text{ to } i} + \underbrace{U' \sum_{i=1} b_{i\uparrow}^\dagger b_{i\downarrow}^\dagger b_{i\downarrow} b_{i\uparrow}}_{\text{on site interaction}} + \underbrace{\frac{V'}{2} \sum_{\langle i,j \rangle} \sum_{\sigma, \sigma'} b_{j\sigma'}^\dagger b_{i\sigma}^\dagger b_{i\sigma} b_{j\sigma'}}_{\text{near neighboring interaction}}, \quad (3.15)$$

where the new term derives from the dipole-dipole interactions between two near neighboring atoms (NNI), and it reads

$$V = \frac{\mu_0 \mu_\sigma \mu_{\sigma'}}{4\pi} \int d\mathbf{r} \int d\mathbf{r}' |w_i(\mathbf{r})|^2 \frac{1 - 3 \cos^2 \theta_{\mathbf{r}-\mathbf{r}'}}{|\mathbf{r}-\mathbf{r}'|^3} |w_j(\mathbf{r}')|^2. \quad (3.16)$$

It is worth noticing that even if the second terms is already part of the Hamiltonian in Eq. (3.11), in (3.15) $U' = U + U_{DDI}$ contains the anisotropic dependence of DDI. The term U_{DDI} strongly depends on the aspect ratio of the Wannier functions and on the dipole orientation, and it can be written as

$$U_{DDI} = \frac{\mu_0 \mu_\sigma \mu_{\sigma'}}{4\pi} \int d\mathbf{r} \int d\mathbf{r}' |w_i(\mathbf{r})|^2 \frac{1 - 3 \cos^2 \theta_{\mathbf{r}-\mathbf{r}'}}{|\mathbf{r}-\mathbf{r}'|^3} |w_i(\mathbf{r}')|^2. \quad (3.17)$$

In fact, the weight between attractive and repulsive dipole-dipole interactions in U_{DDI} relies on the shape of the Wannier function and it can become equal for a symmetric shape, resulting in $U_{DDI} = 0$. Additionally, for a non-symmetric case it can be tuned, at a fixed amplitude of the magnetic fields, rotating the dipoles. In the Hamiltonian (3.15), we neglect the terms driving flip-flop dynamics. This is a valid approximation since, for the onsite measurements presented in this thesis, we work under conditions where these processes are forbidden by the energy conservation¹.

3.3 Measurement of the interaction properties

To probe the onsite interaction between two spin states in the lattice, it is possible to measure the resonant frequency that drives the process where, starting from single occupancy of the atoms in a lattice site, one of the atom tunnels to an already occupied site. It is possible to completely neglect the possibility that two atoms in the same lowest lattice band and in the same spin state share the lattice site, due to Pauli blocking. The following subsections

¹ For the typical magnetic field values in our experiment the quadratic ac-Stark shift, induced by the lattice, (see Chapter 4) and the quadratic Zeeman effect (see Chapter 1) do not compensate each others. Hence, the energy splittings between adjacent magnetic sublevels are not degenerate thus leading to negligible flip-flop dynamics.

describe the experimental sequence usually adopted in our experiment to investigate the onsite interaction and the result of the measurements.

3.3.1 Experimental sequences

The experimental sequence starts with the realization of a degenerate Fermi gas at a typical temperature of $0.2 T/T_F$ in the ODT, where T_F is the Fermi temperature. The sample is spin polarized in the lowest magnetic sublevel $m_F = -19/2$. The atoms are adiabatically loaded into the 3D lattice using an exponential ramp to increase the power of the three retro-reflected lattice beams, afterwards the ODT is linearly ramped down in 10 ms. The final lattice beam powers result in a lattice depths of $(E_x, E_y, E_z) = (20, 20, 60) E_r$. The loading parameters are optimized to achieve population only in the lowest band of the lattice. Although several energy bands exist, the large bandgap allowed to obtain population almost only in the lowest lattice band. Thanks to the quadratic Zeeman effect several spin mixture can be achieved with a RF sweep (see Chapter 3). In this case, we work at a magnetic field of 40G and the parameters of the sweep, i.e. power, radio-frequency duration and frequency range, are optimized to obtain, in a reproducible way, a spin mixture with 75% of the atoms in the lowest spin state $m_F = -19/2$ and 25% in $m_F = -17/2$.

Figure 3.2 shows how, varying the time duration, it is possible to optimize the population of the higher spin states. The frequency range of the sweep is tuned from 75 kHz to -75 kHz with respect to the frequency resonance of the two lowest spin states, both in the experiments and in the simulations, performed along the lines of Chapter 2. The simulated results are obtained considering the time duration and frequency range of the sweep implemented in the experiment, and optimizing as only parameters the off-diagonal Rabi frequency terms of the Hamiltonian (2.8). It can be noticed that a RF sweep duration of $400 \mu\text{s}$ produces a sample of $(|-19/2\rangle, |-17/2\rangle) = (75, 25)\%$. In this set of measurement we thus use a sweep of $400 \mu\text{s}$.

After the sweep, we ramp down the magnetic field to 0.6 G, where we assume to reach a Mott insulator of unit filling per lattice site, assumption that we a-posteriori confirm at the end of this measurement. The measurement of the interspin a_s is then based on parametric heating lattice spectroscopy [Stö04; Kol06]. To resonantly create double occupancy of the lattice sites with two different spin states, the amplitude of the horizontal lattice beams are sinusoidally modulated in phase, at a frequency ν_m with a typical total amplitude of 20% for 500 ms as illustrated in Fig. 3.3. At the resonant condition $U = h\nu_m$, a maximum of doublons² are created.

²Two different spin states in the same lattice site are also referred as doublon

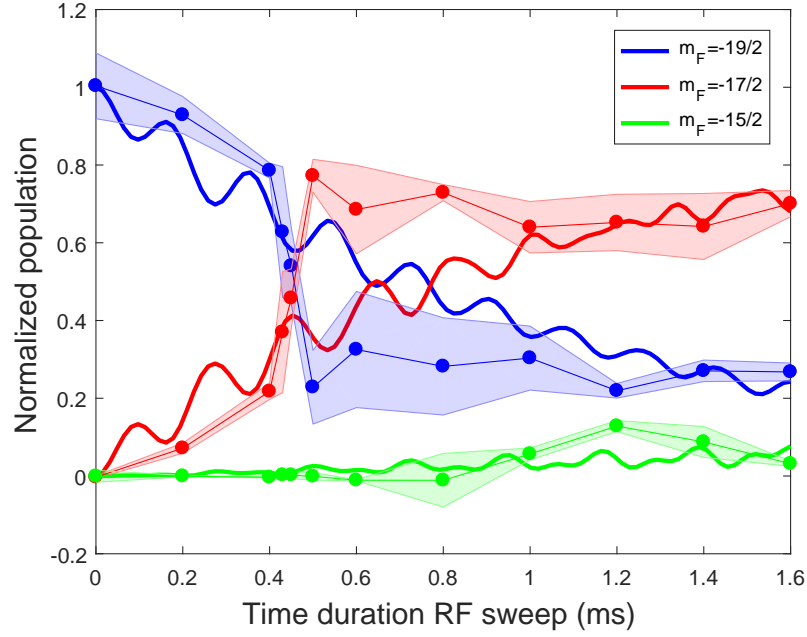


Figure 3.2: Population of the higher spin states as a function of the time duration of the RF sweep. The sweep was performed at a magnetic field of 40 G with a total RF range of 150 kHz. The shaded regions represent the experimental data, whereas the thicker lines are the simulated results.

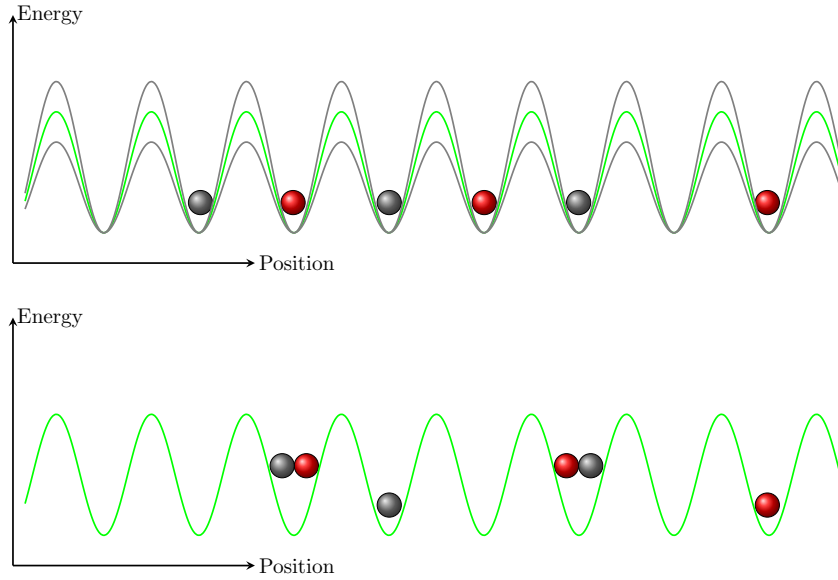


Figure 3.3: In the upper part a schematic illustration of the parametric heating. The two colors represent two different spin states. The lattice depth is changing by 20%. In the lower case, doubly occupied lattice sites are produced as an effect of the parametric heating.

3.3.2 The onsite interaction

The resolution of the imaging setup implemented in our experiment does not allow us to look directly at the doubly occupied sites; yet we can evaluate the number of doubly occupied sites from the atom losses. Indeed, there are several loss mechanisms that can shorten the lifetime of a doubly occupied site, e.g light induced two-body losses or three-body recombinations caused by the spatially overlap of the Wannier functions. The experimental sequence is repeated modulating the lattice at different frequencies ν_m . The resulting atom number is plotted as a function of the lattice modulation frequency (ν_m) in Fig. 3.4. The two colors indicate the different dipole orientations. We perform this measurement for two different polarization directions, in one case the dipoles are oriented along the z axis whereas in the other in the x - y plane, making an angle of 45° with x and y . A resonance is clearly visible in both the modulation scans indicating that, when the modulation frequency matches the energy gap given by the onsite interaction U , doubly occupied lattice sites occur and the losses are enhanced. This process is independent of the sign of the onsite energy; thus from the measurements we can only estimate the absolute value.

Indeed we observe a shift between the resonances for the different dipole orientations, which results from the anisotropic character of the DDI associated with an anisotropic Wannier function. Applying a Gaussian approximation to the Wannier function, it is possible to express the anisotropy in terms of the onsite aspect ratio (AR) as $AR = l_z/l_{x,y}$, where the $l_{x,y,z}$ are the harmonic oscillator lengths for one lattice site along the x, y and z directions. In our experiment the depths of the two green lattices are equal and as a result $l_x = l_y$. The anisotropy is guaranteed adopting a lattice with different lattice depths in the z direction with respect to the $x - y$ plane. This gives an AR of 1.5 for the lattice used. For this AR, we expect a shift of the onsite energy U' with respect to U of $U_{DDI} = -400(30)$ Hz, in the case where the dipoles are oriented along the vertical lattice beams, and of $U_{DDI} = 200(15)$ Hz, when the dipoles are oriented in the $x - y$ plane, where the errors are obtained assuming a 5% uncertainty on the lattice depths.

We can use the dipole-dipole interaction as a tool to understand the sign of the total onsite U' . Since when the dipoles are in the $x - y$ plane (red points) the curve in Fig. 3.4 is shifted to higher frequency; this means that the onsite interaction is repulsive and the sign of U' positive. The measured values³ resulting from a Gaussian fit of the resonances are

$$\text{Dipoles along } z: U' = 2.49(4) \text{ kHz} \quad (3.18)$$

³The measurements of the onsite interaction are done at a magnetic field of 0.6 G where we do not observe close by Feshbach resonances.

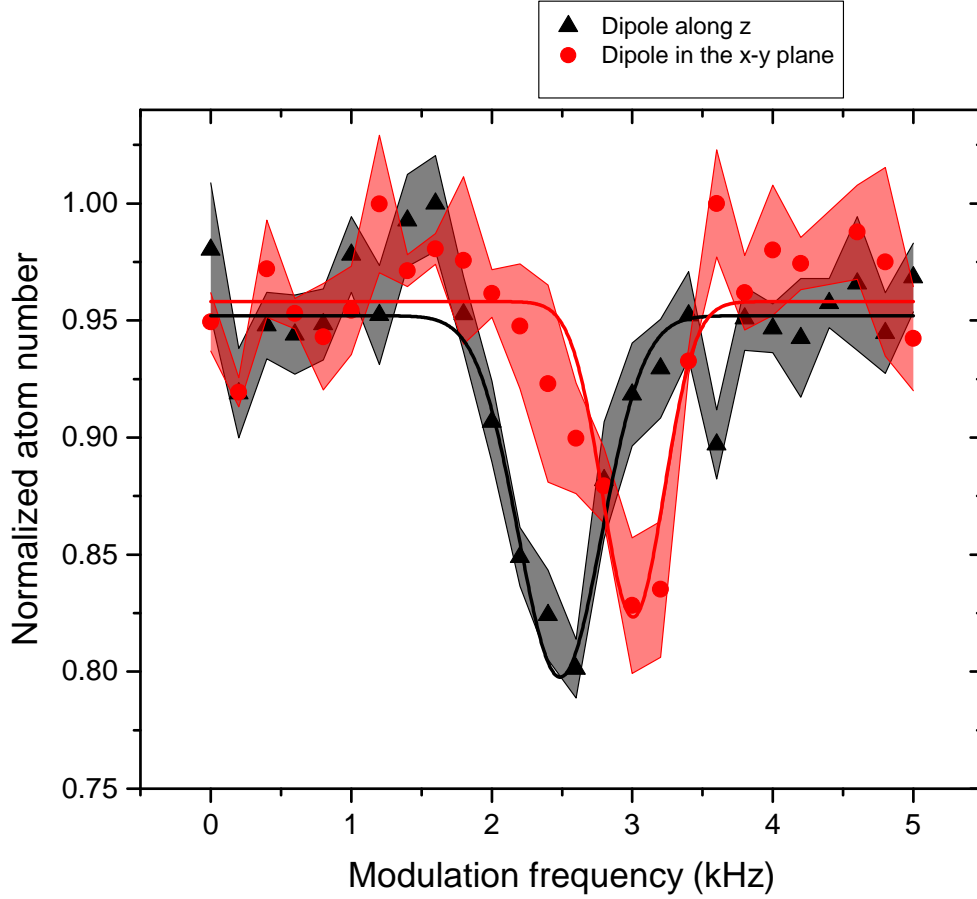


Figure 3.4: Normalized atom number as a function of the modulation frequency. When the modulation frequency matches the energy gap, given by the onsite interaction U , doubly occupied lattice sites are formed and as a result the losses are enhanced. The two colors indicate the different dipole orientations at a magnetic field amplitude of 0.6 G. The black points indicate an orientation of the dipoles along the vertical infrared lattice beam (z axis). Whereas, for the red points the dipoles are oriented in the plane of the horizontal lattice (x - y plane), at almost 45° between the two lattice beams. The clear shift of the resonant position is induced by the angle dependency of U_{DDI} .

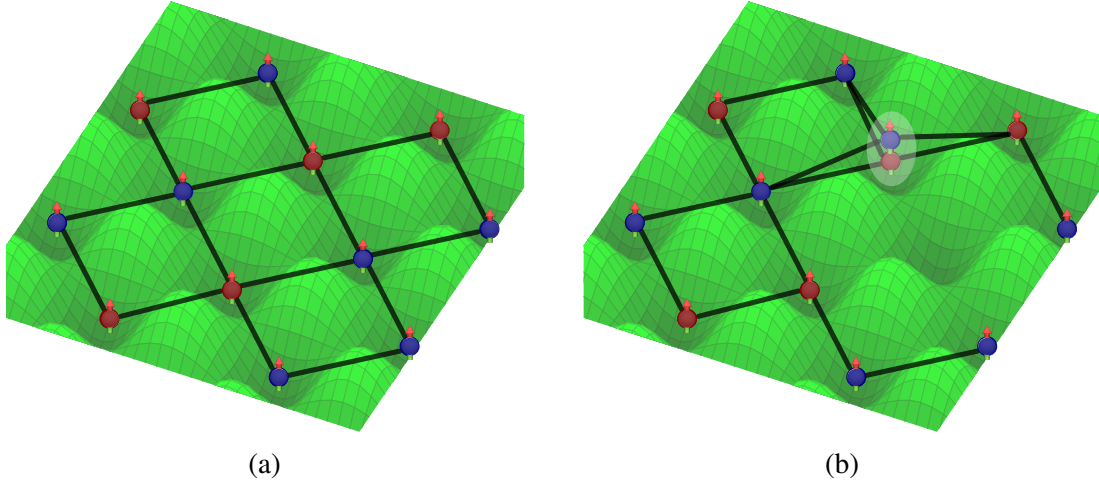


Figure 3.5: In (a) the initial configuration where all the lattice sites are occupied by one atom. The two colors represent the two spin states, whereas the arrows indicate the dipoles orientation. In (b) a double occupied site is formed as a result of the parametric heating of the green lattice beams. It is possible to notice that after the hopping process one neighbor interaction is lost.

$$\text{Dipoles in the } x - z \text{ plane: } U' = 3.00(5) \text{ kHz} \quad (3.19)$$

The measured difference is 510(90)Hz and it is consistent with the expected value of 600(45)Hz. So far, we have neglected the effect of the NNI on the predicted value of the resonance frequency. On the other hand, this is known to have a contribution [Bai12]. Since the lattice spacing in the horizontal plane is half of the spacing along the vertical direction, one can assume that the NNI interactions are non negligible only in the two-dimensional green lattice and one can see the experiment as an ensemble of 2D lattice planes decoupled from each other. The 2D lattice is illustrated in Fig. 3.5. In the production process of a doubly occupied site with two different spin states, the initial configuration has each atom sitting in a different lattice site, thus the NNI is the only energy contribution. When a doubly occupied site is reached, the two atoms in the same lattice site feel an interaction given by the onsite U , and the NNI contribution coming from the now empty lattice site is lost, i.e. one V' . Therefore, the resonant frequency (ν_m) driving the hopping is more precisely given by the following condition:

$$\hbar \nu_m = U' - V', \quad (3.20)$$

where the anisotropic character is present not only in U' but also in V' . In the 2D lattice, with 266-nm spacing, the dipole-dipole interaction assumes a side-by-side configuration which leads to a repulsive interaction, when the dipoles are oriented in the vertical direction, or

a head-to-tail configuration, when the dipoles are in the green lattice plane with an angle of 45° with respect to the two green lattice beams. The resultant corrections, according to Eq. (1.26), are of 30Hz and -15 Hz for the two cases respectively, which lie within our error bars. Finally we can evaluate the scattering length a_s for the interspin interaction between the two lowest spin states from the relation (3.13), this results:

$$a_s = 126(3)a_0 \quad (3.21)$$

where a_0 is the Bohr radius.

The strong repulsive onsite energy present in both configurations is much larger than the tunneling rate J and the thermal energy T ($U \gg J, T$). This yields a Mott insulating phase in our lattice, where each atom sits in a lattice site and the double occupancy is suppressed without the parametric heating. This means that repeating the same experiment, in which the lattice is loaded adiabatically after preparing the spin mixture, we obtain the same initial state.

Chapter 4

Advanced Spin-preparation with light

In this chapter we discuss different approaches to obtain a deterministic spin preparation with light. Almost all of them rely on the quadratic Stark shift of the magnetic sublevels induced by laser light. The chapter is divided in three sections. In the first section, we introduce the AC-Stark shift theory and the relative calculations are explained. The second section describes the realization of a laser source adopted to implement the spin preparation. Finally, the last section explains all the different implementation schemes of the laser source.

4.1 AC-Stark shift

When an atom interacts with light, the electric field \mathbf{E} induces an electric dipole moment \mathbf{P} on the atom. Furthermore, if the electric field oscillates at a frequency close with respect to an atomic transition, it induces an effective modification of the atomic levels involved in the transition, e.g. energy shift and broadening or narrowing of the spectral line. The induced shift of the atomic line can be calculated using the Stark shift theory, which will be introduced in this section. Using such a theory, we also carry out several calculations using an appropriate light wavelength. Section 4.1.2 shows the relative results.

4.1.1 Stark shift: theory

In the case of spherically symmetric atoms, such as alkali atoms, the polarizability is defined as the ratio between the induced dipole moment \mathbf{P} and the electric field \mathbf{E} , which induces the dipole moment

$$\mathbf{P} = \alpha \mathbf{E}, \quad (4.1)$$

where α is the complex scalar polarizability. It is possible to calculate from the polarizability the interaction potential energy and the scattering rates [Gri00]:

$$U_{\text{dip}}(r) = -\frac{1}{2}\langle \mathbf{p} \mathbf{E} \rangle = -\frac{1}{2\epsilon_0 c} \Re(\alpha) I(r), \quad (4.2)$$

$$\Gamma_{\text{sc}}(r) = \frac{P_{\text{abs}}}{\hbar \omega} = \frac{1}{\hbar \epsilon_0 c} \Im(\alpha) I(r). \quad (4.3)$$

The complex polarizability is usually calculated via second-order perturbation theory [Lan72] in the limit of far-detuned frequency with respect to any atomic transition. This limit requires that the detuning between the laser frequency and the atomic transition has to be much larger than the linewidth. This means that the detuning has to be also large enough to avoid that the AC-Stark shift energy scale becomes comparable with the fine structure splitting¹. Under these conditions, specifying a state with $|\beta J\rangle$ where J is the total angular momentum and β summaries all other quantum numbers, it is possible to obtain the complex polarizability after defining for all the atomic levels a complex energy $E_{|\beta' J'\rangle}$. The real part $\Re(E_{|\beta' J'\rangle})$ represents the energy difference from the ground state, whereas the imaginary part $\Im(E_{|\beta' J'\rangle})$ is related to the inverse lifetime of the excited level $\gamma_{\beta' J'}$ [Lep14]

$$E_{|\beta' J'\rangle} = E_{\beta' J'} - E_{\beta J} - i\hbar \frac{\gamma_{\beta' J'}}{2}. \quad (4.4)$$

Following [Li17; Lep14] this gives:

$$\alpha = \frac{1}{3(2J+1)} \sum_{\beta' J'} \left(\frac{|\langle \beta' J' | \mathbf{d} | \beta J \rangle|^2}{E_{|\beta' J'\rangle} - \hbar \omega} + \frac{|\langle \beta' J' | \mathbf{d} | \beta J \rangle|^2}{E_{|\beta' J'\rangle} + \hbar \omega} \right).$$

where $|\langle \beta' J' | \mathbf{d} | \beta J \rangle|$ are the reduced transition dipole moments. Assuming $E_{\beta' J'} + \hbar \omega \gg \hbar \gamma_{\beta' J'}/2$ and $E_{\beta' J'} - \hbar \omega \ll \hbar \gamma_{\beta' J'}/2$ it is then straightforward to isolate the real and imaginary part:

$$\Re[\alpha(\omega)] = \frac{2}{3(2J+1)} \sum_{\beta' J'} \frac{(E_{\beta' J'} - E_{\beta J}) \langle \beta' J' | \mathbf{d} | \beta J \rangle^2}{(E_{\beta' J'} - E_{\beta J})^2 - \hbar^2 \omega^2}, \quad (4.5)$$

$$\Im[\alpha(\omega)] = \frac{1}{3(2J+1)} \sum_{\beta' J'} \frac{(E_{\beta' J'} - E_{\beta J})^2 + \hbar^2 \omega^2}{[(E_{\beta' J'} - E_{\beta J})^2 - \hbar^2 \omega^2]^2} \hbar \gamma_{\beta' J'} \langle \beta' J' | \mathbf{d} | \beta J \rangle^2. \quad (4.6)$$

In contrast, the response of non-spherically symmetric atoms, such as erbium, to an electromagnetic field is more complex. The reasons for this are essentially two and both related to

¹For fermions hyperfine splitting.

the electronic configuration. First, lanthanides, as already underlined in the Chapter 1, have a complex energy spectrum which has to be taken into account with a sum over states formula over all the dipole allowed transitions. Second, Er atoms can be seen as an anisotropic medium, where the asymmetry comes from the highly anisotropic electronic wavefunction of the 4f-electrons. Due to these reasons, the polarizability in these cases is a tensor:

$$\alpha = \begin{bmatrix} \alpha_{xx} & \alpha_{xy} & \alpha_{xz} \\ \alpha_{yx} & \alpha_{yy} & \alpha_{yz} \\ \alpha_{zx} & \alpha_{zy} & \alpha_{zz} \end{bmatrix}$$

The result is a polarization and a magnetic-sublevel dependent polarizability. For convenience the polarizability tensor matrix is usually decomposed in three parts: α_{scal} represents the diagonal elements and hence describes the response in the same direction of the applied field, α_{vect} represents the anti-symmetric part of the off-diagonal elements and together with the symmetric part of the off-diagonal elements α_{tens} , describes the response in different directions with respect to the applied field. The interaction potential energy equals [Vex11]:

$$U_{m_J}^{\text{ell}}(\mathbf{r}; \theta_p, \theta_k, \mathbf{A}; \omega) = -\frac{1}{2\epsilon_0 c} I(\mathbf{r}) \left\{ \Re[\alpha_{\text{scal}}(\omega)] + \mathbf{A} \cos \theta_k \frac{M_J}{2J} \Re[\alpha_{\text{vect}}(\omega)] + \right. \\ \left. + \frac{3M_J^2 - J(J+1)}{J(2J+1)} \times \frac{3 \cos^2 \theta_p - 1}{2} \Re[\alpha_{\text{tens}}(\omega)] \right\}, \quad (4.7)$$

where $\mathbf{A} = \mathbf{u} \times \mathbf{u}^*$, \mathbf{u} is the polarization vector, m_J are the magnetic sublevels, θ_k is the angle between the direction of propagation of the light beam with the quantization axis, defined by the direction of the magnetic field for dipolar atoms, and θ_p is the angle between the polarization vector and the quantization axis. The angles are displayed in Fig. 4.1, where the magnetic field is oriented in the z direction. The decomposition of the polarizability tensor is given by:

$$\alpha_{\text{scal}}(\omega) = \frac{2\omega_{JJ'} |\langle J || \mathbf{d} || J' \rangle|^2}{3\hbar(2J+1)(\omega_{JJ'}^2 - \omega^2)}, \quad (4.8)$$

$$\alpha_{\text{vect}}(\omega) = (-1)^{J+J'+1} \sqrt{\frac{6J}{(J+1)(2J+1)}} \begin{Bmatrix} 1 & 1 & 1 \\ J & J & J' \end{Bmatrix} \frac{\omega_{JJ'} |\langle J || \mathbf{d} || J' \rangle|^2}{\hbar(\omega_{JJ'}^2 - \omega^2)}, \quad (4.9)$$

$$\alpha_{\text{tens}}(\omega) = (-1)^{J+J'} \sqrt{\frac{40J(2J-1)}{3(J+1)(2J+1)(2J+3)}} \begin{Bmatrix} 1 & 1 & 2 \\ J & J & J' \end{Bmatrix} \frac{\omega_{JJ'} |\langle J || \mathbf{d} || J' \rangle|^2}{\hbar(\omega_{JJ'}^2 - \omega^2)}, \quad (4.10)$$

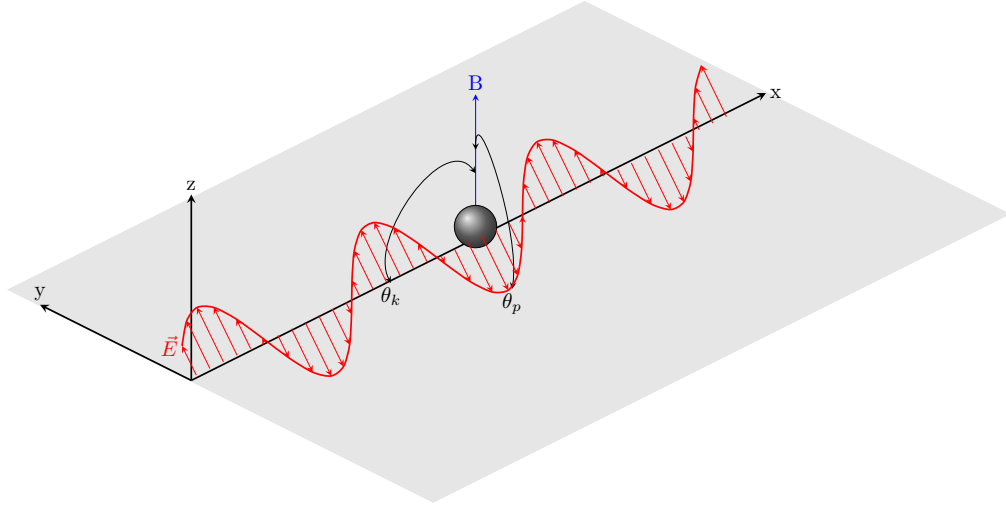


Figure 4.1: Representation of the angle notation used to define the polarizability. The B field is along z and defines the quantization axis. The light is linearly polarized and it propagates along x . θ_k is the angle between the direction of propagation of the light and the quantization axis, whereas θ_p is the angle between the polarization vector and the quantization axis.

where the curly brackets are used to indicate the Wigner 6J-symbols.

The result of Eq. 4.7 points out that the anisotropy of the polarizability in erbium atoms can disappear for a proper choice of the angle. In particular the vectorial part is always zero for linear polarization (since \mathbf{u} is a real vector and hence $A = 0$) and the tensorial one choosing the angle $\theta_p = 54.7^\circ$. This definition is also consistent with alkali atoms where no quadratic magnetic sublevel and polarization dependency is found since $J=1/2$ makes the tensorial contribution always zero.

The photon-scattering rate is even more strongly anisotropic [Lep14]. It can be calculated from

$$\begin{aligned} \Gamma_{m_J}(\mathbf{r}; \theta_p, \theta_k, \mathbf{A}; \omega) = & -\frac{1}{2\epsilon_0 c} I(\mathbf{r}) \left\{ \Im[\alpha_{\text{scal}}(\omega)] + \mathbf{A} \cos \theta_k \frac{m_J}{2J} \Im[\alpha_{\text{vect}}(\omega)] + \right. \\ & \left. + \frac{3m_J^2 - J(J+1)}{J(2J+1)} \times \frac{3 \cos^2 \theta_p - 1}{2} \Im[\alpha_{\text{tens}}(\omega)] \right\}. \end{aligned} \quad (4.11)$$

To obtain a spin preparation exploiting light, different methods can be implemented. As already underlined in Chapter 2, the main difficulties to obtain a reproducible spin preparation with the use of RF in erbium is due to the presence of a high number of states which become all coupled together, for bosons. This problem can be overcome with fermions preparing the spin at field larger than 20 G through the quadratic Zeeman effect. Also preparing the spin states with other methods as a Landau-Zener sweep or using excitation via excited states,

Table 4.1: Summary of the characteristics of the chosen transition. It is worth noticing that the g_J value of the excited state is different with respect to the one of the ground state.

Wavelength (nm)	Linewidth (kHz)	g_J value	Γ (s^{-1})
631.04	11.6	1.07	8.587×10^4

as for Raman scheme or Stimulated Raman Adiabatic Passage (STIRAP) will not provide a pure preparation if particular care is not taken in the choice of the used wavelength. In fact, the main idea for a light scheme relies on the possibility of removing the degeneracy induced by the coupling between the different spin states. This is feasible due to the quadratic dependence of the magnetic sublevels of the tensorial term that is present in the AC-Stark shift of Eq. (4.7). Hence, it is crucial to choose a wavelength for which the tensorial part is suitable to obtain enough detuning when the coupling is switched on. In addition, it is necessary that the scattering rate is sufficiently low to avoid heating of the system. For these reasons and for others that will be clear following the discussion, the transition at 631 nm of erbium was the one finally chosen. The main characteristics of the chosen transition are listed in Table 4.1.

4.1.2 Ac-Stark shift: calculation at 631 nm

To compute the total Ac-Stark shift we use the formalism of the previous section 4.1.1. The following calculations are realized for the bosonic isotopes but similar result are obtained also for the fermionic one. Using a sum over Eq. (4.7) for the 1284 lines, all the known dipole-allowed transitions of erbium were considered. In addition, when possible, the theoretical matrix elements were replaced with experimentally measured values as for the 631-nm transition [Ban05]. Figure 4.2 shows the calculated total energy shift for different light polarizations as a function of the detuning from the transition. For simplicity, in the figure we show only the four lowest spin states. Below each plot a schematic diagram of the shift is shown for a fixed positive detuning. Among the three light polarizations, the σ^- gives the largest AC-Stark shift. On the other hand, for a deterministic spin preparation we are interested in the differential light shift between adjacent spin states. Thus, for the three light polarizations, we need to compare the difference between two adjacent spin states $\Delta E_{m_J} - \Delta E_{m_J+1}$ with the following two $\Delta E_{m_J+1} - \Delta E_{m_J+2}$. Figure 4.3 shows the resulting differential light shift as a function of the light detuning. Finally, the quadratic effect on the different magnetic sublevels, coming from the tensorial term, is directly visible. Table 4.2 summarizes the results for a fixed detuning of 2 GHz. In particular, it is possible to notice

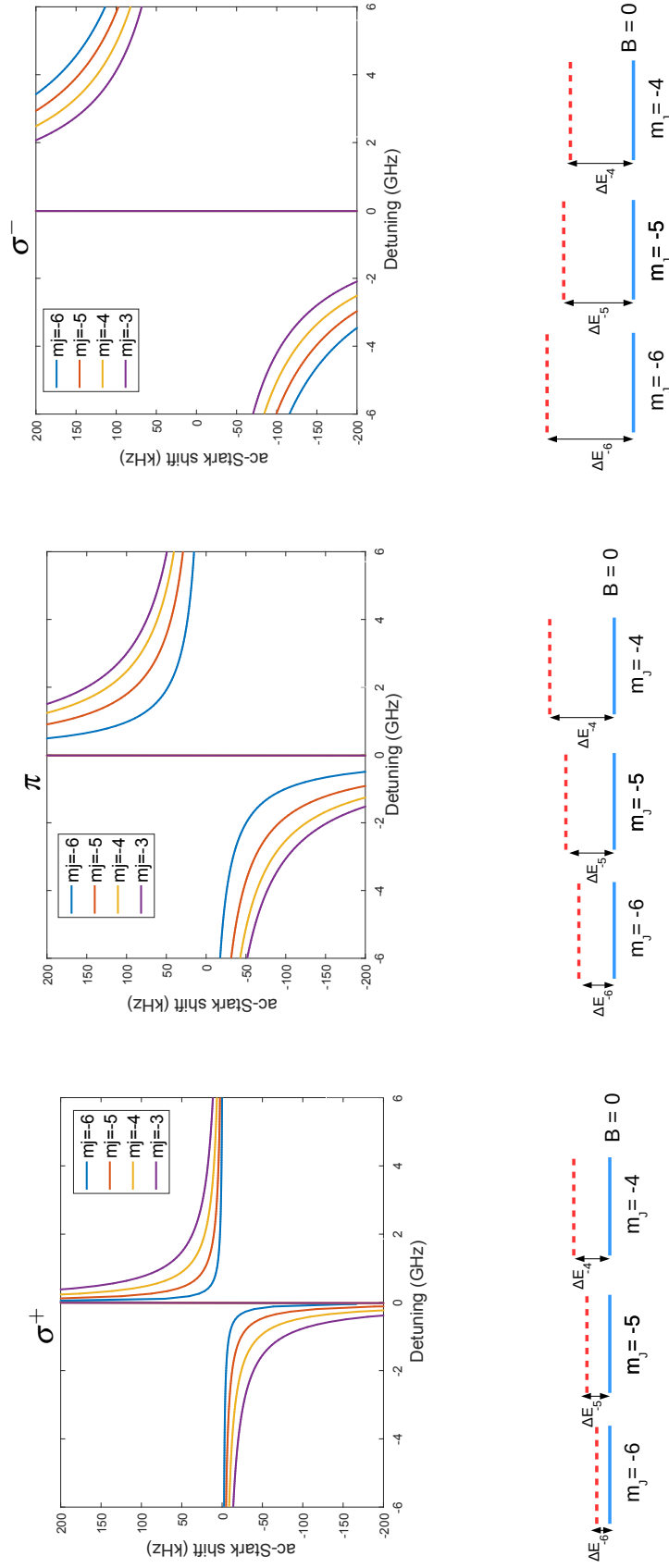


Figure 4.2: Total light shift for σ^+ , π , and σ^- polarization as a function of the detuning for an interval of 12 GHz around the resonance. For this calculations the intensity is set to 1 W/mm^2 and only the first four magnetic sublevels are plotted. Below each plot is a schematic diagram of the shift of the levels of the shift of the levels is depicted in red. Without the light at a magnetic field $B = 0$ all the states (blue) are degenerate.

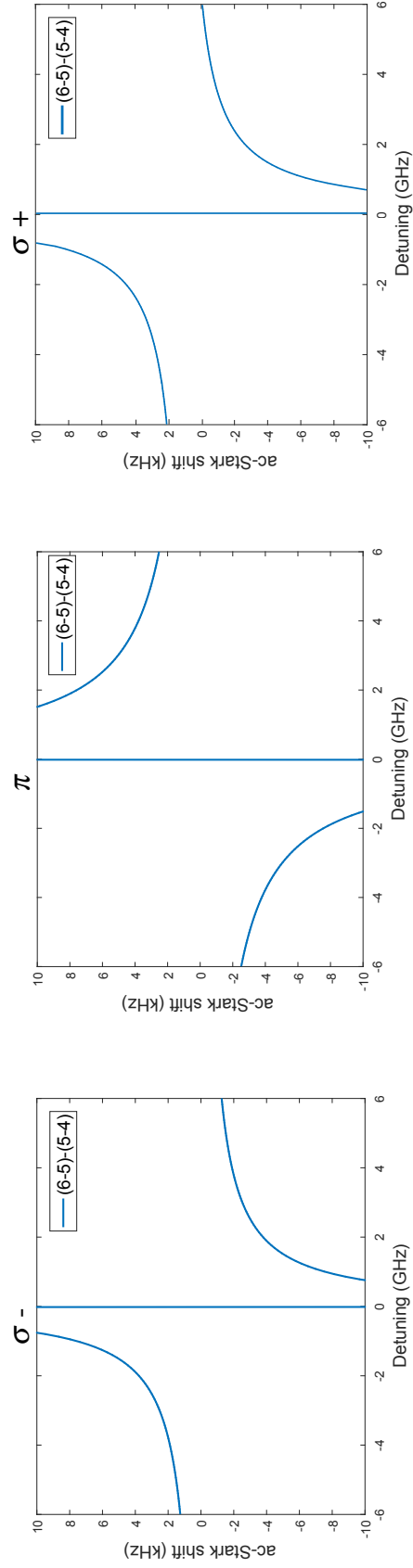


Figure 4.3: Differential shift $\Delta E_{m_J=-6} - \Delta E_{m_J=-5} - \Delta E_{m_J=-4}$ obtained with an intensity $I = 1 \text{ W/mm}^2$ is plotted versus the detuning. It is worth to notice the similar behavior with respect to the total AC-stark shift of Fig. 4.2. The quadratic effect is directly visible. The π polarized light is the one in which the biggest quadratic effect is obtained.

that the quadratic effect is not constant over the detuning range analyzed, but assumes almost the same shape of the total shift. Considering Eq. (4.8) and Eq. (4.9), the ratio between the tensorial term and the scalar one, for this transition, is almost constant and equal to $\alpha_{\text{tens}}/\alpha_{\text{scalar}} = 0.3$. To notice, this ratio results particularly big in this narrow linewidth transition. For dysprosium a ratio of the same order was also experimentally confirmed for the same type of transition at 741 nm [Kao17].

Table 4.2: Summary of the differential AC–Stark shift for different polarizations. The π polarized light gives the absolute bigger value. The data were calculating at a detuning of 2 GHz from the resonance, with an intensity $I = 1 \text{ W/mm}^2$.

$\delta = 2 \text{ GHz}; I = 1 \text{ W/mm}^2$	σ^+	π	σ^-
Differential AC–Stark shift(kHz)	-4	7	-4

Even if larger quadratic effects can be achieved from the simulation going towards the resonance, one should always take care of two different effects. First, the calculations are only valid in far-detuned condition $\delta \gg \Gamma$, which for the 631-nm light requires $\delta \gg 116 \text{ kHz}$. Second, the AC-Stark shift is only half of the story, it is important to look at the scattering rates to avoid that an excessive scattering overheat the system out of the degeneracy condition. Figure 4.4 shows the scattering rates, obtained with an intensity of 1 W/mm^2 from the sum of all the known states of Eq. (4.11), as a function of the detuning and for different polarizations. It is possible to notice the different scaling with respect to the AC-Stark shift. The potential and the AC-Stark shift scales as I/Δ , whereas the scattering rates as I/Δ^2 . Therefore, increasing the intensity and the detuning will lead to the desired shift with lower scattering and hence, lower heating.

Beside the beneficial narrow-linewidth character of the 631-nm atomic line, the g_J factor of the excited state is 7% smaller with respect to the one of the ground state. This, according to Eq. (1.17), results in a different slope of the magnetic sublevels of this excited state with respect to those of the ground state, allowing several possibilities for the spin preparation, as explained in section 4.3.

4.2 Realization of a laser source at 631 nm

As described above, the 631-nm line has different advantages from the atomic prospective. Not so lucky is instead the commercial side. The solutions available are usually expensive or have low output power. The main reason is that finding a diode lasing at this wavelength is not straightforward and often very extreme temperatures are required to reach the desired wavelength. For this reason, and in addition due to the fact that we luckily found a diode

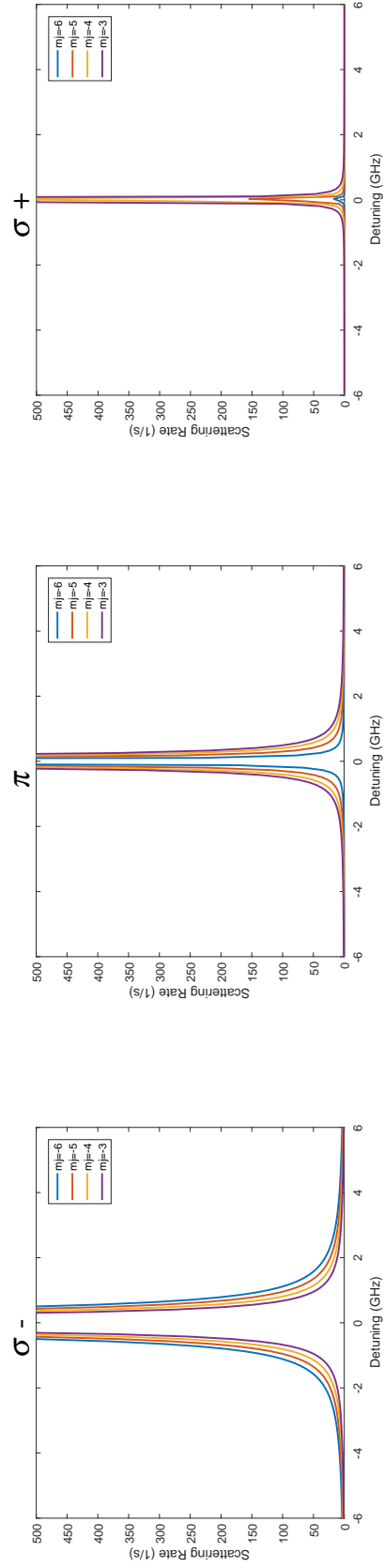


Figure 4.4: The scattering rates obtained from the calculation using an intensity of 1 W/mm^2 is plotted as a function of the detuning for an interval of 12 GHz around the resonance. From the left to the right the result for different polarizations $\sigma^- \pi \sigma^+$ is shown. It is possible to notice that the photon-scattering rates is strongly dependent on the polarization and that the use of σ^+ light induces less heating.

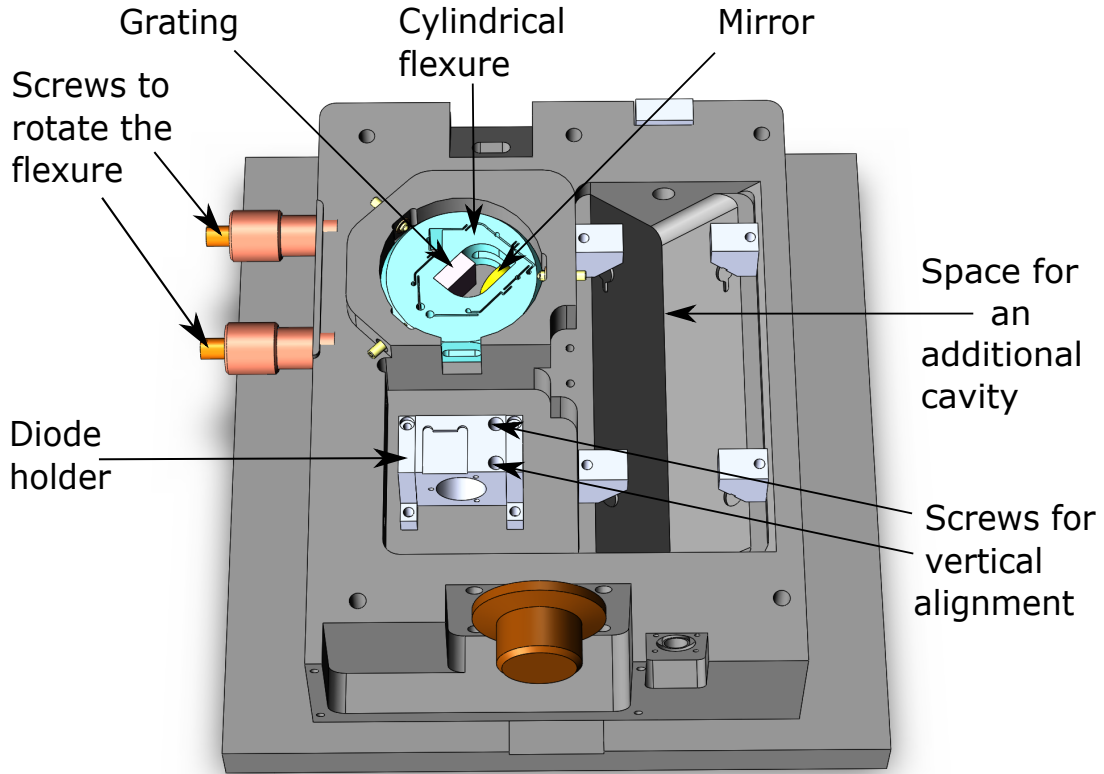


Figure 4.5: The laser design used for realizing the source emitting at 631 nm. Four peltier elements on the basement are used to thermally stabilize the whole body. An additional peltier is used to stabilize the temperature of the diode housing. This is a Littrow enhanced configuration. The rotating cylindrical part depicted in blue allows a simultaneous rotation of the grating and of the mirror. The resulting output beam has a fixed direction parallel to the one coming from the diode. Design from [Kir15]

lasing at the right wavelength, we decided to realize the laser source. In this section the experimental setup and the development of the laser source are discussed. First, the chosen design is briefly discussed. Second, the diode laser is presented and characterized. Finally, the optical setup used in the experiment is shown and explained in detail.

4.2.1 Design of the laser system

Diode lasers are generally compact light sources that, using as external cavity with optical retroreflection, can easily achieve linewidths in the range of 200 kHz [Rie04]. The design used in this thesis is a compact, robust Littrow-type external cavity diode laser (ECDL), already tested and discussed in [Kir15]. Here we briefly summarize the characteristics. The design is illustrated in Fig. 4.5. It is often referred as enhanced Littrow configuration.

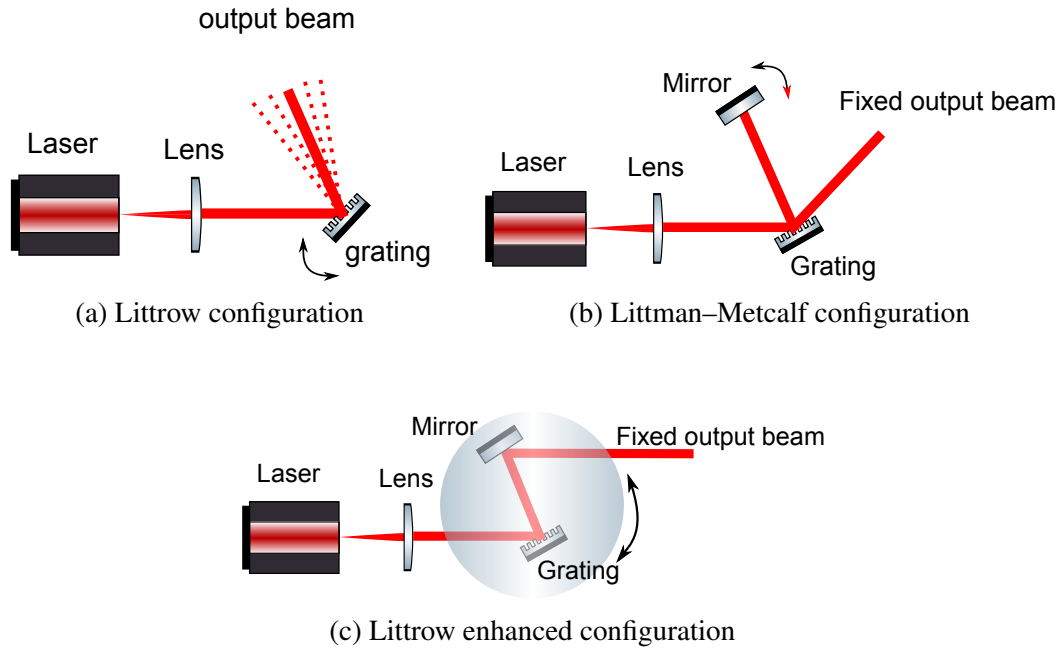


Figure 4.6: Tunable external-cavity diode lasers in (a) Littrow, (b) Littman–Metcalf and (c) Littrow enhanced configuration. In the Littrow configuration the selection of the wavelength is obtained rotating the grating. This rotation causes a variation in the direction of the beam. In the Littman–Metcalf configuration a fixed output beam is obtained using an additional mirror that is rotated to select the wavelength. The fixed output beam is obtained from the second order diffracted beam from the grating. In the Littrow enhanced configuration, the grating and mirror, parallel to each others, are rotated simultaneously. The resulting fixed beam is parallel to the beam coming from the laser and is due the 0 order of the grating.

In a standard Littrow, a grating is used as wavelength-selective optical element to tune the light wavelength, retroreflecting a portion of the laser beam into the diode chip itself. The configuration, which includes diode, lens and grating, as standard Littrow, has the main disadvantage that the beam direction changes when the grating is rotated. Having a fixed direction of the output beam is often convenient for many applications. For this reason, other configurations were developed as the Littman-Metcalf or the Littrow enhanced. For comparison the three configurations are illustrated in Fig. 4.6. In the Littman-Metcalf configuration the first order beam from the grating is not directly retro-reflected on the diode chip but it is reflected on an additional mirror. This mirror reflects the beam again on the grating and finally back to the chip. By rotating the mirror it is possible to tune the wavelength. The second order of the grating is a fixed beam that can be used for the optical setup. This configuration tends also to offer a smaller linewidth due to the double use of the grating. The main drawback is that the zero-order reflection of the beam is lost, resulting in a lower power output compared to the simple Littrow. Finally, the Littrow-enhanced

configuration allows to obtain an almost fixed beam with the same power of the simple Littrow configuration, combining the main advantages of the other two configurations. This is realized with the simultaneous rotation of the grating and of an additional mirror. The latter is usually positioned parallel to the grating to additionally obtain a beam traveling parallel to the original one coming from the diode. In this configuration, when the system grating plus mirror is rotated, the beam is slightly laterally displaced on the mirror by a quantity $\Delta_x \simeq 2L\Delta_\theta$, where L is the distance between mirror and grating and Δ_θ is the grating angle. For a tuning range of 1 GHz, typical for tuning through an atomic resonance of different isotopes in Er, the displacement is on the order of 100 nm for $L \simeq 1$ cm. This is negligible for our experimental uses, in which the light will be fiber coupled before aligned on the atoms. The whole body of the laser is made of aluminum and thermally stabilized by 4 peltiers wired in series. Passive stability and acoustic immunity were obtained using a CAD program where elastic properties could be simulated.

4.2.2 Diode laser characterization

The diode chip² is supplied with an home-made low noise current driver and it is mounted in a commercial collimation package provide by Thorlabs (LT230P-A). The collimation package is covered by a thin copper foil and inserted in an alluminum diode holder isolated from the whole body by a plastic insert. One side of a peltier element is glued with high thermo-conductive glue on the top of the diode holder and the other side of the peltier is glued to a copper wire which is connected to the main body. The overall system, copper wire plus main body, serves as a heatsink for the peltier. Two temperature-sensing elements³ are used to thermally stabilize with an home-made proportional-integral (PI) control loop feedback. A PI continuously calculates an error signal as the difference between a set value and a measured one and applies a correction proportional to the difference and takes into account the previous value with the integrative part. The integrative part is not necessarily zero when the error signal is zero. This makes it possible to maintain the error signal zero even when the action of the proportional part would be zero. In this way, the current flowing on the peltier is instantaneously chosen from the PI to make the error signal zero and to maintain this value over time.

Once the temperature is correctly stabilized, we characterize the diode laser. Figure 4.7 displays the output power as a function of the injection current for the free running diode at a

²HL63163DG is an AlGaInP from USHIO with a maximum optical output power of 100 mW.

³The two elements are made of semiconductor that displays large increase of resistance in proportion to small diminution in temperature. For this reason are usually referred as Negative Temperature coefficient (NTC).

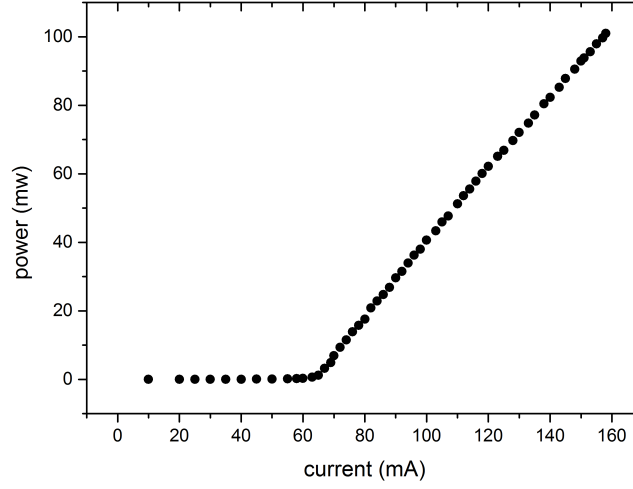


Figure 4.7: Power output versus injection current of the diode. The measurements set is obtained at a temperature of 20°C.

fixed temperature. The threshold current is at 60 mA and the laser provides maximum power of 100 mW at 158 mA. For a fixed current (80 mA), the power of the emitted light decreases when the temperature of the diode is increased⁴, see Fig. 4.8.

To measure the wavelength, we coupled the light into a fiber, which it is then connected to a commercial wavemeter from the company *High Finesse*. To investigate the wavelength tunability, the temperature of the diode holder was stabilized to different values. Figure 4.9 reports the induced variation of the wavelength. Changing the temperature of the diode tunes the frequency of the laser for two main reasons. First, the gain curve depends on the wavelength. Second, the optical path length of the internal cavity of the diode changes with the temperature. The three jumps in the plot indicate hopping from one longitudinal mode to the next mode ($\simeq 0.4$ nm) induced by a shift of the gain curve. The erbium line at 631.04 nm can be obtained also in free running at a temperature of 24.8°C.

For a fixed temperature, we also investigate the current dependence of the wavelength, since the current affects again the temperature of the diode and the carrier density (causing a small change in the index of refraction of the material). This is shown in Fig. 4.10. It is worth noticing that the resulting tuning curve looks almost equal with respect to the previous one. The main effect is induced by the temperature variations.

After characterizing the free running laser, we aligned the retroreflection from the grating of the Littrow configuration. To obtain a good alignment the current of diode was set near

⁴This effect is induced by the increase of not radiative process, i.e. thermal electron-hole recombination.

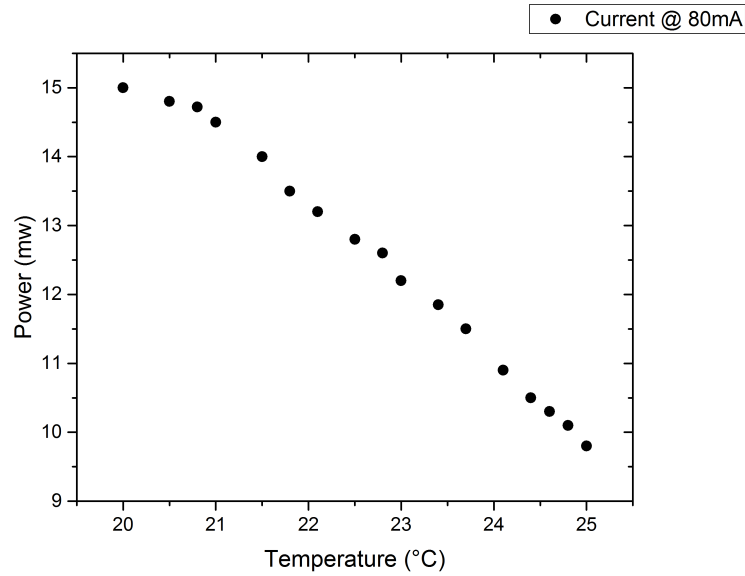


Figure 4.8: Power output versus temperature of the diode. The measurement set is obtained at a fixed current of 20 mA.

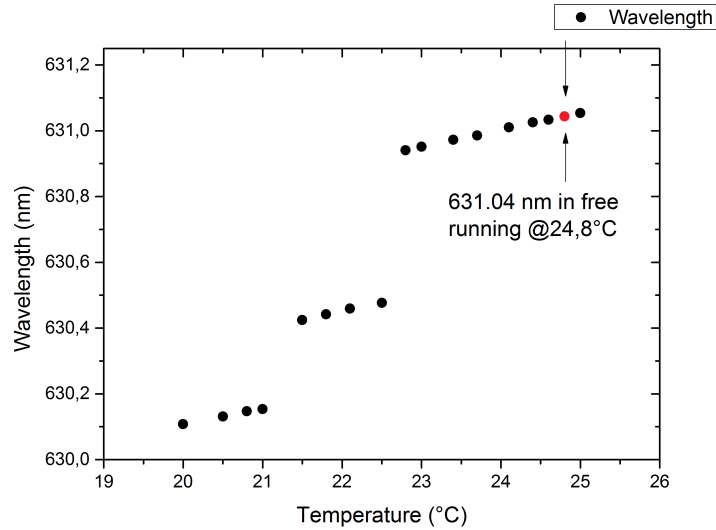


Figure 4.9: Laser output wavelength versus temperature of the diode holder. The current is fixed at 80 mA during the measurements. The continuous tuning behavior indicates the variation of the optical length of the cavity where the mode emitted longitudinally is not changed. Three mode jumps are also present indicating that the peak of the gain medium has shifted so far that the laser jumps to another mode. It is possible to notice that the erbium line is in the free running regime of the diode at a temperature of 24.8°C.

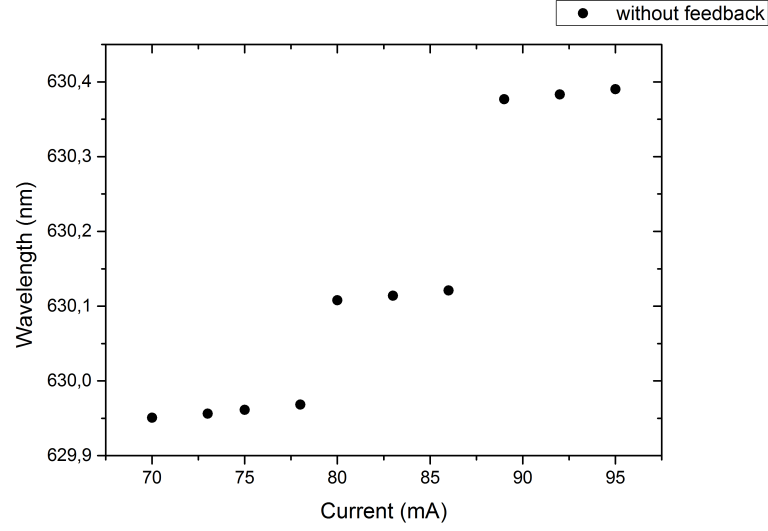


Figure 4.10: The wavelength reported from the wavemeter is registered for different currents. The current was always chosen to achieve a stable single mode emission. It is possible to notice the presence of the typical mode jump of the free running diode.

the threshold, since the laser power is more sensitive to optical feedback. The brightest spot ensures that the feedback is correctly retro-reflected. The alignment can then be optimized maximizing the output power. In our case the feedback is roughly 20% and this induces a power around 3-5 times higher than the power of the free running laser when the feedback is well aligned and the current is at the threshold. The wavelength range, which can be achieved rotating the cylindrical part, is (628 – 633) nm. The angle of the grating was adjusted to obtain approximately the Er line wavelength. The fine adjustment can be realized applying a voltage to the piezoelectric elements. The turn on characteristic (output power versus injection current) in the ECDL was repeated and the result is compared to the free running case in Fig. 4.11.

It is possible to notice that the threshold is 3 mA lower with respect to the free running laser as a result of the external optical feedback. Choosing the "right" amount of feedback fraction depends on the specific diode. It is important to verify that the lasing frequency in the ECDL is fixed by the angle of the grating. To check this, the wavelength was registered for different temperatures, repeating the measurements of Fig. 4.9 but in the external cavity configuration. Fig. 4.12 shows the correspondent measurements. It is possible to notice that the same variation of temperature ($\simeq 5^\circ\text{C}$) results in a total variation of 0.1 nm while, in the free running configuration, is of the 1 nm order. The diode is now forced to operate at the optical feedback wavelength [Lau02].

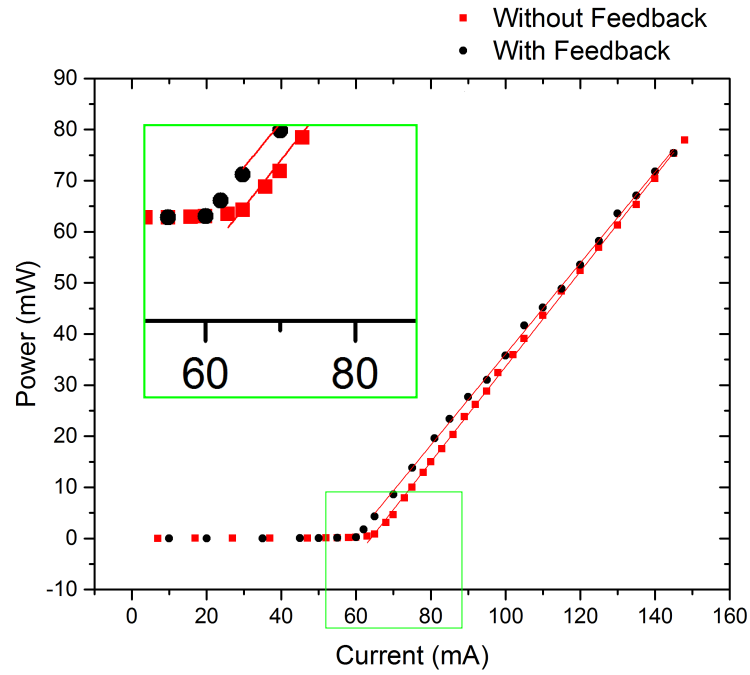


Figure 4.11: Power output versus injection current of the diode. The black points indicate the data of the free running diode, whereas the data in red are for the ECDL where the grating provides a feedback in the diode. Both measurements set are obtained at a temperature of 20°C. It is possible to notice the typical shift of the threshold, expected in the ECDL, from the relative zoom in green.

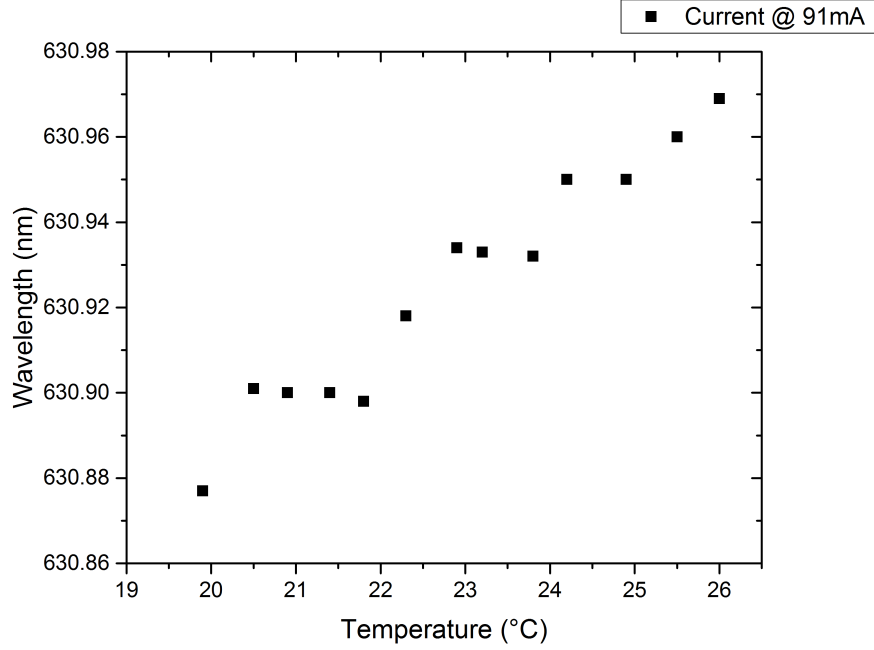


Figure 4.12: The wavelength is measured for different currents. It is possible to notice that the wavelength variation is much smaller with respect to the free running case.

4.2.3 Experimental setup

After testing the ECDL, we build the optical setup, as illustrated in Fig. 4.13. This setup has three main sections. First, a prism pair reduces the astigmatism of the beam then, two commercial faraday isolators⁵ give an high isolation (-35/dB each) and allow a stable use of the laser⁶. Using a combination of three polarizing beam splitters and a $\lambda/2$ wave plate it is possible to select the power of the three sections. To achieve a long-term stability the laser is locked to an ultra low expansion (ULE) cavity through the Pound Drever Hall (PDH) technique. The sidebands are generated through a fiber coupled EOM⁷. Details on the lock-in system are in Appendix A. From the 0th order of an acusto optic modulator (AOM) we realize the beam for the second section. The beam, which has a total power smaller than 200 μ W, is fiber-coupled to check the wavelength via a commercial wavemeter. Finally, in

⁵Thorlabs IO-3-633-LP.

⁶The setup was initially tested using only one isolator. The incredible high sensitivity of the diode to the additional optical feedback was making the use of it almost impossible. In particular during the scan of the piezo the power of the laser was distributed in different longitudinal mode. This high response to reflection is mainly due the low finesse and the small length of the internal cavity. As a result, the number of photons in cavity is low so that the laser frequency can be easily perturbed. As discussed in [NIS98] *"this unique feature can be both a blessing and a curse"*. In our case after adding a second isolator the laser could be stably used.

⁷Jenoptick PM 635.

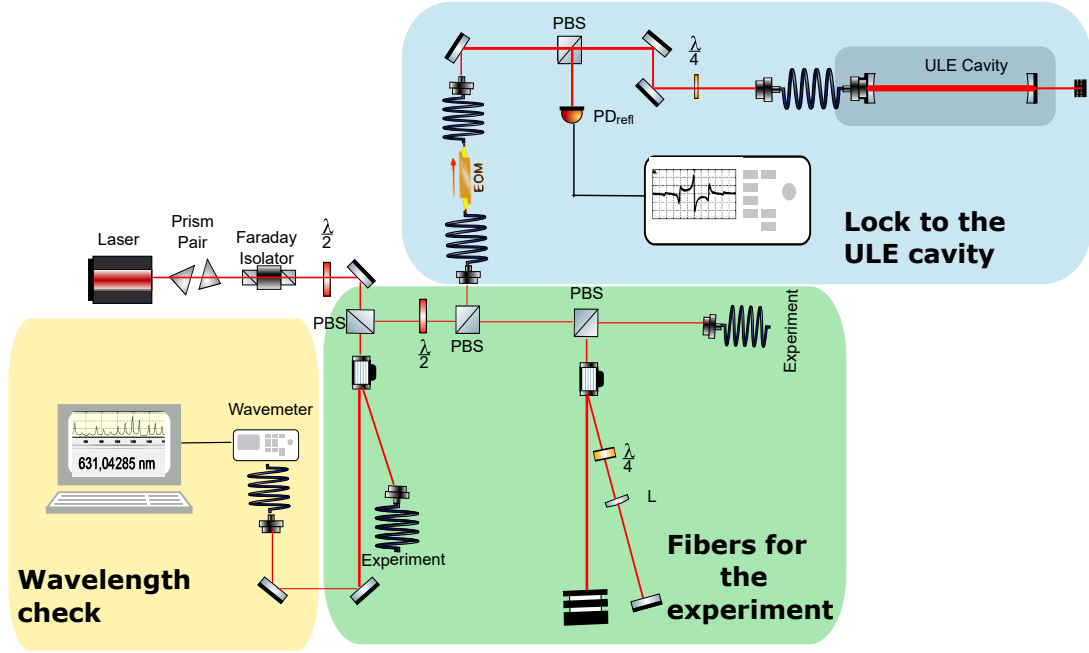


Figure 4.13: The optical setup is divided in three sections for the three different purposes. The power is divided between the sections using two half wave plates and three polarizing beam splitters ($\lambda/2$ and PBS respectively in the picture). The section underlined in blue is used to lock the wavelength of the laser to an ultralow-expansion cavity. This is achieved using a fiber coupled electro-optic modulator (EOM in the picture) to generate sidebands on the laser. The reflection from the cavity is sent to a photodetector (PD_{refl}). The section underlined in yellow is used to check wavelength of the laser using a commercial wavemeter. The 0th order of an AOM is fiber coupled and sent to the wavemeter. Finally, the section underlined in green is used to make two beams ready for the experiment. In particular two AOMs are used to stabilize the intensity of the two beams and to realize a tunable frequency shift between them.

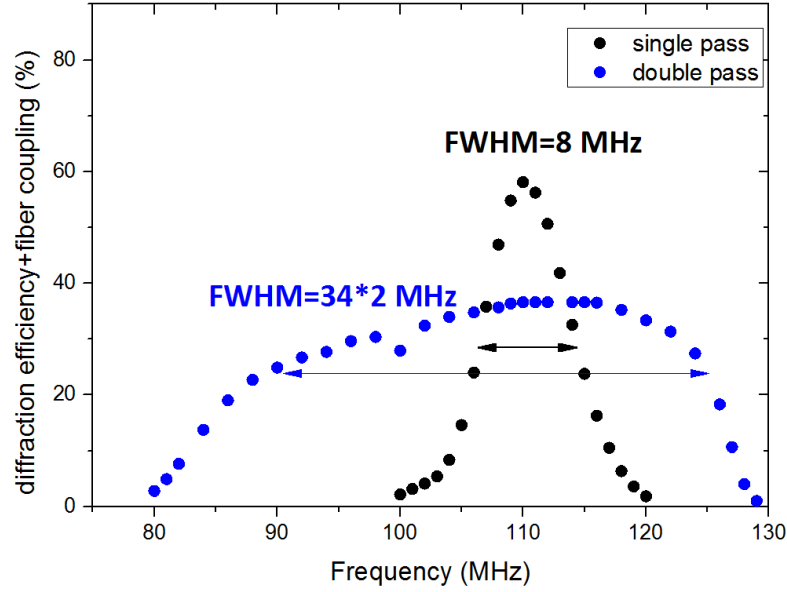


Figure 4.14: The overall efficiency, diffraction efficiency of the AOM plus fiber coupling efficiency is plotted versus the driving frequency of the AOM. It is possible to notice that using a double pass an increase of the bandwidth is obtained. The double pass beam is in fact not displaced when the frequency is changed. Since the fiber coupling remain almost the same the shape is mainly caused by the bandwidth of the AOM.

the last section two AOMs prepares the beams for the experiment. In one AOM, the +1 order, shifted in frequency of 110 MHz, is fiber coupled and sent to the experiment while, for the other AOM a double pass is realized using the -1 order. In this way two beams with a frequency difference of 3 times the AOM modulation frequency are obtained. Fig. 4.14 shows the frequency tunability of the double pass and of the single pass, where the overall efficiency, given by the diffraction efficiency of the AOM plus the fiber coupling efficiency, is considered. The FWHM spectral bandwidth is of 68 MHz for the double pass and of 8 MHz for the single pass it is possible to tune the frequency difference between the two experimental beams of 78 MHz. The role of the two AOMs is not only to allow for a controllable frequency shift on the MHz region but also to stabilize in intensity the beam. Dynamically changing the radio frequency power, which drives the AOM, it is in fact possible to change the fraction of the beam that is diffracted in the first order. The intensity seen by the atoms can be stabilized sampling a portion of the light sent to the experiment on a photodiode. The photodiode gives a voltage output proportional to the intensity of the beam. Using a reference voltage it is possible to obtain an error signal. A PI system is then used in combination with a voltage attenuator to change the RF power that drives the modulation.

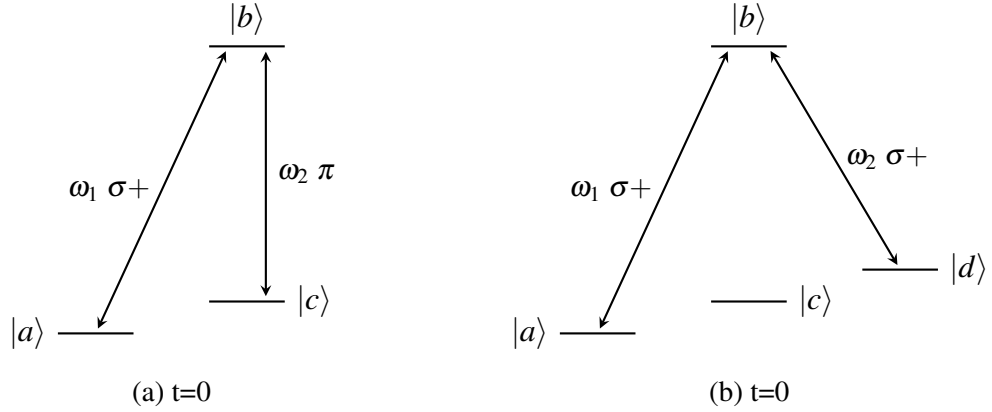


Figure 4.15: Optical pumping and depumping scheme. On the left a scheme to populate an adjacent spin state is shown. It consists of two resonant laser beams with σ^+ and π polarized light. On the right side it is shown the effect of two σ^+ polarized frequencies. It is possible in this way to skip the following spin state.

4.3 Overview on spin preparation/manipulation with light

The setup explained in the previous section was developed for different implementation schemes. As the quadratic Zeeman effect, also the quadratic light shift effect removes the degeneracy between the magnetic sublevels. This allows us to use a simple RF pulse or an adiabatic passage sweep to prepare a spin mixture, as we do for fermions, also for the bosonic isotopes. In addition, different schemes involving a higher excited state can be applied. In the following an overview on the variety of existing techniques to produce a spin preparation is given. We focus on the bosonic case. The techniques introduced are three: an optical pumping scheme, a Raman transition and a stimulated Raman adiabatic passage. They are illustrated using the formalism of the bosonic isotopes since in this case it is not possible to exploit the quadratic Zeeman effect. Finally, it is shown that exploiting the light it is also possible to manipulate the energy of the single spin state.

4.3.1 Optical pumping scheme

The optical pumping scheme relies on the use of resonant light combined with a magnetic bias field. The transition at 631 nm is a transition from $J = 6$ to a $J = 7$ state. This means that in the excited state 15 Zeeman sublevels are present and that all types of polarization can drive a transition to the excited state. This method depends strongly on the characteristic of the transition and in particular it is reliable thanks to the following two different factors: the different Landé g -factor of the excited state with respect to the ground state and the narrow linewidth of the excited state. Thus the resulting Zeeman splitting of the magnetic sublevels

of the ground state is different with respect to the magnetic sublevels of the excited state. The idea is shown in Fig. 4.15. Using one beam π polarized, atoms can be pumped from the initial states $(J, m_J) = (6, -6)$ to the excited state $(J, m_J) = (7, -6)$. Using also a σ^+ polarized beam, there are two different processes that can lead to a relaxation. Spontaneous emission from the excited state $(J, m_J) = (7, -6)$ can lead to a population of the $(m_J) = (-6, -5)$ magnetic sublevels of the ground state, with a different branching ratio. This process is slow in our case due to the long lifetime of the excited state, thus can be neglected. The other process is the stimulated emission as a result of the coupling induced by σ^+ light. This process transfers the population from $(J, m_J) = (7, -6)$ to the state $(J, m_J) = (6, -5)$. The atoms are now not anymore transferred by the radiation. In fact the light results not resonant for the coupling of $(J, m_J) = (6, -5)$ and $(J, m_J) = (7, -5)$, due to the different slope of equation (1.17) induced by the different Landè g-factor. In addition the quadratic spin dependent light shift, resulting from the use of resonant light, helps in removing the degeneracy. In addition as depicted in Fig. 4.15 (b) it is possible to obtain as final state $J = 6$, $m_J = -4$ using the two resonant frequencies σ^+ polarized. Due to the finite linewidth of the 631-nm line, the degeneracy is removed only at a magnetic field of 10 mG. From this field the detuning $\Delta = \mu_B(g'_J - g_J)B$ is much greater than the linewidth of the transition Γ^8 . In the ERBIUM experiment a reliable spin preparation using this method need particular care because of the heating rate induced by the use of resonant light and because of the laser frequency noise. In fact only with a B field of 10G the different resonances are separated by 1 MHz. This means that both the long term stability and the linewidth of the laser have to be below 100kHz.

4.3.2 Raman scheme

The Raman scheme relies on the use of an off-resonant light to populate the target state. Figure 4.16 shows a schematic diagram of two different schemes. Two laser beams are simultaneously used to couple the initial state to the final state. The frequency difference between the two beams has to be equal to the magnetic sublevels separation which is now given by the Zeeman splitting and the differential light shift. Once again, to avoid coupling with all the spin states, the beam detuning (Δ_1) has to be chosen to achieve a sufficiently large quadratic Stark shift and low heating. In addition it is important that the frequency of the beams is stable to avoid a change in the quadratic effect. Furthermore, the frequency difference of the beams has to be stable, below the differential quadratic shift induced. These conditions, using the setup in Fig. 4.13, are easily obtained since the laser beam is frequency

⁸If the laser linewidth is greater than the atomic linewidth it is necessary to consider the laser linewidth as Γ .

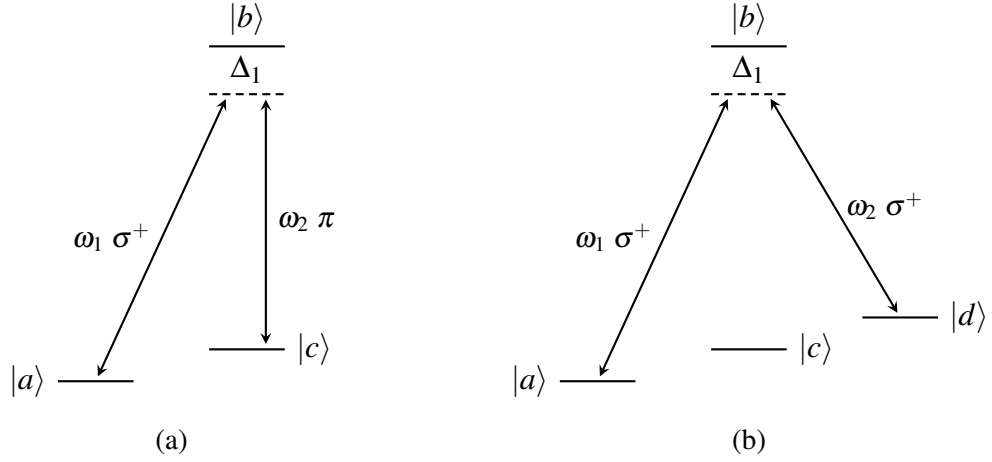


Figure 4.16: Two different Raman schemes. On the left, a scheme to populate an adjacent spin state is shown. It consists of two off resonant laser beams with σ^+ and π polarized light. The detuning Δ_1 has to be carefully chosen to obtain the desired quadratic effect. On the right side it is shown the effect of two σ^+ polarized frequencies. It is possible in this way to skip the following spin state.

locked to a ULE cavity and the frequency difference of the beams, since generated by the same laser, is only caused by the modulation RF the drives the AOMs⁹. In the case (a) of Fig. 4.16, one of the beams is σ^+ polarized, whereas the second is π polarized. In this case it is possible to transfer the population from the $m_J = -6$ to the $m_J = -5$. In the case (b), both beams are σ^+ polarized¹⁰ and the population can be transferred from the $m_J = -6$ to the $m_J = -4$.

4.3.3 Stimulated raman adiabatic passage

Another technique to transfer population between the magnetic sublevels is the stimulated Raman adiabatic passage (STIRAP). In its simplest version, this technique allows a coherent transfer of the population between two quantum states using an intermediate state. The three states are coupled together by two radiation fields switched on with a temporal delay. The use of a second optical field introduces the possibilities of exploiting the quantum interference in amplitude of the transition. Using a counterintuitive order for the time dependence of the intensity of the two beams an adiabatic transfer between the two states is possible. The main benefits of STIRAP are two. First, the spontaneous emission from the usually radiatively

⁹The frequency that drives the AOM is generated through two independent DDS that are automatically phase locked since they share the same reference clock.

¹⁰In this case using a bias field that realizes a splitting on the MHz range for adjacent spin states it is possible to drive one AOM with both frequencies removing the need of aligning two beams on the atoms.

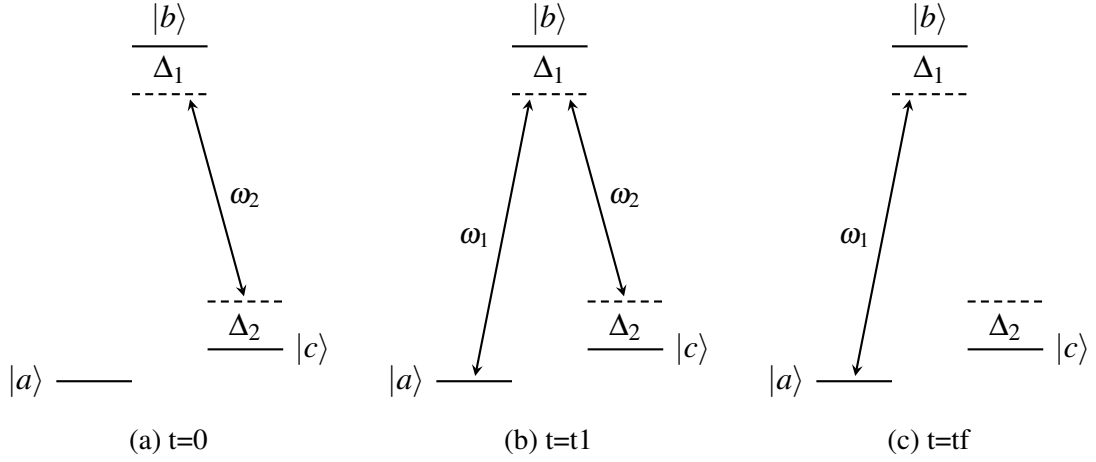


Figure 4.17: A Stirap scheme. In temporary order from the left to the right. Using this counterintuitive order for the time dependence of the intensity of the two beams an adiabatic transfer between the two states $|a\rangle$ and $|c\rangle$ is obtained. The intensity of the laser pulses has a delayed Gaussian shape. In (a) only the laser that couples the final state and the intermediate one is on. In the intermediate step both the lights reach the same intensity. In this step the transfer of the population started. In the final step the laser that couples the initial state and the intermediate one is gradually switched off. The best results are usually obtained in the double resonance condition $\Delta_1 = \Delta_2 = 0$.

decaying intermediate state is prevented despite the fact that the radiative lifetime of the intermediate state can be several orders of magnitude shorter than the length of the laser pulses. Second, as in the case of the adiabatic passage, it is robust against small fluctuations of the experimental conditions e.g magnetic field noise, intensity and frequency noise of the laser. The idea is drawn in Fig. 4.17c. As starting point, the intermediate state of the Raman scheme is coupled to the final magnetic sublevel with a Gaussian-shape pulse labeled from now on as pump beam (P). This coupling will not drive any transition of the population, which remains unchanged. These two states have to be now considered dressed by the radiation and as result these special Autler-Townes states do not interact with other optical fields present in the system. Then, while reducing the intensity of the probe beam, a second beam labeled Stokes (S), which couples the initial state to the intermediate one, is switched gradually increasing the intensity. In the beginning this field will not drive any transition to the two Autler-Townes states. Later, both the S and P laser beams are with comparable intensities. This stage is usually referred as adiabatic passage phase [Vit01]. Since on the two-photon resonance condition, one of the eigenstate of the Hamiltonian results in a superposition of the only initial and final state, where the weight is given by the ratio of the two Rabi frequencies involved, the population can be transferred in an adiabatic passage if an adequate length and delay of the two Gaussian pulses is chosen in such a way that, to

conclude the transfer, only the probe laser beam results on and slowly switched off. This counter intuitive coupling scheme is complicated by different factors in using Er. First, this three level population transfer will result in a multistate chain STIRAP-like population transfer and the necessary condition to realize the transfer to the higher magnetic sublevels is the existence of an eigenstate of the multilevel Hamiltonian that connects the initial state to the final one of the chain. Multistate STIRAP, formed by the Zeeman sublevels of $J=2$ system, has been demonstrated experimentally [Vit01]. Finally the different Landé g -factor of the excited states removes the resonant condition for the STIRAP to higher spin states. Whereas a transfer in the highest magnetic sublevels could be difficult using the 631-nm light, the quadratic magnetic sublevels dependence of the Stark shift leads to a decouple of higher magnetic states and an effective three level STIRAP scheme could work to transfer the population between the first two magnetic sublevels. In the setup the two intensity Gaussian profiles needed for the pulse can be realized dynamically changing the RF power of the acousto-optic modulators.

4.3.4 Single spin state manipulation

One of the more interesting features is that the applied laser field induces light shifts, which depends on m_J , i.e. on the magnetic sublevels. The different Landé g -factors can be additionally exploited to obtain a controllable shift of almost only one spin state in the ground manifold. The intensity of the beam, which can be dynamically modified¹¹ in the setup, can lead to a dynamical change of the energy of the coupled spin state. To achieve this effect the wavelength of the laser beam is locked close to a resonance between one magnetic sublevel of the ground state and the respectively one of the excited state according to the polarization of the laser beam. It is possible in this way to obtain a much bigger shift in the quasi-resonant states with respect to the other magnetic sublevels. The obtained AC-Stark shift can be calculated taking care of the different Landé g -factors. The resulting shift using an intensity of the laser beam of 1 W/mm^2 with a bias magnetic field of 30 G is plotted as a function of the detuning of the laser beam and it is shown in Fig. 4.19. In this way it is possible to prevent the population of the coupled level. To obtain a control over a single spin state, the requirements are even more stringent with respect to the spin preparation. To have a stable energy of the spin level working at 30 Gauss requires to have both long term stability and a linewidth of the laser below 50 kHz. Due to the high scattering rates of this quasi-resonant light the intensity used and the time duration has to be carefully chosen. This technique could be useful to follow spin phase protocol as for example to realize stripe phase [Maz17]

¹¹Changing the RF power that drives the AOM.

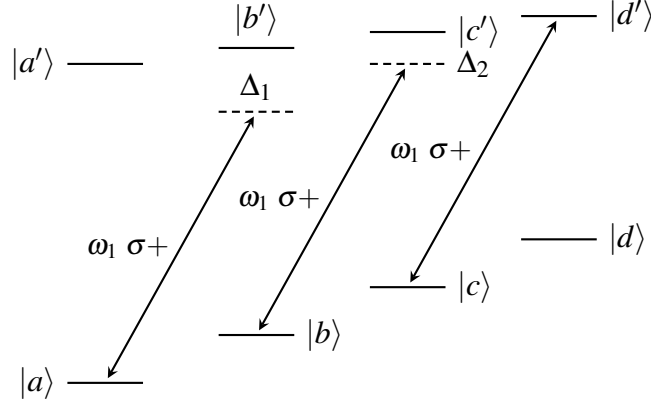


Figure 4.18: Four magnetic sublevels for the ground and the excited state are displayed. Only one spin state of the ground manifold is resonantly coupled. The two Autler-Townes states $|c\rangle$ $|d'\rangle$ receive now a shift that is much bigger with respect to the one induced in the other states. It is possible to dynamically change the shift changing the intensity of the beam.

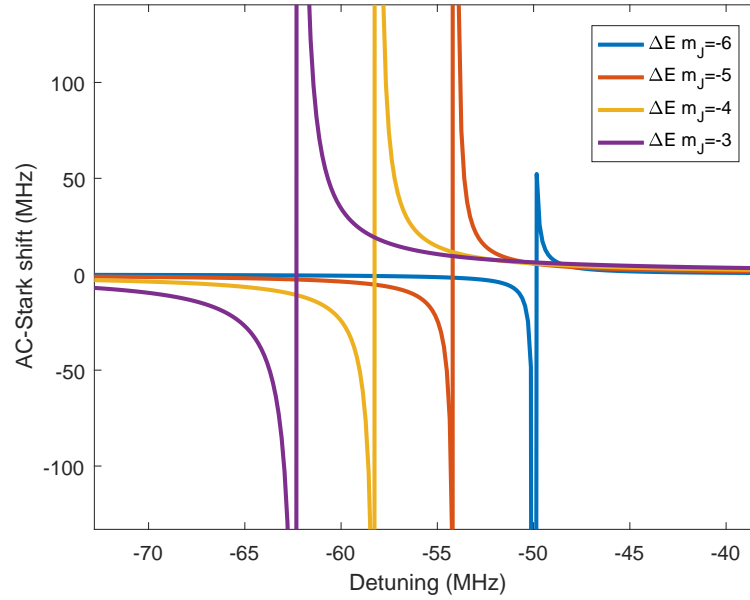


Figure 4.19: Total light shift for σ^+ polarization versus detuning for an interval of 8 MHz around the resonance. It is possible to distinguish the different spin states resonances.

Conclusion

The aim of my master thesis was to develop an optical setup which allows to obtain a deterministic spin preparation in the context of the ERBIUM experiment and to start the investigation of the rich physics behind spinor quantum gases [Sta13].

In the ground state Er has a total angular momentum $J=6$ ($F=19/2$) giving rise to 13 (20) different spin states for bosons (fermions). For bosons, the splitting induced by an external magnetic field B is linear and hence, a RF pulse that couples two adjacent spin states unavoidably couples all the spin states. These makes the spin preparation not straightforward. In the contrary, in the case of fermions, the magnetic moment of the nucleus couples to the magnetic field produced by the electrons of the atom, resulting in a quadratic splitting of the magnetic sublevels with the external B field. In this way, a RF pulse can couple only two magnetic sublevels. Working at magnetic fields higher than 20G, we achieved a deterministic spin preparation of the lowest two spin states using a RF pulse or a RF sweep. To optimize the sweep parameters and to get further understanding we simulated the RF transition with an Hamiltonian in the rotating frame approximation that qualitatively describes the experimental results.

Additionally, once we understood how to obtain a stable spin mixture, we loaded the atoms in a deep three-dimensional lattice, where several unexplored phases are predicted to occur with a spin mixture of highly magnetic atoms, e.g [Maz17]. In the ERBIUM experiment the lattice is created retro-reflecting 2 laser beams operating at 532nm and one operating at 1064nm. In particular, two beams coming from the 532-nm and one from the 1064-nm light sources are retro-reflected to obtain the 3D array of lattice sites. The beams cross each others orthogonally. In this lattice we investigated the interactions between the lowest spin states by estimating the onsite interaction U . We showed that this quantity preserves the anisotropic character of the dipole-dipole interactions of Er. We measured this value for two different dipole orientation and find a good agreements with the theory. Additionally, as a step towards the predicted phases, we present a method to obtain a deterministic spin preparation and a single spin state control, which exploits the tensorial ac-Stark shift and can be implemented for both fermionic and bosonic isotopes. For this aim, we developed an External Cavity

Diode Laser (ECDL) source, emitting close to a narrow transition at 631 nm, together with an optical setup that allows different schemes for spin manipulation. The laser was intensity stabilized using the acusto-optic modulator technology and frequency stabilized using the Pound-Drever-Hall technique. This study provides new elements to increase the knowledge of our system and opens the door to investigate quantum magnetism and the stability of ordered magnetic phases in a well-controlled manner.

Bibliography

- [Ahm05] Ahmadi, P., Timmons, B. P., and Summy, G. S. “Geometrical effects in the loading of an optical atom trap”. *Phys. Rev. A* 72 (2 Aug. 2005), p. 023411. DOI: 10.1103/PhysRevA.72.023411. URL: <https://link.aps.org/doi/10.1103/PhysRevA.72.023411> (cit. on p. 19).
- [Aik12] Aikawa, K., Frisch, A., Mark, M., Baier, S., Rietzler, A., Grimm, R., and Ferlaino, F. “Bose-Einstein condensation of erbium”. *Physical Review Letters* 108.21 (2012). ISSN: 00319007. DOI: 10.1103/PhysRevLett.108.210401. arXiv: 1204.1725 (cit. on p. 20).
- [And95] Anderson, M. H., Ensher, J. R., Matthews, M. R., Wieman, C. E., and Cornell, E. A. “Observation of Bose-Einstein Condensation in a Dilute Atomic Vapor”. *Science* 269.5221 (1995), pp. 198–201. ISSN: 0036-8075. DOI: 10.1126/science.269.5221.198. arXiv: arXiv:1011.1669v3. URL: <http://www.sciencemag.org/cgi/doi/10.1126/science.269.5221.198> (cit. on p. 1).
- [Ani91] Anisimov, Vladimir I., Zaanen, Jan, and Andersen, Ole K. “Band theory and Mott insulators: Hubbard U instead of Stoner I”. *Phys. Rev. B* 44 (3 July 1991), pp. 943–954. DOI: 10.1103/PhysRevB.44.943. URL: <https://link.aps.org/doi/10.1103/PhysRevB.44.943> (cit. on p. 36).
- [Bai12] Baier, S. “An optical dipole trap for Erbium with tunable geometry”. PhD thesis. 2012 (cit. on pp. 2, 19, 43).
- [Ban05] Ban, H. Y., Jacka, M., Hanssen, J. L., Reader, J., and McClelland, J. J. “Laser cooling transitions in atomic erbium”. *Opt. Express* 13.8 (Apr. 2005), pp. 3185–3195. DOI: 10.1364/OPEX.13.003185. URL: <http://www.opticsexpress.org/abstract.cfm?URI=oe-13-8-3185> (cit. on p. 49).
- [Bar04] Baranov, M. A., Dobrek, and Lewenstein, M. “Superfluidity of trapped dipolar Fermi gases”. *Physical Review Letters* 92.25 I (2004), pp. 250403–1. ISSN: 00319007. DOI: 10.1103/PhysRevLett.92.250403. arXiv: 0307671 [cond-mat] (cit. on p. 20).
- [Bar12] Baranov, M. A., Dalmonte, M., Pupillo, G., and Zoller, P. *Condensed matter theory of dipolar quantum gases*. 2012. DOI: 10.1021/cr2003568. arXiv: 1207.1914 (cit. on p. 33).
- [Bla98] Black, Eric. “Notes on the Pound-Drever-Hall technique”. *Technology* 4.617 (1998), pp. 16–98. URL: <http://www.ligo.caltech.edu/%7B~%7Djay/documents/NotesOnPoundDreverHallLocking.pdf> (cit. on p. 81).

- [Blo05] Bloch, Immanuel. “Ultracold quantum gases in optical lattices”. *Nature Physics* 1.1 (2005), pp. 23–30. ISSN: 1745-2473. DOI: 10.1038/nphys138. arXiv: 0912.3646. URL: <http://www.nature.com/doifinder/10.1038/nphys138> (cit. on p. 34).
- [Blo12] Bloch, Immanuel, Dalibard, Jean, and Nascimbène, Sylvain. “Quantum simulations with ultracold quantum gases”. *Nature Physics* 8.4 (2012), pp. 267–276. ISSN: 1745-2473. DOI: 10.1038/nphys2259. arXiv: nphys2259 [10.1038]. URL: <http://www.nature.com/doifinder/10.1038/nphys2259> (cit. on p. 34).
- [Blo14] Bloom, B. J., Nicholson, T. L., Williams, J. R., Campbell, S. L., Bishof, M., Zhang, X., Zhang, W., Bromley, S. L., and Ye, J. “An optical lattice clock with accuracy and stability at the 10⁻¹⁸ level”. *Nature* 506.7486 (2014), pp. 71–75. ISSN: 0028-0836. DOI: 10.1038/nature12941. arXiv: 1309.1137. URL: <http://www.nature.com/doifinder/10.1038/nature12941> (cit. on p. 79).
- [Bon09] Bonn, J. L., Cavagnero, M., and Ticknor, C. “Quasi-universal dipolar scattering in cold and ultracold gases”. *New Journal of Physics* 11 (2009). ISSN: 13672630. DOI: 10.1088/1367-2630/11/5/055039. arXiv: 0901.1281 (cit. on p. 20).
- [Bor28] Born, M. and Fock, V. “Beweis des Adiabatsatzes”. *Zeitschrift fuer Physik* 51.3-4 (1928), pp. 165–180. ISSN: 14346001. DOI: 10.1007/BF01343193 (cit. on p. 29).
- [Bos24] Bose. “Plancks Gesetz und Lichtquantenhypothese”. *Zeitschrift fuer Physik* 26.1 (1924), pp. 178–181. ISSN: 14346001. DOI: 10.1007/BF01327326 (cit. on p. 1).
- [Bra83] Bransden, B H and Joachin, C J. *Physics of atoms and molecules.pdf*. 1983. DOI: 10.1887/0750303468/b293c2. URL: http://books.google.com/books?id=b6x%7B%5C_%7Dz8nZbw0C%7B%5C&%7Ddq (cit. on p. 7).
- [Cha13] Chakraborty, Subhadeep. “Advantages of Blackman Window over Hamming Window Method for designing FIR Filter”. *International Journal of Computer Science & Engineering Technology (IJCSET)* 4.08 (2013), pp. 1181–1189. URL: <http://ijcset.com/docs/IJCSET13-04-08-030.pdf> (cit. on p. 27).
- [Chi10] Chin, Cheng, Grimm, Rudolf, Julienne, Paul, and Tiesinga, Eite. “Feshbach resonances in ultracold gases”. *Rev. Mod. Phys.* 82 (2 Apr. 2010), pp. 1225–1286. DOI: 10.1103/RevModPhys.82.1225. URL: <https://link.aps.org/doi/10.1103/RevModPhys.82.1225> (cit. on p. 1).
- [Cho16] Chomaz, L., Baier, S., Petter, D., Mark, M. J., Wächtler, F., Santos, L., and Ferlaino, F. “Quantum-Fluctuation-Driven Crossover from a Dilute Bose-Einstein Condensate to a Macrodroplet in a Dipolar Quantum Fluid”. *Phys. Rev. X* 6 (4 Nov. 2016), p. 041039. DOI: 10.1103/PhysRevX.6.041039. URL: <https://link.aps.org/doi/10.1103/PhysRevX.6.041039> (cit. on p. 1).
- [Coh11] Cohen-Tannoudji, Claude and Guéry-Odelin, David. *Advances in Atomic Physics: An Overview*. World Scientific Publishing Company, 2011. ISBN: 9789812774965 (cit. on p. 21).
- [Dav95] Davis, K. B., Mewes, M. O., Andrews, M. R., Van Druten, N. J., Durfee, D. S., Kurn, D. M., and Ketterle, W. “Bose-Einstein condensation in a gas of sodium atoms”. *Physical Review Letters* 75.22 (1995), pp. 3969–3973. ISSN: 00319007. DOI: 10.1103/PhysRevLett.75.3969. arXiv: 9604005 [quant-ph] (cit. on p. 1).

- [De 25] De Broglie, Louis. “Recherches sur la théorie des quanta”. *Annales de la fondation Louis De Broglie* 17.1 (1925) (cit. on p. 1).
- [DeM99] DeMarco, B. “Onset of Fermi Degeneracy in a Trapped Atomic Gas”. *Science* 285.5434 (1999), pp. 1703–1706. ISSN: 00368075. DOI: 10.1126/science.285.5434.1703. URL: <http://www.sciencemag.org/cgi/doi/10.1126/science.285.5434.1703> (cit. on p. 1).
- [Dut14] Dutta, Omjyoti, Gajda, Mariusz, Hauke, Philipp, Lewenstein, Maciej, Lühmann, Dirk-Sören, Malomed, Boris A., Sowiński, Tomasz, and Zakrzewski, Jakub. “Non-standard Hubbard models in optical lattices: a review”. (June 2014). DOI: 10.1088/0034-4885/78/6/066001. arXiv: 1406.0181. URL: <http://arxiv.org/abs/1406.0181> (cit. on pp. 2, 33, 36).
- [Ein25] Einstein, A. “Quantum Theory of a Monoatomic Ideal Gas A translation of Quantentheorie des einatomigen idealen Gases (Einstein , 1924)”. *Sitzungsberichte der Preuss. Akad. der Wissenschaften* 1.3 (1925), pp. 1–5. DOI: 10.1002/3527608958.ch27 (cit. on p. 1).
- [Fri12] Frisch, A., Aikawa, K., Mark, M., Rietzler, A., Schindler, J., Zupanič, E., Grimm, R., and Ferlaino, F. “Narrow-line magneto-optical trap for erbium”. *Physical Review A - Atomic, Molecular, and Optical Physics* 85.5 (2012). ISSN: 10502947. DOI: 10.1103/PhysRevA.85.051401. arXiv: arXiv:1203.1460v2 (cit. on p. 7).
- [Fri14] Frisch, Albert. “Dipolar Quantum Gases of Erbium”. PhD thesis. 2014 (cit. on pp. 6, 9, 17, 18, 25).
- [Gre02] Greiner, Markus, Mandel, Olaf, Esslinger, Tilman, Hänsch, Theodor W., and Bloch, Immanuel. “Quantum phase transition from a superfluid to a Mott insulator in a gas of ultracold atoms”. *Nature* 415.6867 (2002), pp. 39–44. ISSN: 00280836. DOI: 10.1038/415039a. URL: <http://www.nature.com/doi/10.1038/415039a> (cit. on p. 2).
- [Gre03] Greiner, Markus. “Ultracold quantum gases in three-dimensional optical lattice potentials”. PhD thesis. 2003, pp. 1–134. URL: papers2://publication/uuid/231B7D43-A8B7-41D3-9791-AF4C7F41717F (cit. on p. 35).
- [Gri00] Grimm, Rudolf, Weidemüller, Matthias, and Ovchinnikov, Yurii B. “Optical Dipole Traps for Neutral Atoms”. *Advances in Atomic, Molecular and Optical Physics* 42.C (2000), pp. 95–170. ISSN: 1049250X. DOI: 10.1016/S1049-250X(08)60186-X. arXiv: 9902072 [physics] (cit. on p. 46).
- [Hub63] Hubbard, J. “Electron Correlations in Narrow Energy Bands”. *Proceedings of the Royal Society A: Mathematical, Physical and Engineering Sciences* 276.1365 (1963), pp. 238–257. ISSN: 1364-5021. DOI: 10.1098/rspa.1963.0204. arXiv: arXiv:1205.0516v2. URL: <http://rspa.royalsocietypublishing.org/cgi/doi/10.1098/rspa.1963.0204> (cit. on p. 36).
- [Jen91] Jensen, Jens and Mackintosh, a.R. “Rare earth magnetism: structures and excitations”. *Physics* (1991), p. 403. URL: <http://www.fys.ku.dk/%7B~%7Djensen/Book/Ebook.pdf> (cit. on p. 5).
- [Jud61] Judd, B. R. and Lindgren, I. “Theory of Zeeman effect in the ground multiplets of rare-earth atoms”. *Physical Review* 122.6 (1961), pp. 1802–1812. ISSN: 0031899X. DOI: 10.1103/PhysRev.122.1802 (cit. on p. 9).

- [Kao17] Kao, Wil, Tang, Yijun, Burdick, Nathaniel Q., and Lev, Benjamin L. “Anisotropic dependence of tune-out wavelength near Dy 741-nm transition”. *Optics Express* 25.4 (2017), p. 3411. ISSN: 1094-4087. DOI: 10.1364/OE.25.003411. arXiv: 1609.02111. URL: <http://arxiv.org/abs/1609.02111%7B%5C%%7D5Cnhttps://www.osapublishing.org/abstract.cfm?URI=oe-25-4-3411> (cit. on p. 52).
- [Kes12] Kessler, T., Hagemann, C., Grebing, C., Legero, T., Sterr, U., Riehle, F., Martin, M. J., Chen, L., and Ye, J. “A sub-40-mHz-linewidth laser based on a silicon single-crystal optical cavity”. *Nature Photonics* 6.10 (2012), pp. 687–692. ISSN: 1749-4885. DOI: 10.1038/nphoton.2012.217. arXiv: 1112.3854. URL: <http://www.nature.com/doifinder/10.1038/nphoton.2012.217> (cit. on p. 79).
- [Ket96] Ketterle, W. and Druten, N.J. Van. *Evaporative Cooling of Trapped Atoms*. 1996. DOI: 10.1016/S1049-250X(08)60101-9. arXiv: 1306.5950. URL: <http://www.sciencedirect.com/science/article/pii/S1049250X08601019> (cit. on p. 19).
- [Kir15] Kirilov, E., Mark, M. J., Segl, M., and Nägerl, H. C. “Compact, robust, and spectrally pure diode-laser system with a filtered output and a tunable copy for absolute referencing”. *Applied Physics B: Lasers and Optics* 119.2 (2015), pp. 233–240. ISSN: 09462171. DOI: 10.1007/s00340-015-6049-5. arXiv: 1412.1116 (cit. on p. 54).
- [Kno08] Knoop, S., Ferlaino, F., Mark, M., Berninger, M., Schoebel, H., Naegerl, H. -C., and Grimm, R. “Observation of an Efimov-like resonance in ultracold atom-dimer scattering”. *Nature Physics* 5.3 (2008), p. 12. ISSN: 1745-2473. DOI: 10.1038/nphys1203. arXiv: 0807.3306. URL: <http://arxiv.org/abs/0807.3306> (cit. on p. 1).
- [Kol06] Kollath, C., Iucci, A., Giamarchi, T., Hofstetter, W., and Schollwoeck, U. “Spectroscopy of ultracold atoms by periodic lattice modulations”. *Physical Review Letters* 97.5 (2006). ISSN: 00319007. DOI: 10.1103/PhysRevLett.97.050402. arXiv: 0603721 [cond-mat] (cit. on p. 39).
- [Lah09] Lahaye, T, Menotti, C, Santos, L, Lewenstein, M, and Pfau, T. “The physics of dipolar bosonic quantum gases”. *Reports on Progress in Physics* 72.12 (2009), p. 126401. ISSN: 0034-4885. DOI: 10.1088/0034-4885/72/12/126401. arXiv: arXiv:0905.0386v1. URL: <http://stacks.iop.org/0034-4885/72/i=12/a=126401?key=crossref.f3ade09a61129cb9af3a519307f064f7> (cit. on p. 12).
- [Lan72] Langhoff, P. W., Epstein, S. T., and Karplus, M. “Aspects of time-dependent perturbation theory”. *Reviews of Modern Physics* 44.3 (1972), pp. 602–644. ISSN: 00346861. DOI: 10.1103/RevModPhys.44.602 (cit. on p. 46).
- [Lau02] Laurila, Toni, Joutsenoja, Timo, Hernberg, Rolf, and Kuittinen, Markku. “Tunable external-cavity diode laser at 650 nm based on a transmission diffraction grating.” *Applied optics* 41.27 (2002), pp. 5632–5637. ISSN: 0003-6935. DOI: 10.1364/AO.41.005632 (cit. on p. 59).
- [Lep14] Lepers, M., Wyart, J. F., and Dulieu, O. “Anisotropic optical trapping of ultracold erbium atoms”. *Physical Review A - Atomic, Molecular, and Optical Physics* 89.2 (2014). ISSN: 10502947. DOI: 10.1103/PhysRevA.89.022505. arXiv: arXiv:1310.6149v1 (cit. on pp. 46, 48).

- [Li17] Li, Hui, Wyart, Jean François, Dulieu, Olivier, and Lepers, Maxence. “Anisotropic optical trapping as a manifestation of the complex electronic structure of ultracold lanthanide atoms: The example of holmium”. *Physical Review A* 95.6 (2017). ISSN: 24699934. DOI: 10.1103/PhysRevA.95.062508. arXiv: 1704.04134 (cit. on p. 46).
- [Lia12] Lian, Biao, Ho, Tin-Lun, and Zhai, Hui. “Searching for non-Abelian phases in the Bose-Einstein condensate of dysprosium”. *Phys. Rev. A* 85 (5 May 2012), p. 051606. DOI: 10.1103/PhysRevA.85.051606. URL: <https://link.aps.org/doi/10.1103/PhysRevA.85.051606> (cit. on p. 20).
- [Lid10] Lide, D.R. “CRC Handbook of Chemistry and Physics, 90th Edition”. CRC Handbook of Chemistry and Physics, 90th Ed. Taylor & Francis, 2010, pp. 14–19. ISBN: 9780849304859 (cit. on p. 4).
- [Mar07] Mark, Manfred Johann. “Wechselwirkungseffekte eines Cäsium-BEC in eindimensionalen Gittern”. *Thesis* November (2007) (cit. on p. 81).
- [Mar78] Martin, W. C. “Atomic energy levels: The rare earth elements (the spectra of lanthanum, cerium, praseodymium, neodymium, promethium, samarium, europium, gadolinium, terbium, dysprosium, holmium, erbium, thulium, ytterbium, and lutetium)”. *Unknown* (1978). DOI: 10.6028/NBS.NSRDS.60. URL: <http://adsabs.harvard.edu/abs/1978aelsr.rept.....M> (cit. on pp. 9, 10).
- [Maz16] Mazurenko, Anton, Chiu, Christie S., Ji, Geoffrey, Parsons, Maxwell F., Kanász-Nagy, Márton, Schmidt, Richard, Grusdt, Fabian, Demler, Eugene, Greif, Daniel, and Greiner, Markus. “Experimental realization of a long-range antiferromagnet in the Hubbard model with ultracold atoms”. 2 (2016), pp. 1–15. ISSN: 0002838X. DOI: 10.1038/nature22362. arXiv: 1612.08436. URL: <http://arxiv.org/abs/1612.08436> (cit. on p. 2).
- [Maz17] Mazloom, Azadeh, Vermersch, Benoît, Baranov, Mikhail A., and Dalmonte, Marcello. “Adiabatic state preparation of stripe phases with strongly magnetic atoms”. *arXiv* (2017). DOI: 10.1103/PhysRevA.96.033602. arXiv: 1702.04662. URL: <http://arxiv.org/abs/1702.04662> (cit. on pp. 3, 20, 33, 68, 70).
- [Mew97] Mewes, M.-O., Andrews, M. R., Kurn, D. M., Durfee, D. S., Townsend, C. G., and Ketterle, W. “Output Coupler for Bose-Einstein Condensed Atoms”. *Phys. Rev. Lett.* 78 (4 Jan. 1997), pp. 582–585. DOI: 10.1103/PhysRevLett.78.582. URL: <https://link.aps.org/doi/10.1103/PhysRevLett.78.582> (cit. on p. 27).
- [Mon10] Monmayrant, Antoine, Weber, Sébastien, and Chatel, Béatrice. “A newcomer’s guide to ultrashort pulse shaping and characterization”. *Journal of Physics B: Atomic, Molecular and Optical Physics* 43.10 (2010), p. 103001. ISSN: 0953-4075. DOI: 10.1088/0953-4075/43/10/103001. URL: <http://stacks.iop.org/0953-4075/43/i=10/a=103001?key=crossref.a3845bf6ff5ac8d2545d08312eb698> (cit. on p. 27).
- [Nic13] Nickerson, M. “A review of Pound-Drever-Hall laser frequency locking”. *Post* (2013) (cit. on p. 81).
- [NIS98] NIST. *Precision Spectroscopy, Diode Lasers, and Optical Frequency Measurement Technology*. 1998, p. 296. ISBN: 3034973276 (cit. on p. 61).
- [Pat17] Patscheider, Alexander. “Stable Reference Cavity for Er and Dy MOT Light”. master’s thesis. 2017 (cit. on p. 79).

- [Pat83] Patzak, E., Sugimura, a., Saito, S., Mukai, T., and Olesen, H. “Semiconductor laser linewidth in optical feedback configurations”. *Electronics Letters* 19.24 (1983), p. 1026. ISSN: 00135194. DOI: 10.1049/el:19830695. URL: http://digital-library.theiet.org/content/journals/10.1049/el%7B%5C_%7D19830695 (cit. on p. 82).
- [Pfa97] Pfau, T., Müller-Seydlitz, T., Hartl, M., Brezger, B., Hänsel, H., Keller, C., Spreeuw, R. J. C., and Mlynek, J. “Atoms in the lowest motional band of a 3D optical lattice”. *Quantum Electronics and Laser Science Conference*. Optical Society of America, 1997, QTuJ2. URL: <http://www.osapublishing.org/abstract.cfm?URI=QELS-1997-QTuJ2> (cit. on p. 37).
- [Pit16] Pitaevskii, Lev and Stringari, Sandro. *Bose-Einstein Condensation and Superfluidity*. Oxford Science Publications, 2016, p. 576 (cit. on p. 20).
- [Raa87] Raab, E. L., Prentiss, M., Cable, Alex, Chu, Steven, and Pritchard, D. E. “Trapping of Neutral Sodium Atoms with Radiation Pressure”. *Physical Review Letters* 59.23 (1987), pp. 2631–2634. ISSN: 00319007. DOI: 10.1103/PhysRevLett.59.2631. arXiv: arXiv:1009.2475v1 (cit. on p. 18).
- [Rie04] Riehle, Fritz. *Frequency Standards*. 2004, pp. 767–775. ISBN: 3-527-40230-6. DOI: 10.1002/3527605991. URL: <http://doi.wiley.com/10.1002/3527605991> (cit. on p. 54).
- [Rie12] Rietzler, A. “Narrow-Line Cooling Light for a Magneto-Optical Trap of Erbium Atoms”. master’s thesis. 2012 (cit. on pp. 79, 82).
- [San06] Santos, L. and Pfau, T. “Spin-3 Chromium Bose-Einstein Condensates”. *Phys. Rev. Lett.* 96 (19 May 2006), p. 190404. DOI: 10.1103/PhysRevLett.96.190404. URL: <https://link.aps.org/doi/10.1103/PhysRevLett.96.190404> (cit. on p. 20).
- [Sta13] Stamper-Kurn, Dan M. and Ueda, Masahito. “Spinor Bose gases: Symmetries, magnetism, and quantum dynamics”. *Reviews of Modern Physics* 85.3 (2013), pp. 1191–1244. ISSN: 00346861. DOI: 10.1103/RevModPhys.85.1191. arXiv: 1205.1888 (cit. on pp. 16, 70).
- [Stö04] Stöferle, Thilo, Moritz, Henning, Schori, Christian, Köhl, Michael, and Esslinger, Tilman. “Transition from a strongly interacting 1D superfluid to a Mott insulator”. *Physical Review Letters* 92.13 (2004), pp. 130403–1. ISSN: 00319007. DOI: 10.1103/PhysRevLett.92.130403. arXiv: 0312440 [cond-mat] (cit. on p. 39).
- [Sve10] Svelto, Orazio. *Principles of lasers*. 2010, pp. 1–620. ISBN: 9781441913012. DOI: 10.1007/978-1-4419-1302-9. arXiv: arXiv:1011.1669v3 (cit. on p. 79).
- [Tro78] Troitskiĭ, Yu V. “Optimization and comparison of the characteristics of optical interference discriminators”. *Soviet Journal of Quantum Electronics* 8.5 (1978), pp. 628–631. ISSN: 0049-1748. DOI: 10.1070/QE1978v008n05ABEH010175. URL: <http://stacks.iop.org/0049-1748/8/i=5/a=A20?key=crossref.b9dcc394d8a9ca1fa3c960bd54c911bd> (cit. on p. 80).
- [Vex11] Vexiau, R., Bouloufa, N., Aymar, M., Danzl, J. G., Mark, M. J., Nägerl, H. C., and Dulieu, O. “Optimal trapping wavelengths of Cs₂ molecules in an optical lattice”. *European Physical Journal D* 65.1-2 (2011), pp. 243–250. ISSN: 14346060. DOI: 10.1140/epjd/e2011-20085-4. arXiv: 1102.1793 (cit. on p. 47).

- [Vit01] Vitanov, N. V., Fleischhauer, M., Shore, B. W., and Bergmann, K. “Coherent manipulation of atoms and molecules by sequential laser pulses”. *Advances in Atomic, Molecular and Optical Physics* 46.C (2001), pp. 55–190. ISSN: 1049250X. DOI: 10.1016/S1049-250X(01)80063-X (cit. on pp. 67, 68).

Appendix A

Lock of the laser system

Ultra-stable laser sources are fundamental tools in ultracold atoms experiments. Even more if the laser is adopted to realize a reliable and reproducible spin preparation. The idea of laser locking is to use a stable optical cavity as a reference to reduce frequency fluctuations or long-term drifts and hence to transfer the stability of the cavity to the laser. The requirements is a tunable laser source, which allows to dynamically change the laser frequency in such a way to match the resonant mode of the cavity. In the last years the necessity of stable resonators for several research topics, e.g. atomic clock [Blo14], drove the development of optical cavities more and more accurate and stable [Kes12]. In our experiment, we use an ultra-low expansion (ULE) cavity¹ with optically-contacted mirrors [Rie12; Pat17] In our case, and in general with diode laser in Littrow configuration, the tunability is usually achieved by varying the current or rotating the grating. In particular, the former is used to responds to fast fluctuations (> 1 kHz) of the wavelength. The latter controls the angle of the grating, as shown in figure tot, and respond to slow fluctuations (up to 1 kHz).

The locking scheme relies on the coupling between cavity and laser light. The light is transmitted by the cavity only if the laser frequency matches one of the Airy peaks [Sve10], in such a way that, for a Fabry-Perot cavity, two times the length of the cavity is a integer multiple of the wavelength. If the laser operates off resonance with respect to the cavity transmission peaks, the light is reflected out from the cavity. Thus, one can try to lock the laser using the transmitted signal from the cavity and stabilize the laser. Since both transmission and reflection are symmetric with respect to the resonance, one needs to lock the laser at one side of this resonance, where a change of intensity can be directly converted to a frequency change. This was how lock was performed before the Pound Drever Hall (PDH) technique. One of the disadvantageous of this technique is that power fluctuations are not decoupled from frequency fluctuations. Indeed, if the laser power changes, the feedback

¹Made of a special glass the has low thermal expansion coefficient.

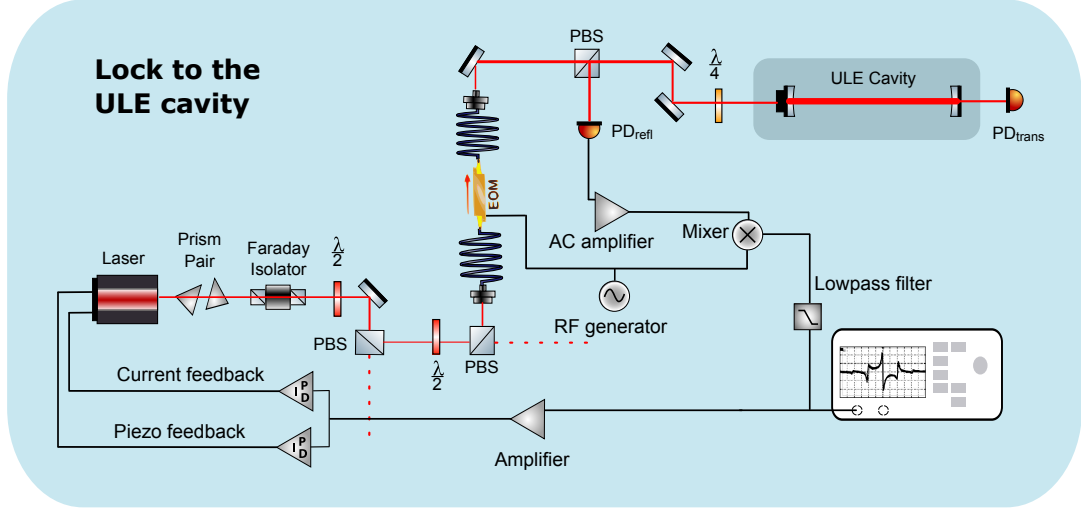


Figure A.1: Level occupation given in the equations (2.3) and (2.5) as function of the energy ε for the Bose-Einstein (blue), Fermi-Dirac (red) statistics. For comparison also the Maxwell-Boltzmann (yellow) is included.

response is the same as if the laser frequency drifts out. Thus, to improve a lock realized with this technique, the laser beam sent through the cavity has to be intensity stabilised [Tro78]. Furthermore, using the transmitted light increases the shot noise.

Today, the standard technique adopted to achieve a long-term stability is the PDH. In this technique one exploits the use of the reflected light, where the signal on the photodiode can be reduced to zero and the resulting lock can achieve better performance. Since the reflected signal from the cavity is symmetric around the resonance, one should look at the derivative. This is easily achieved by slightly modulating the phase or the frequency of the laser. The variation of the reflection induced by the modulation tells us on which side of the resonance the laser is sitting. Furthermore, it gives us the possibility to realize an error signal, which can be easily sent to the laser electronics control as a feedback.

Figure A.1 shows the layout used in the lab, where the electronics adopted for the lock is included to fully understand the working principle of the laser locking. The EOM in the picture works as a phase modulator. The signal coming from the reflection of the cavity is sent to a photodiode through the combination of a $\lambda/2$ waveplate and a polarizing beam splitter. The signal from the detector is then amplified and sent to a commercial mixer² together with the same signal that drives the EOM. This latter is generated from a DDS and splitted by a commercial splitter³. The mixer multiplies both signals in such a way that the result, after an

²Minicircuit

³Minicircuit ZFSC-2-1W+

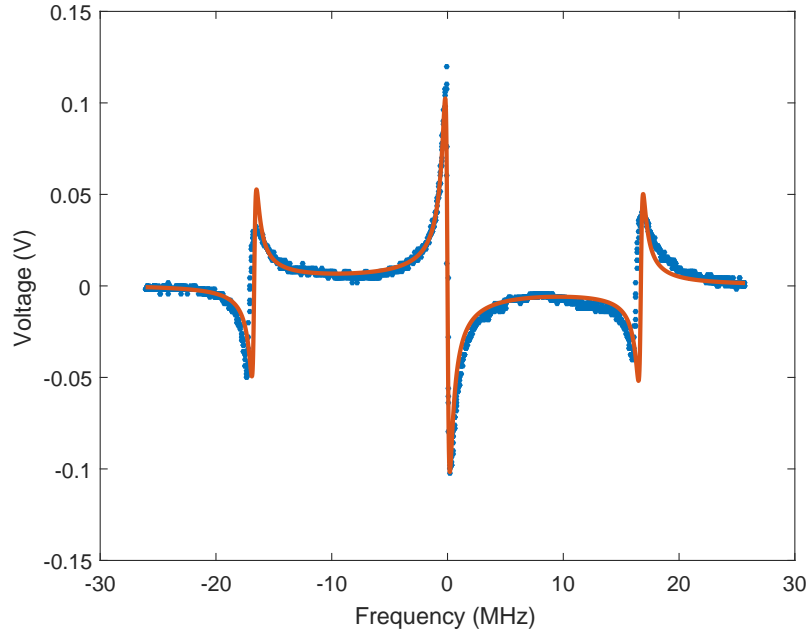


Figure A.2: Level occupation given in the equations (2.3) and (2.5) as function of the energy ε for the Bose-Einstein (blue), Fermi-Dirac (red) statistics. For comparison also the Maxwell-Boltzmann (yellow) is included.

additional low pass filter which removes the signal at twice the modulation frequency, is a signal whose value is zero on resonance since the reflection is zero and it changes sign on the two sides of the resonance. This represents our error signal. Figure A.2 shows the error signal obtained using a fast phase modulation⁴. The error signal is additionally amplified and sent to the PI system to generate the final feedback for the piezo and for the current. Locking both, one finally obtains the desired result. The error signal gives also additional informations regarding the linewidth of the cavity or of the laser. The error signal is fitted with the following relation [Mar07]:

$$S(\Delta) = A + B \cdot \frac{\Gamma \Delta \Omega (\sin(\phi) \Gamma (\Gamma^2 + \Delta^2 + \Omega^2) + \cos(\phi) \Omega (\Gamma^2 - \Delta^2 + \Omega^2))}{(\Gamma^2 + \Delta^2) (\Gamma^2 + (\Delta + \Omega)^2) (\Gamma^2 + (\Delta - \Omega)^2)}, \quad (\text{A.1})$$

where A takes into account an eventually offset, B is the amplitude of the error signal, Γ is the linewidth, Δ is the detuning of the laser with respect to the cavity resonance, Ω is the modulation frequency that drives the EOM, and ϕ takes into account not perfect phase matching between the reflected signal on the photodiode and the RF modulation sent to the

⁴Although one could think that with high modulation frequency the reflection intensity would not follow the modulation and the technique would not work. One can easily demonstrate with a quantitative model [Bla98; Nic13] that the not only high modulation frequency can be used but also that the performance of the lock are also improved.

mixer. From the fit one can obtain an approximate estimation of the linewidth. This quantity has to be referred to which one between the laser and the cavity has the largest linewidth. From the fit the linewidth(Γ) results $\Gamma = 199(4)$ kHz. The measured value is consistent with our prediction on the linewidth of both laser [Pat83] and cavity [Rie12]. Thus, one can conclude that both the long-term stabilization and the narrowing of the linewidth can be expected from the cavity and that the laser system is ready to be used in the experiment.

Acknowledgements

First, I would like to thank my supervisor Francesca Ferlaino. She gave me the possibility to do the master thesis in the exciting environment of Innsbruck where I joined a fantastic group in the ERBIUM experiment. I would like to thank her for the continuous support and the time spent in correcting my thesis.

Thanks also to my supervisor in Pisa, Donatella Ciampini. During the course of atom optics she shared with us her knowledge and she was able to transmit to me the passion for the field of ultracold quantum gases.

Many thanks to Manfred J. Mark for the patience in answering the never-ending questions. A big thanks goes to the ERBIUM team, Simon Baier, Jan Hendrik Becher, Lauriane Chomaz and in particular to Daniel Petter who were always available to clarify my doubts during the lab experience and for correcting my thesis. I would like to thank them also for giving me all the instruments to conclude my project and making the atmosphere in the group so friendly and light. Thanks to Emil Kirilov for the always fruitful discussions and for realizing such a nice laser design. I would like to thank Giulia Faraoni for the long conversation about physics and not.

Thanks to Elisa and Lorenzo for organizing the industry production of burned home-made jam and limoncello. They were always available when I need to unplug the brain.

Finally, I would like to thank Claudia for always support me and stand by my side and to be the center of my frame of reference.